UNIVERSITÀ DEGLI STUDI DI MILANO

FACOLTÀ DI SCIENZE E TECNOLOGIE

Corso di Laurea Magistrale in Fisica

# OBSERVING PERSISTENT CURRENTS IN ANNULAR FERMIONIC SUPERFLUIDS

Relatore interno:
Prof. Davide Emilio GALLI

Relatore esterno:
Dott. Giacomo ROATI

Correlatore:
Dott. Woojin KWON

Tesi di Laurea di:
FEDRIZZI MARCO
Matr. 960755

Anno Accademico 2020/2021

# Summary


**Introduction** **1**

**1 Theoretical introduction** **5**

1.1 Introduction to fermionic superfluidity . . . . . 5

1.1.1 Main paradigms . . . . . 7

BCS . . . . . 7

BEC . . . . . 8

1.2 Across the BEC-BCS crossover: the unitary gas . . . . . 8

1.2.1 Towards the unitary regime . . . . . 8

1.2.2 The unitary gas . . . . . 11

1.2.3 Condensation and superfluidity in the crossover . . . . . 13

Landau criterion for superfluidity . . . . . 16

1.3 Persistent currents in fermionic superfluids . . . . . 17

1.3.1 A remark on superconductors . . . . . 17

1.3.2 Persistent currents in quantum fluids . . . . . 19

Quantized circulation in rotating superfluids . . . . . 21

Analogy between superconducting systems and fermionic superfluids . . . . . 22

**2 Methods** **23**

2.1 Experimental apparatus . . . . . 23

2.1.1 Genesis of the gas . . . . . 24

2.1.2 Loading in the $TEM_{0,1}$ . . . . . 26

2.1.3 High resolution objective . . . . . 27

2.1.4 DMD for arbitrary optical potentials . . . . . 28

2.1.5 Imaging technique . . . . . 30

2.2 Ring geometry and characterization . . . . . 32

2.3 Phase imprinting technique . . . . . 36

2.4 Detection by interference methods . . . . . 38

2.4.1 Interference in Bose-Einstein condensates . . . . . 38

2.4.2 The problem of interference in fermionic systems . . . . . 40

**3 Measurements of persistent currents and decay in fermionic superfluids** **43**
3.1 Detection of spirals . . . 43
3.2 Phase gradient calibration: the results of phase imprinting technique . . 50
3.3 Persistence of the currents . . . 55
3.4 Critical velocity . . . 59
3.5 Disorder effects on persistent currents . . . 65

**4 Outlooks to dynamical instabilities** **73**
4.1 Double ring geometry and KH instability . . . 73
4.2 Analysis to detect KH instability . . . 77
4.2.1 Image processing for vortex detection . . . 77
4.2.2 Point vortex model . . . 80
4.2.3 Cluster analysis . . . 82

**Conclusions** **87**

**A Feshbach resonances and states in $^6$Li** **89**

**B Density depletion caused by phase imprinting** **93**

**Bibliography** **97**

# Introduction

Strongly correlated gases of ultracold fermionic atoms in arbitrary shaped optical potentials are extremely controllable and versatile quantum systems in which it is possible to study many-body fermionic matter phenomena such as superfluidity and superconductivity. In these systems, the interparticle interactions can be tuned at will by means of Feshbach resonances. This allows to explore different regimes of superfluidity from the Bose-Einstein condensate (BEC) limit of strongly bound molecules to the Bardeen-Cooper-Schrieffer (BCS) theory of long range weakly coupled Cooper pairs, and in particular to reach a regime of universality in which correlations play a fundamental role. In this regime, the interactions are the strongest possible in nature, as allowed by quantum mechanics, and the properties of the gas do not depend on the detailed characteristics of the constituents [1]. As a consequence, the thermodynamics of the gas become universal and the properties of this low density strongly interacting Fermi gas at nanokelvin directly relate, for example, to the physics of dilute neutron matter in the crust of neutron stars or to the quark-gluon plasma created at several trillion of Kelvin in the Early Universe. Moreover, by looking at critical temperatures, Fermi gases in the BEC-BCS crossover share several characteristics with high temperature superconductors: since the latter exhibit mechanisms which are not fully understood yet, ultracold fermionic gases can act as powerful quantum simulators to better investigate the essence of superconductivity, achieving the celebrated quantum computing originally proposed by Feynman [2] to overcome limitations of classical simulations.

In particular, a paradigmatic phenomenon of superfluid/superconducting state consists in the possibility to sustain current flows remaining constant in time without being driven by any external force. This is a well known phenomenon in solid-state superconductors [3, 4], originating from the application of a Aharonov-Bohm phase [5], and this persistent charge oscillates with the magnetic flux [6] causing a quantization of the magnetic flux trapped in the superconductor [7]. These persistent currents can also be observed in normal mesoscopic systems [6, 8, 9], when the system size is sufficiently small that the orbital motion remains quantum phase coherent throughout. The possibility to detect these currents leads to a variety of applications, e.g. building quantum devices (such as the very famous SQUIDs) which act as magnetometers or gradiometers [10] that find their utility in a variety of scientific fields including medicine and metrology.

By employing ultracold quantum gases, the engineering of tailored optical potentials [11, 12] allows the realization of a variety of tunable geometries. In particular, persistent currents in ring-shaped traps can be excited by the application of arbitrary optical potentials with a digital-micromirror-device (DMD) [13]. Stability and decay of these supercurrents have thus been studied both in Helium superfluids and in thin-wire superconductors [14], but still the decay mechanisms are not fully understood yet [15]. More recently, a quantity of experiments have been performed studying widely the persistent current phenomenon in Bose-Einstein condensates [16–22] by investigating kinds of dissipation due to barriers, temperature or vortex shedding, and pointing out their extremely powerful applications also in atomtronics [23].

Persistent currents in fermionic systems are instead a very new field of investigation [24]. The interest lays on multiple reasons, from the more exotic possibility to employ persistent currents in fermionic superfluids as ideal laboratory systems to simulate pulsar glitches [25], to the prospect of investigating fundamental phenomena of fermionic superfluidity, for example using supercurrents as a powerful tool to probe the BEC-BCS crossover [26]. Moreover, it is possible to investigate the decay mechanisms arising when impurities of disordered potentials are inserted in the landscape of the atomic motion. Another possibility is to use high resolution tailored optical potentials to explore annular geometries in which the width of the ring is comparable with or lower than the pair size of the fermions, and investigate the non-trivial fundamental physical phenomena that arise.

In this thesis work, we report the first observation of persistent currents through the BEC-BCS crossover, investigating also some possible decay mechanisms. We present the phase imprinting technique together with interference detection as very powerful methods that allow the manipulation both of the phase and of the density of the macroscopic wave function describing the gas. A full control of the order parameter of the system is thus achieved, and this renews the interest to employ ultracold atomic Fermi gases as quantum simulators for more complex systems. The employed techniques allowed the characterization of the excitation, persistence, and decay of the currents, by studying also the effects of Landau-like impurities in the flow and the consequence of the application of random optical impurities. As a conclusion, we show that the results open the field to study the effects of quantum dynamical instabilities in a single component fermionic superfluid.

The outline of this work will pursue the following structure. In chapter 1 we will set the framework to introduce the systems employed in the experiments: we will present the BEC-BCS crossover and the peculiarities of the gas at unitarity, and we will also discuss some dissipation mechanisms (such as the Landau criterion) of the superfluid phase. Finally, persistent currents in fermionic superfluids will be presented by underlying the strong analogies and differences with the world of solid state superconductors. A review of the state-of-art persistent flows in ultracold atoms is provided and the chapter is concluded with a theoretic description of the rotation of a superfluid, up to obtain the quantization condition for the superfluid velocity.

Chapter 2 will instead provide the methods, main instruments, and techniques, employed during the work to generate and manipulate the gas, and to analyze the experimental data. The chapter will begin with a description of the experimental apparatus: the atoms will be followed from their evaporation in the oven, up to the science chamber in which they are confined and cooled down to reach degeneracy. We will describe the tool employed to obtain oblate uniform geometries and the possibility to imprint high resolution arbitrary optical potentials with a digital micromirror device (DMD). The description of the imaging setup will conclude the explanation of the experimental apparatus. The chapter will continue with the presentation and the characterization of the geometry we employed in the work, to arrive at the discussion on the phase imprinting technique, which is the method used to excite currents: we present both theoretic concepts and experimental realization of the technique. As a conclusion of the chapter, we will provide a discussion on interference methods we use to obtain information on the systems, and an explanation of the main issues coming out when dealing with fermionic systems.

In chapter 3, the main results of this thesis work will be presented and discussed. We will begin it providing expected and obtained interference pattern from the time-of-flight expansion of the superfluids in our system. We will see that the result is a pattern made of spirals, whose number we are able to link to the winding number of the superfluid. Since the number of spirals is so important, we also provided some quantitative methods to count them. This allowed us to study the effects of the phase imprinting on the annular superfluid: we have thus related the time duration of the imprinting to the applied phase gradient, and consequently to the excited circulations, reporting the results for a quantized flow. It will be possible, at that point, to study the persistence of the current in time across the BEC-BCS crossover for different imprinted circulations, from zero to eight. A further step that we will be presented is studying the decay mechanisms: firstly we will probe Landau criterion by adding a few number of obstacles in the annular trap. Then, some random optical obstacles will be inserted to study the effects of a disordered potential on the atoms.

Finally, in chapter 4, we will discuss some possible outlooks of our work. In particular, the attention will be focused on the study of dynamical instabilities in a double ring geometry. Experiments to explore Kelvin-Helmholtz instability in a single component superfluid will be proposed, and also the required analysis will be presented together with some preliminary results.

# Chapter 1

# Theoretical introduction

Superfluidity and superconductivity are fascinating phenomena, which regard respectively mass and charge transport without dissipation in particular materials. These phenomena usually take place when very low temperature are achieved. A lot of efforts have been done during the years to explain with a suitable theory the related phenomenology; in particular the research reached its peak in the 1956 with the appearance of the BCS (Bardeen-Cooper-Schrieffer) theory [27] for superconductors, and in the 1970s with the study of the $^4$He superfluidity [28]. In this context, some discoveries led by the superfluidity in $^3$He, brought an always greater interest in studying fermionic superfluidity.

In this chapter, it will be briefly presented the phenomenon of the superfluidity in fermionic systems and its peculiarities in section 1.1, then the crossover between the two main paradigms of superfluidity will be discussed in section 1.2. Finally, in section 1.3, some attention will be paid in illustrating the phenomenon of the persistent currents in circulating fermionic superfluids.

## 1.1 Introduction to fermionic superfluidity

After the experimental realization of a quantity of Bose-Einstein condensates [29], great efforts have been done to achieve quantum degeneracy in atomic Fermi gases. The reason of interests for fermionic systems is that most of the fundamental particles present in nature are fermions (quarks, leptons, baryons); moreover understanding the physics of quantum effects in Fermi gases is important for many systems, from transport properties of electrons in metals and semiconductors, to superconductors, superfluid $^3$He, quark matter and neutron stars.

In Bose-Einstein condensates, the condensation of the bosons is detectable since a phase transition occurs and the density distribution becomes bimodal. Instead, dealing with Fermi systems, things get more complicated. In fact, by following the same approach as Bosons, one would proceed as follows: considering an ideal Fermi gas, the

| System | $T_C$ | $T_F$ | $T_C/T_F$ |
|---|---|---|---|
| Metallic lithium at ambient pressure | 0.4 mK | 55 000 K | $10^{-8}$ |
| Metallic superconductors (typical) | 10 nK | 100 000 K | $10^{-4}$ |
| $^3$He | 2.6 mK | 5 K | $5 \times 10^{-4}$ |
| $MgB_2$ | 39 K | 6 000 K | $10^{-2}$ |
| High-$T_C$ superconductors | 100 K | 5 000 K | $2 \times 10^{-2}$ |
| Neutron stars | $10^{10}$ K | $10^{11}$ K | $10^{-1}$ |
| Strongly interacting atomic Fermi gases | 170 nK | 1 $\mu$K | 0.17 |

Table 1.1: Transition temperatures, Fermi temperatures, and their ratio $T_C/T_F$ for a variety of fermionic superfluids and superconductors.

Fermi energy is

$$E_F = \frac{\hbar^2}{2m}\left(3\pi^2 n\right)^{2/3} \tag{1.1}$$

where $n$ is the density of the gas. It is straightforward defined a temperature scale in which the density distribution deviates from the Maxwell-Boltzmann, namely $T_F = E_F/k_B$; in particular it happens when the phase-space density is

$$n\lambda_{dB} \simeq 1.504\ . \tag{1.2}$$

The problem is that, in difference with what happens in the bosonic case, fermions do not condense at the Fermi temperature, since the Pauli principle prevents them to macroscopically occupy the single-particle ground state. Thus, a different mechanism for the condensation of pairs have been researched. This opened the field to the BCS theory which explained the fermionic condensation mechanisms.

In the recent years, the interest in ultracold Fermi gases has moved to study systems in which interactions are manipulated and changed by means of Feshbach resonances (see Appendix A). In particular the a great interest has been captured by the investigation of strongly interacting fermionic gases, to access properties of the fermionic superfluidity i.e. the BEC-BCS crossover, which will be discussed in section 1.2.

In particular, the phenomenon of the superfluidity in Fermi gases does not emerge together with the condensation as in the bosonic case; instead it appears from the pairing of fermions. This happens usually at temperatures well below the Fermi temperature $T_F$; it is indeed possible to distinguish between two main ranges: we reported in table 1.1 the values for typical superfluid and superconducting systems: strongly interacting Fermi gases are indeed in a superfluid state already at $T_C/T_F = 0.017$. Surprisingly enough, these systems result to be more similar to extremely high density and temperature neutron stars than metallic superconductors: scaled to the density of electrons in metal, this kind of superfluidity would occur far above room temperature.

As said, superfluidity is the phenomenon emerging in a gas that flows without any dissipation and, in Fermi system, it is indeed directly related to superconductivity. The most common proofs of a superfluid behavior are the existence of a critical velocity and the quantization of vortices, which we are going to discuss in section 1.2.3. Before discussing of the strongly interacting regime, we will briefly report the main result on the two paradigms for superfluidity; then we will arrive to describe the smooth crossover linking the two limits.

### 1.1.1 Main paradigms

Historically speaking, BEC and BCS are the two main paradigms used to explain the phenomenon of superfluidity, as it will be discussed in section 1.2.1. Here, the basic knowledge of these two theory are taken for granted, just some of the main results achieved will be recalled.

Both fermionic BEC and BCS are described by an order parameter which can be written as

$$\psi = \sqrt{N_0}\, e^{i\varphi} \tag{1.3}$$

where $N_0$ indicates the number of condensed pairs. The condensation implies the presence of a macroscopic quantum phase coherence, so the phase $\varphi$ can be assigned to all the atoms of the condensate.

#### BCS

For the BCS theory applied to fermion superfluidity, it is possible to employ mean field theory to extract some useful quantities. One finds out that the chemical potential equals the Fermi energy:

$$\mu \approx E_F \ . \tag{1.4}$$

Moreover, the gap near the Fermi surface is

$$\Delta \approx \frac{8}{e^2} e^{-\pi/2k_F a} \tag{1.5}$$

which is indeed exponentially small compared to the Fermi energy, meaning that the Cooper pairing is very fragile.
It is also possible to write the ground state energy:

$$E_{G,BCS} = \frac{3}{5} N E_F - \frac{1}{2}\rho(E_F)\Delta^2 \ . \tag{1.6}$$

There are two main contributes to the ground state energy: the first term is due to the fact that the interaction is mediated by the Fermi sea, since $\frac{3}{5}E_F$ is the average kinetic energy per fermion in the Fermi sea. The second term, instead, is the energy of the condensation; it is negative, pointing out that the condensed state is energetically favorable compared to the normal one.

Since the gap $\Delta$ is exponentially suppressed with the interaction parameter $1/k_F a$, in order to experimentally achieve superfluidity in Fermi gases it is required to use Feshbach resonances to increase the scattering length. By doing so, it is possible to access the regime $k_F|a| > 1$ where $\Delta > 0.22 E_F$.

**BEC**

It is possible to follow the same approach for BEC fermionic superfluids. The result for the chemical potential is:

$$\mu = -\frac{\hbar^2}{2ma} + \frac{\pi\hbar^2 an}{m} \tag{1.7}$$

which is made of two terms. The first one is the binding energy per fermion in a tightly bind molecule; instead, the second term is due to the repulsive interactions between molecules in the gas, by considering a molecule with mass twice that of the fermions $m$, and a density which is half the gas density $n$. Clearly, in equation 1.7, $a$ stands for the scattering length.
It is also possible to derive the quasiparticle energies

$$E_k \approx |\mu| + \varepsilon_k + \frac{4\pi\hbar^2}{m}na \tag{1.8}$$

where the last term is the mean field energy which a fermion experiences in a gas of molecules.

It is worth to point out that these expressions do not take into account three and four body interaction. Those interactions are indeed exponentially suppressed because of the high binding energy with which molecules are bound together.

## 1.2 Across the BEC-BCS crossover: the unitary gas

### 1.2.1 Towards the unitary regime

Since early ages of superfluidity theory, it was clear that the two main paradigms were not overlapping [1]: on the one side Bose-Einstein condensation (BEC) explains the main mechanism for weakly interacting bosonic gases superfluidity, on the other side Bardeen-Cooper-Schrieffer (BCS) theory describing long range fermion pairs. However, Schrieffer pointed out that BCS superfluidity is not Bose-Einstein condensation of fermionic pairs, since these pairs do not obey Bose-Einstein statistics [27].

In a Fermi gas, there is just a temperature scale which is set by the Fermi energy: $T_F = E_F/k_B$. Lowering the temperature causes no phase transition, but a gradually formation of the Fermi sea; it plays a central role in Cooper pairing, which is indeed a many body effect mediated by the Fermi sea. Usually in superconductors the critical temperature is described by $T_C \simeq \hbar\omega_D e^{-1/\rho_F|V|}$, where $\omega_D$ is the Debye frequency, $\rho_F$ is the density of states at the Fermi surface, and $|V|$ is the strength of electron-phonon coupling. Instead in Fermi gases $T_C$ is proportional to $E_F$ since the attractive contact interactions are working through the entire Fermi sea; still the exponential suppression is present, so

$$T_C \simeq E_F e^{-\pi/2k_F|a|} \tag{1.9}$$

In this expression we have introduced the Fermi wavevector $k_F = \sqrt{2mE_F}/\hbar$ and the scattering length $a$. It is clear now that $k_F a$ represents the ratio between inter-particle

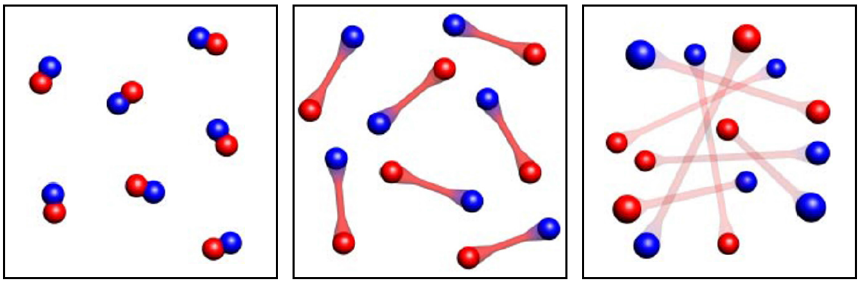


Figure 1.1: The size of the pairs in the BEC-BCS crossover. In the BEC side, pairs are tightly bound and the inter-particle distance $1/k_F$ is much larger than the scattering length $a$, while in the BCS limit $a$ is large compared to $1/k_F$, so the pairs are very slightly bound and distant. In between there is no singularity but a system in which the pair size is comparable with the inter-particle spacing. Image taken from [33].

distance and the scattering length, and so it defines a characteristic parameter of the gas: for energy below the Fermi energy $E_F$, the pair size is much larger than the inter-particle spacing, so thousands of fermions are in between any pair.

On the other hand, a weakly interacting Bose gas degenerates when the inter-particle distance becomes comparable with the thermal de Broglie wavelength of particles:

$$\lambda_T = \left( \frac{2\pi\hbar^2}{mk_B T} \right)^{\frac{1}{2}} \tag{1.10}$$

This corresponds to a degeneracy temperature $T_D \simeq \hbar^2 n^{2/3}/2m$, below which bosons start to condensate in the ground state. Despite the very first idea due to Fritz London in the '50s to unify the two regimes has revealed not correct, still it is clear that the BEC is somehow connected with the fermionic superfluidity, namely it is in the regime of tight bound Fermi pairs. This happens whenever the inter-particle distance is much greater than the pair size, namely when $1/k_F a \gg 1$: in this scenario the fermionic nature of any two particles of a couple cannot play a role since the fermionic wave function is spread out over many Fermi wavevector in momentum space, and therefore Pauli repulsive force is not relevant.

Therefore a question arises: how are these two regimes connected? What is in between the limit of Bose-Einstein condensate of strongly bound fermionic pairs - which appears when repulsive interactions between fermions at $1/k_F a \gg 1$ take place - and the formation of Cooper pairs for weak attractive interactions when $1/k_F a \ll -1$? During the 1960s some firsts attempts were made in order to find an answer: a first observation was that the wave function of the BCS, was not only suitable for long-range condensation of Cooper pairs, but also for tightly bound pairs of a Bose-Einstein condensate [30–32].

In particular, Eagles discovered the formation of the pairs at a temperature above the critical temperature $T_C$: he held constant the scattering length (positive or negative

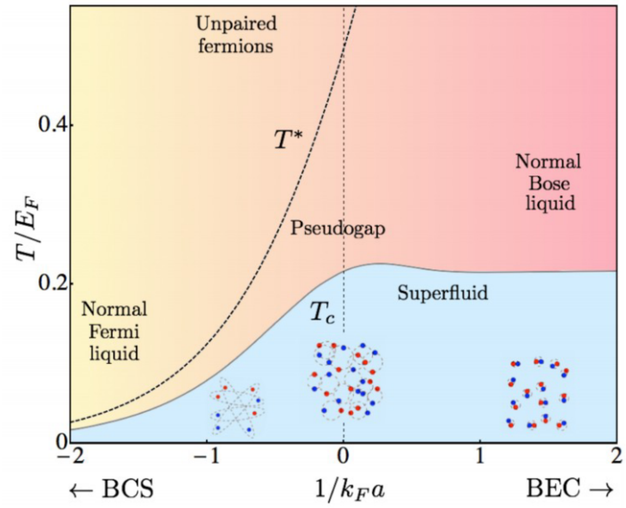


Figure 1.2: Phase diagram of the BEC-BCS crossover. Pairs form under the temperature $T^*$, while the system condensates below the temperature $T_C$; it decays exponentially in the BCS side, and recovers the value for Bose-Einstein condensate of tight bound pairs in the BEC limit varying smoothly across the region in which $a \to \infty$. Image from [35]

accordingly) and varied the inter-particle spacing. It brought to the 1980, when Leggett [34] showed (by using a generic two body potential) that BEC and BCS limits are connected in a smoothly crossover: he kept instead fixed the inter-particle distance, and varied the scattering length; in that case the pairs change from having a strong binding energy and a small size in the BEC side, to be far and with small binding energy in the BCS side (ref fig 1.1). Between these two regimes there is no singularity, instead a system in which the inter-particle spacing become comparable with the pair size. It happens when $a \to \infty$, so $1/k_F a = 0$ and therefore the system enters in a universal regime of scale-invariance in which the only energy scales that matter are the Fermi energy and the temperature.

Before entering deeper in the characteristics of this regime, it is worth to mention the work by Nozières and Schmitt-Rink [36] which extended the Leggett model for finite temperature: they showed that the critical temperature for superfluidity $T_C$ decays exponentially in the BCS limit, in which it is very small and equal to the pair breaking temperature $T^*$. Moreover $T_C$, as shown in fig 1.2, varies smoothly across the crossover to reach, in the $1/k_F a \gg 1$ limit, the value for Bose-Einstein condensate of tightly bound molecules.

We are now going to describe more in details the features of the regime in which the scattering length diverges, which takes the name of ”unitary regime”.

### 1.2.2 The unitary gas

As we have just explained, between the two well known regimes of BEC and BCS, there is a smoothly crossover through a regime very peculiar in which the scattering length $a$ diverges. The gas in this condition is called unitary Fermi gas (UFG), and has peculiar characteristics.

Since $a \to \infty$, it means that the interactions are the strongest possible, as allowed by quantum mechanics. As a consequence, it follows that $1/k_F a = 0$, meaning that the inter-particle spacing is of the same magnitude order of the pairs size. This implies that the bond length of the pairs plays no role in the description of the gas: the only two magnitude scales are fixed by the spacing between particles in the gas $n^{-1/3}$ - associated indeed with an energy scale which is the Fermi energy -, and the de Broglie wave length $\lambda_T$, which is straightforward to relate to the temperature.

These characteristics allow the gas to enter in a universality class so that it can be described as a scale invariant system where the only parameter that matters is the dimensionless parameter $q = \beta\mu = \mu/k_B T$; so, also the thermodynamics becomes universal: it means for example that the thermodynamic properties of the gas are directly correlated with those of an non-interacting Fermi gas by a function of $T/T_F$; therefore at zero temperature, the equation of state and the properties of these two gases have to be the same. It is also possible to calculate the mean free path $\lambda$ of the particles inside the gas when the scattering length diverges: $\lambda = (n\sigma)^{-1}$, and therefore $\lambda \sim 1/k_F$. It means that the mean free path is the shortest possible, namely as short as the inter-particle distance, which means that the strongly interacting fermionic gas of atoms at nanokelvin is a "perfect liquid". Surprisingly enough, there's another physical system which satisfies the same condition, which is the quark-gluon plasma at extremely high temperatures (trillions of Kelvin).

As we said, as a result of the scale-invariance, the properties of the UFG can be derived by those of the non-interacting Fermi gas; it happens by means of a parameter $\xi$, called Bertsch parameter. It has been measured for zero temperature spin balanced gas for which the value is $\xi = 0.37$ [37]. It is possible therefore to write [33] the chemical potential $\mu$ of the UFG related to the Fermi energy $\mu = \xi E_F$ which, for harmonic trapping, becomes $\mu = \sqrt{\xi} E_F$. It is also possible to derive the equation of state (EoS) of the unitary Fermi gas. We are interested mainly in the density EoS, since it is accessible by directly imaging the atomic sample; it is possible to write it as:

$$n = \frac{1}{\lambda_T^3} \cdot f_n(q) \tag{1.11}$$

where $\lambda_T$ is the already defined de Broglie wavelength, and $f_n(q)$ is a generic function which depends on the invariance parameter $q = \mu/k_B T$. The functional form of $f_n(q)$ depends on the range of $q$ values, and it can be derived with different methods:

- $\mathbf{q < -1.5}$ for low $q$ it is possible to perform a virial expansion in the gran canonical ensemble.

- $\mathbf{q} > \mathbf{3.9}$ for high values of $q$ the main contribution to the excitation spectrum is due to the phonons, so a phonon model can be employed.
- $\mathbf{-1.5} \leq \mathbf{q} \leq \mathbf{3.9}$ for values of $q$ in between, it is experimentally accessible.

The result is a parametric equation of state that can be written as follows [38]:

$$f_n(q) = \begin{cases} \sum_{s=1}^{4} s\, b_s\, e^{sq} & \text{if } q < -1.5 \\ -Li_{3/2}(e^{-q})F(q) & \text{if } -1.5 \leq q \leq 3.9 \\ \frac{4}{3\pi}\left[\left(\frac{q}{\xi}\right)^{3/2} - \frac{\pi^4}{480}\left(\frac{3}{q}\right)^{5/2}\right] & \text{if } q > 3.9 \end{cases} \tag{1.12}$$

where $b_s$ are the virial expansion coefficient, known up to the 4th order, $Li_n(z)$ is the polylogarithm function of order $n$, and $F(q)$ is experimentally interpolated.

Concluding the treatment of the unitary regime, a discussion is provided to remark the difference in physics phenomena taking place across the crossover: the different nature of the fermionic superfluids play a significant role in determine the relative properties, such as excitation (as we will see in section 1.2.3), pair size, and so on.
The spatial wave function of the crossover regimes can be derived, and it clearly exhibits different features. In the BCS limit, Cooper pairs form close to the Fermi surface, thus with a momentum $k = k_F$, so the spatial wave function has a strong modulation at hte inverse wave vector $1/k_F$. It is possible to write therefore:

$$\psi(r) = \frac{k_F}{\pi r^2} \frac{\Delta}{\hbar v_F} \sin(k_F r) K_0 \left(\frac{r}{\pi \xi_{BCS}}\right) \tag{1.13}$$

where $v_F$ is clearly the Fermi velocity, $r = |\mathbf{r}_1 - \mathbf{r}_2|$, while $K_0(kr)$ is the modified Bessel function and decays exponentially when argument goes to infinity. Instead, $\xi_{BCS}$ is the characteristic size of the Cooper pair that corresponds, in BCS, to the two particle correlation length. It can be computed as

$$\xi_0 \approx \xi_{BCS} \equiv \frac{\hbar v_F}{\pi \Delta} \tag{1.14}$$

In the BEC limit, on the other side, the wave function decays exponentially as

$$\psi(\mathbf{r}_1, \mathbf{r}_2) = \frac{e^{-|\mathbf{r}_1 - \mathbf{r}_2|/a}}{|\mathbf{r}_1 - \mathbf{r}_2|} \tag{1.15}$$

which is trivially the wave function for a molecule of size $a$. As a consequence, the two-particle correlation length reads: $\xi_0 = a$. From equation 1.15 follows that the BEC spatial wavefunction broadens as the pairs become more and more tightly bound.
The unitary features can thus finally be extracted by smoothly interpolating the two regimes [34] and the results can be seen in fig. 1.3.

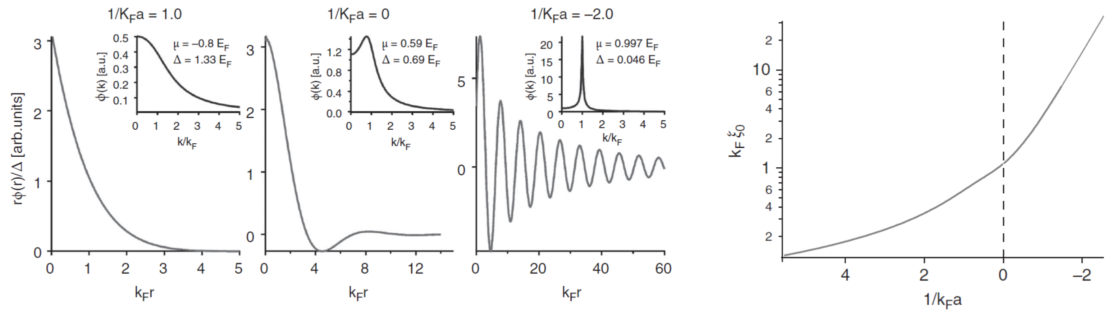


(a) Evolution of the spatial pair wave function $\psi(r)$ for different values of $1/k_F a$. In the insets, the Fourier transform of $\psi(r)$ is shown: in the crossover, pairing affects the entire momentum distribution from a localized one near the Fermi surface, to broader ones with more tightly bound pairs. Adapted from [1]

(b) Evolution of the pair size from tight bound molecules to long range Cooper pairs. At the resonance (in dashed line) the pair size is comparable to the interparticle spacing. Image from [1]

Figure 1.3: Evolution of the spatial pair wave function (a) and of pair size (b) in the BEC-BCS crossover, from the Legget ansatz.

### 1.2.3 Condensation and superfluidity in the crossover

As a conclusion of the discussion about the crossover in fermionic superfluids, it is presented here a remark on the difference between condensation and superfluidity in these systems (we will restrict the discussion to the three dimensional regime, since when lower dimensions are achieve different phenomena takes place such as the Berezinskii-Kosterlitz-Thouless transition [39, 40]): we will see that in the three different regimes, the relative condensed versus superfluid fraction are different and a 100% superfluid behavior can take place also when condensed fraction is very low.

As well-known, condensed fraction is related in BEC to the presence of off-diagonal long range order (ODLRO) in the one-particle density matrix. When dealing with fermionic gases, the one-particle density matrix can never have a macroscopic matrix element, since Pauli principle prevents the occupation number of a particular quantum state from exceeding unity. Indeed, for fermionic superfluids the long range order appears in the two-particle density matrix. We report the formula obtained for condensed fraction in BCS regime to be compared with the one of the superfluid fraction we will write later in the text. In BCS regime it reads [1]:

$$n_0 = \frac{mk_F}{8\pi\hbar^2}\Delta = \frac{3\pi}{16} n \frac{\Delta}{E_F} \tag{1.16}$$

so the condensed fraction exponentially decreases like the gap, with the interaction strength. This strong depletion is - as said - due to the Pauli principle.
Anyway this depletion does not prevent the system to exhibit superfluid behavior, since it is linked to the macroscopic coherence of the wave function phase.

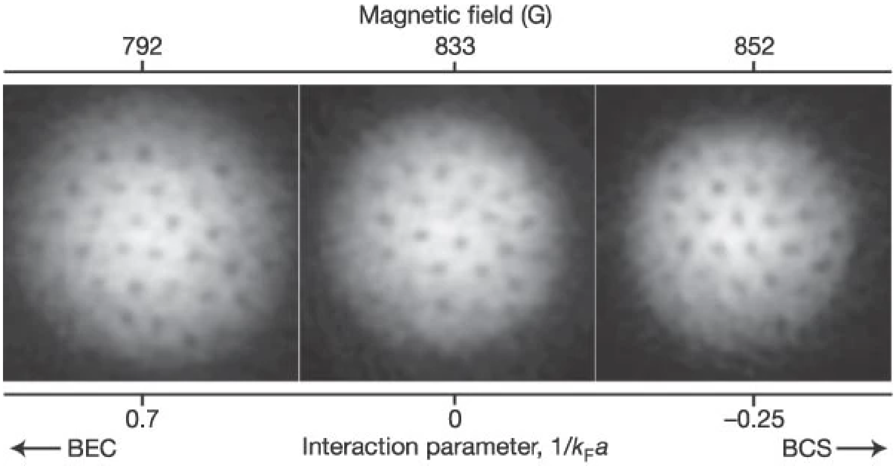


Figure 1.4: Observation of vortex lattice in strongly interacting Fermi gas. Different kinds of fermionic superfluids are put in rotation by two laser beams; after a time-of-flight expansion an ordered lattice of vortices is created. Image from [41]

Superfluid fraction in a fermionic ultracold gas, is indeed the fraction of the fluid which exhibits superfluid behavior. In general, it is not directly related to the condensed fraction, e.g. two-dimensional Bose gas can be superfluid although the Mermin-Wagner theorem prevents it to exhibit off-diagonal long range order, or on the other side a non-interacting BEC can be condensed but not superfluid. The basis of the models for superfluids and superconductors lies in the distinction between normal density $n_n$ and superfluid density $n_s$ which bring to a two-fluid hydrodynamic description. Here, $n_s$ can be found from the total density trivially as $n_s = n - n_n$. In the BCS regime, for $T \ll T_C$, it holds:

$$n_s = n \left( 1 - \sqrt{\frac{2\pi\Delta_0}{k_B T}} e^{-\Delta_0/k_B T} \right) \tag{1.17}$$

from which it is visible that at low temperatures the contribution of the quasiparticles is suppressed, as it is characteristic for gapped excitation spectra.
By comparing equations 1.16 and 1.17, it is clear the difference in the dependence from physical quantities. We presented the BCS regime because it is the clearest example: at zero temperature the condensed fraction is very low (tends to zero with the interaction strengths) while the superfluid one is 100%.

A directly evidence of superfluidity across the main regimes of fermionic superfluids was obtained at MIT [41] and shown in figure 1.4: three pictures are shown of the three different superfluid regimes of $^6$Li atoms in the BEC-BCS crossover. The gas is stirred with two laser beams e put into rotation, and after a time-of-flight expansion, a vortex lattice forms. The uniformity of the lattice spacings is a sign of the quantization of the vortex charge [29], and thus a striking evidence of superfluid behavior.

More recently, it was measured the superfluid fraction of a unitary Fermi gas (see section 1.2.2) by looking at the second sound [42]. It is indeed possible to describe

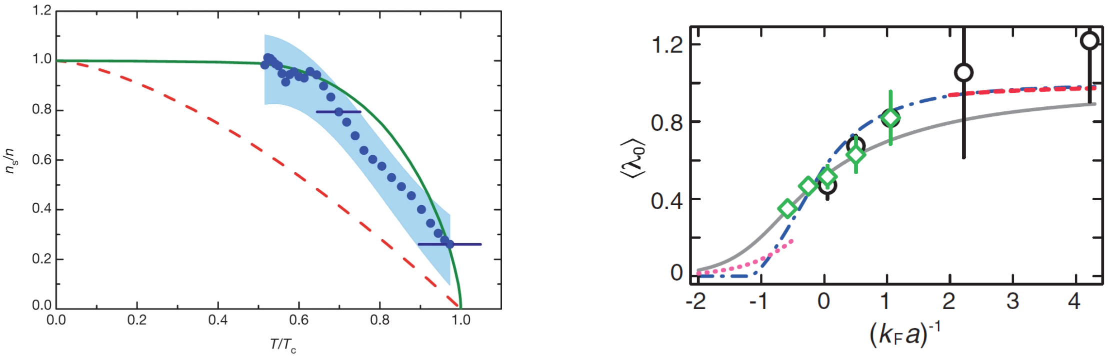


(a) Superfluid fraction in unitary gas. Blue dots show the measured superfluid fraction for different temperatures with their uncertainties (shaded region); green solid line is fraction for Helium II, while red dashed line represents the condensed fraction expected for an ideal Bose gas. Image from [42]

(b) Condensed fraction for fermionic superfluids. The condensed fraction of different fermionic superfluid regimes has been measured (diamonds and circle points) in function of the interaction parameter $1/k_F a$ from Josephson effect; the lines represent some different theoretical predictions. Image from [43]

Figure 1.5: Comparison between superfluid and condensed fraction in fermionic superfluids. The second sound measurement (a) allows to access at the superfluid fraction since the two phases - thermal (normal) and superfluid - oscillate with opposite phases. On the other side a Josephson experiment (b) accesses directly to the condensed fraction, since the Josephson current is proportional to it.

superfluid gases as two-mixture systems: the first mixture is made of a normal component, while the second is a superfluid gas with zero viscosity and zero entropy. The second sound is an entropy wave where the two components (normal and superfluids) oscillate with opposite phases.

In fig 1.5a the results of the study are represented: the measured superfluid fraction is plotted against temperature in units of the critical temperature $T_C$, and it is compared to the expected condensed fraction of an ideal Bose gas (red dashed line). It is clear that the system is entirely superfluid at temperatures of $0.6T/T_F$ when the condensed fraction is instead almost an half. This condition is thus expected to be satisfied for all the fermionic superfluids that we are talking about in these thesis. On the other side, very recent experiments have measured the condensed fraction of different fermionic superfluids. It showed up [43] that in the unitary gas, regardless the kind of trap used, the condensed fraction is much lower; in particular at $T = 0$ it was found a mean condensed fraction of $0.47 \pm 0.07$.

In particular, also at T=0, when for BEC condensed fraction is 100% just as superfluid one, in UFG and BCS regime the two percentage do not correspond. It follows that this is another criterion distinguishing the different regimes in the BEC-BCS crossover:

a zero temperature unitary gas is just half percent condensed but still exhibit superfluid behavior as strikingly proven by the vortex lattice shown in fig. 1.4.

We have presented two different experiments probing superfluid and condensate fractions, by measuring the second sound mode and by looking at the Josephson current respectively. The experiment we will present in this thesis will provide instead a more unique quantity across the BEC-BCS crossover, which is the persistence of currents. From the results we will report, we confirm that the phenomenon is independent from the condensed fraction and instead fully lies on the superfluid behavior of the fermionic systems.

**Landau criterion for superfluidity**

We will further investigate quantization of vortices in the section related to circulating superfluid. Now we want to remark another feature which will be useful in the proceedings.

It has been mentioned before, that one of the evidences for superfluidity is the presence of a critical velocity. As a matter of fact, it happens that a superfluid flows without dissipation only if its velocity is lower than a critical velocity $v_c$. The first theoretic explanation is due to Landau [44], who linked the dissipation with the creation of excitations: if the superfluid is moving faster then $v_c$, it is energetically favorable to it to transfer momentum from the moving superfluid to excitations. As a result of the loss of momentum, superfluid flow is damped. Let's consider an excitation carrying plane-wave momentum $\hbar\mathbf{k}$: to be created it must satisfy energy and momentum conservation laws. It means

$$M\mathbf{v}_i = M\mathbf{v}_f + \hbar\mathbf{k} \tag{1.18}$$

$$\frac{1}{2}M\mathbf{v}_i = \frac{1}{2}M\mathbf{v}_f + \varepsilon_k \tag{1.19}$$

where $M$ is the mass of the whole fluid. By simplification of the equations and assuming mass of the fluid big enough to ignore motion of center of mass (it is also possible to release this assumption by considering the rest frame) it is straightforward to obtain:

$$\varepsilon_k = \hbar\mathbf{v}_i \cdot \mathbf{k} = \hbar v_i k \cos\vartheta \leq \hbar v_i k \ . \tag{1.20}$$

It means that for an excitation to be created the condition $v_i \geq \varepsilon_k/\hbar k$ must be satisfied. It follows the Landau criterion for superfluidity which states that in order the fluid to flow without dissipation, it must move with a velocity lower than a critical velocity $v_c$ defined by:

$$v_c = \min_k \left[\frac{\varepsilon_k}{\hbar k}\right] \tag{1.21}$$

where the minimum value is taken over all the possible excitation, including both collective and single-particle excitations.

It is thus clear that the critical velocity depends on the excitation spectrum, and therefore on the kind of superfluid we're dealing with: e.g. in the BEC regime relevant excitations correspond to Bogoliubov sound waves [33] with speed of sound

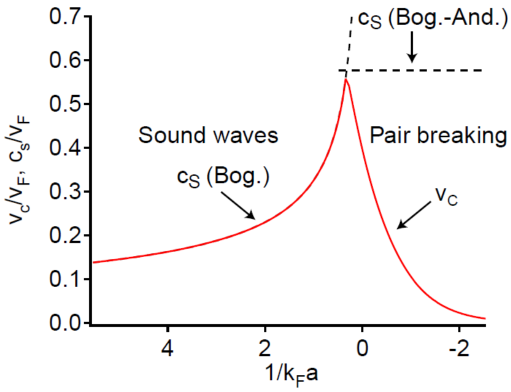


Figure 1.6: Critical velocity in the BEC-BCS crossover. In the BEC side, lowest excitations are Bogoliubov waves (Bog.) which are usually referred as Bogoliubov-Anderson waves (Bog.-And.) in the BCS regime; here actually the lowest energy excitations are single-particle due to the breaking of Cooper pairs. Image taken from [33].

$c_s = \sqrt{\mu/m} = \frac{v_F}{\sqrt{3\pi}}\sqrt{k_F a}$. On the other side, in the BCS regime critical velocity can be lower, since the first excitations are single particle ones involving the breaking of Cooper pairs. Instead, at the resonance, an interplay of the two natures causes the critical velocity to be the highest, therefore to obtain the most robust system.

In fig. 1.6 it is shown the critical velocity across the BEC-BCS crossover: the evolution from Bogoliubov (Bog.) waves in the BEC to the pair breaking in the BCS is smooth. Here (at the resonance), the critical velocity assumes its maximum value, and therefore at unitarity the superfluid is the most stable.

## 1.3 Persistent currents in fermionic superfluids

It is possible in superfluids and superconductors, that currents flow without a driven external force remaining constant in time. These flows are thus called ”persistent currents”, since they can resist for timescales much longer than the experimental sample itself. They were first observed [3, 4] and predicted in the field of superconducting materials, in which a lot of remarkable properties take place, but then they were discovered also in superfluid phases [45–47]. Since there are many analogies between what happens in superconducting systems and in fermionic superfluids, it is useful to take an insight of some remarkable properties discovered in the field of superconductivity.

### 1.3.1 A remark on superconductors

The phenomenon of persistent flow is one of the most remarkable properties of macroscopic quantum systems. It takes its genesis in the world of superconductors. In 1911 Kamarlingh Onnes first discovered this phenomenon by studying the resistivity of a mercury sample at low temperatures: he observed that the resistance dramatically drops below $4.2K$. Clearly, since the resistance becomes very low below the critical temperature, the flow of the electric current is damped very slowly, and the decay rate is so big to become often experimentally inaccessible. For example by taking into account a superconducting ring below $T_C$, the insertion of a magnet causes a variation of the magnetic flux which induces a current; this current decays as

$$I(t) = I_0 e^{-Rt/L} \tag{1.22}$$

where $L$ is the inductance and $R$ the resistance. By taking into account this method it was estimated that the passage trough the critical temperature causes the resistance to reduce its value by 16 magnitude orders at least.

Persistence currents are actually a phenomenon observed also in normal mesoscopic systems [48, 8, 9] where the system size is sufficiently small that the orbital motion remains quantum phase coherent throughout. This persistent charge oscillates with the flux and it is generated by the Aharonov-Bohm (AO) phase factor [6]. The AO effect [5] consists in the fact that the electromagnetic vector potential influences the quantum-mechanical orbital motions of electrons, even if the particles move in a region with vanishing electric and magnetic fields. This is a purely quantum-mechanical effect which manifests itself trough the acquisition of the AO phase factor that can change the boundary condition on the orbital wave function.

Another related phenomenon regarding superconducting materials is the quantization of magnetic flux. This effect was first predicted by London in 1950 [49] but observed only in 1961 [50]. The effect consists in the fact that in a superconducting ring the value of the magnetic flux is quantized in unities of $h/2e$. Actually the prevision by London was qualitatively correct but inexact since he didn't assume the factor $1/2$. In figure 1.7, the results from a 1971 paper are shown: it is plotted the trapped flux in a superconducting cylinder against the magnetic field in which it is cooled below its transition temperature. It emerges clearly that the curve is made of steps, indicating indeed the quantization of the flux. The explanation of the phenomenon follows the consequences of another superconducting effect which is the Meissner effect. Indeed, the definition of a superconductor is not related to the presence of persistence currents (since - as said - they can be present also in the normal phase) neither to the quantization of the flux. A superconductor is instead defined by the presence of the Meissner effect, which is the expulsion of the magnetic field from the sample, during its transition to the superconductive state when it is cooled below the critical temperature.

The Meissner effect thus implies that the magnetic induction $\mathbf{B}$ inside a superconductor below $T_C$ is always zero, even if an external field is applied. As a consequence, the probability current vanishes: $\mathbf{J} = 0$. Since it is possible, as we mentioned for fermionic gases, to write the wave function as

$$\psi(\mathbf{r}) = \sqrt{\rho(\mathbf{r})} e^{i\vartheta(\mathbf{r})} , \tag{1.23}$$

we can write the probability current per minimal coupling, and it follows:

$$\nabla\vartheta = \frac{q}{\hbar}\mathbf{A} \tag{1.24}$$

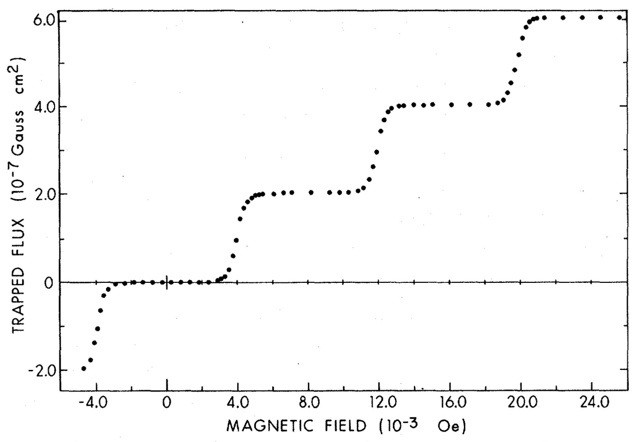


Figure 1.7: Quantization of the magnetic flux. Trapped flux in a superconducting thin cylinder is plot against the magnetic field in which it is cooled down below its critical temperature. Image from [7]

where **A** is the magnetic potential vector. Now by integrating over a close circuit and using Stokes theorem it is straightforward to derive the follow relation:

$$\Phi_B = n\frac{h}{q} \tag{1.25}$$

The charge here is the one of the Cooper pairs, so $q = 2e$ and we find the equation for the quantization of the flux.

In the so-called second type superconductors, quantization of the flux plays an important role: it does exist indeed a critical external magnetic field that - if exceeded - causes the field to penetrate into the superconductor even at temperatures below $T_C$. When it happens, the field is carried by normal conducting islands with a thin filament shape, called Abrikosov vortices. Each of these vortices carries a quantum of flux $\Phi_0$, and their number increases with the increment of the applied field. Nowadays, it is also possible to observe the disposition of these structures in superconductors thanks to scanning electron imaging techniques [51]. Each vortex consists of a normal core, which is indeed a non-superconducting cylinder with a normal phase and it has a diameter that corresponds to the superfluid correlation length $\xi$: the magnetic field lines use this channel to pass through the sample, and thus the core of the vortex plays the role of a hole in the superconducting phase.

### 1.3.2 Persistent currents in quantum fluids

Concerning quantum fluids, during the recent years an increasing attention has been paid to the generation of persistent flows in condensates. The most exploited and easy geometry in which excite currents in the annular one, i.e. a ring-shaped condensate. It was first proposed in 2005 [52] to experimentally realize a 1D closed optical lattice with the possibility of adding a tunable boundary phase twist in order to further study persistent currents. In that paper it was proposed to use a Laguerre-Gaussian laser beam, experimentally available by using computer generated holograms, and exploit its rotational symmetry to generate a ring-shaped potential for the atoms.

This method has been used in the recent years to excite persistent currents in bosonic condensates [16–18] to obtain an annular geometry. Then persistent current are usually excited with one of these two methods: a possibility is employing two-photon Raman transfer [19, 14] to give angular momentum to the condensate. Another very common way is achieved by "stirring" the condensate with a far off-resonance laser beam [53, 20] for enough time to make the atoms rotate.

Once excited the currents, their decay it has been also studied in Bose-Einstein condensates. In fact, it is possible to induce the decay of a persistent flow by tuning the temperature [21] or by adding different kinds of tunable barriers or weak links [16]. Studies on persistent flows find a lot of interest also in the field of atomtronics and quantum technologies, e.g. it has been demonstrated their utility in creating an atomic version of the superconducting quantum interference devices (SQUIDs) [22] during very recent years. So their usage has been proven to be helpful in quantum application but also it has been proposed [26] to further investigate physics of fermionic system e.g. probing the BEC-BCS crossover (see sect. 1.2).

Instead, the realization of persistent current in fermionic systems is still a great challenge, and only in 2021 the very first realization has been done [24]. It is reported in that work the creation of currents around a mesoscopic ring of ultracold fermionic $^6$Li atoms trapped by optical potential. They are in condition in which the currents are long-lived ($\gtrsim$ 10 sec) and with the possibility of tune the interaction strength by means of Feshbach resonances (see Appendix A). This feature allows to reversibly drive the system in and out the superfluid phase by going a bit far in the BCS side (since, as seen in sect. 1.2.1, the critical temperature $T_C$ decays exponentially with the interaction strength in the BCS regime). The idea of the experiment is thus to excite a current by stirring the superfluid, then to change the magnetic field which sets the interaction strength going into the normal phase, and at the end return into a molecular BEC (mBEC) superfluid to study the probability of survival of the current. In that paper, the persistence of the current after the sweeping out-and-in the superfluid phase, is attributed Hess-Fairbank effect.

What is most interesting is the way the current is detected. As shown in fig. 1.8, the circulation of the atoms is detected by looking at the topological defect which arises in the middle of the cloud. Before explaining how it happens, it is worth to briefly describe advantages and disadvantages of this method. Clearly detecting a vortex is a simple and efficient way, since it is only necessary to confirm or not the presence of a hole inside the cloud. On the other hand it gives only a partial information on the current: as a matter of fact, it is not possible to understand the direction of the circulation (clockwise or anticlockwise). Moreover, as we will now see the possible number of circulations is quantized, but it is not possible to distinguish if more than

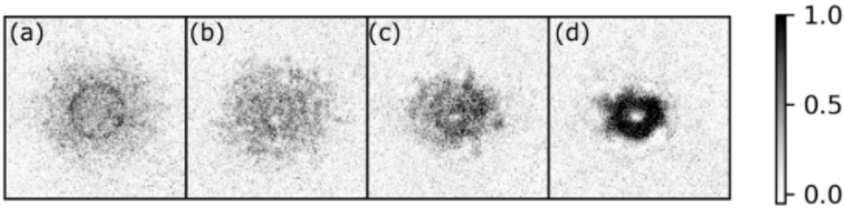


Figure 1.8: First realization of persistent currents in fermionic systems. Evolution of the density profile after absorption imaging is shown here; the current is detected by looking at the presence of a topological defect inside the cloud. Image taken from [24].

one circulations are applied. During this thesis I will present instead some methods of detection which require a better visibility but give more information on the system.

**Quantized circulation in rotating superfluids**

One of the most remarkable properties of superfluid and superconducting systems regards the quantization of the circulation which causes phenomena such as the creation of vortex lattices as seen in sect. 1.2.3. We will now show that the quantization of the circulation is an effect that directly follows the existence of a macroscopic wave function of the system.

As we've already seen, a fermionic superfluid can be described by a macroscopic wave function $\psi(\mathbf{r})$; it plays the role of order parameter, so it is zero valued in the normal phase and non-zero in the superfluid one. It can be written as:

$$\psi(\mathbf{r}) = |\psi(\mathbf{r})|e^{i\varphi(\mathbf{r})} \tag{1.26}$$

which is normalized so that

$$\int d\mathbf{r}|\psi(\mathbf{r})|^2 = N_0 \tag{1.27}$$

where $N_0$ is the number of condensed pairs (i.e. Cooper pairs in the BCS regime) forming the superfluid. It is thus possible to write the current density operator in the usual form

$$\mathbf{J}(\mathbf{r}) = -\frac{i\hbar}{2m^*}\left(\psi^*(\mathbf{r})\nabla\psi(\mathbf{r}) - \psi(\mathbf{r})\nabla\psi^*(\mathbf{r})\right) = n_0\frac{\hbar}{m^*}\nabla\varphi(\mathbf{r}) \tag{1.28}$$

where $n_0$ is the density of condensed pairs. Moreover, since we're dealing with fermionic superfluids, the mass which appears is the mass of the bosonic couples which is double of the mass of each fermion $m^* = 2m$.

Now a superfluid velocity can be defined in the common way since usually $\mathbf{J} = n\mathbf{v}$, and so the superfluid velocity reads:

$$\mathbf{v}_s(\mathbf{r}) = \frac{\hbar}{m^*}\nabla\varphi(\mathbf{r}) \tag{1.29}$$

from which follows that the velocity field is irrotational. From this point it is possible to derive the Onsager-Feynmann quantization condition [54–56]. It is indeed possible to integrate eq. 1.29 around a close loop inside the superfluid: since the phase $\varphi$ is defined modulo $2\pi$, it follows that

$$\Gamma = \oint \mathbf{v}_s \cdot \mathbf{dl} = \frac{\hbar}{m^*}\Delta\varphi = n\frac{h}{m^*} \tag{1.30}$$

where $n$, here is a positive integer value, and $\Gamma$ is the circulation.

By looking at eq. 1.30, it is clear that in case of a simply connected region of space in which the loop lies, we must have $n = 0$ if the superfluid wave function has no nodal lines in the loop. Otherwise, solutions with $n \neq 0$ are possible with the formation of topological defects i.e. vortices. If a vortex forms, the superfluid wave function vanishes in the vortex core, and has there its nodal lines. In this way the superfluid is able to carry angular momentum.

Assuming that the flow is only dependent on the angular coordinate in a cylindrical coordinates frame, and by taking into account uniform flow (meaning $|\psi| = \text{const}$ inside the superfluid) it is possible to derive the expression for the phase of the superfluid, which happens to be linear with the angular coordinate $\vartheta$:

$$\varphi(\vartheta) = n\vartheta + \text{const}\ . \tag{1.31}$$

Under the same assumptions it follows that the superfluid velocity around the topological defect is inversely proportional to the core distance:

$$\mathbf{v}_s(r) = n\frac{\hbar}{m^*}\frac{1}{r}\hat{\mathbf{e}}_\vartheta\ . \tag{1.32}$$

**Analogy between superconducting systems and fermionic superfluids**

It becomes clear so far a strong analogy between what happens in superconductors and the phenomena related to the persistent flows in fermionic superfluids. Both the phenomenology and the physical drivers are comparable: in the first case there is a quantize quantity that is the magnetic flux trapped in the superconductor, which is driven by a gradient of the phase of the superconducting wave function. The phase is indeed associated to the external applied magnetic field thanks to the magnetic potential vector. On the other side, in case of fermionic superfluids, the quantized quantity is the circulation, and it is related to the gradient of the phase of the superfluid wave function through the superfluid velocity. In both cases (focusing on type-II superconductors in detail) the phenomenology brings to the formation of topological defects in which the order parameter vanishes, through which the superfluid/superconducting phase can carry the associated quantity (angular momentum/magnetic flux).

These analogies also confer a greater relevance in the study of fermionic superfluids: they are often extremely controllable system in which it is possible to investigate deeply the physics which underlies also the mechanisms driving different kind of superconducting materials.

# Chapter 2

# Methods

In this chapter we are going to discuss the methods to create, manipulate, and study ultracold quantum fermionic gases. Atoms have to be evaporated and cooled to reach degeneracy, then they are manipulated by means of optical potentials; finally an absorption imaging is taken to have a direct picture of the gas. We will proceed by describing the experimental apparatus which permits the creation of fermionic superfluids of $^6$Li. Then a characterization of the system will be provided, discussing interesting way to manipulate and the atoms in desired geometries. Once trapped, a current can be imprinted on the atoms with the phase imprinting technique and finally it will be explained how interference methods can be employed to obtain information about fermionic condensates.

## 2.1 Experimental apparatus

An exhaustive description of the experimental apparatus used in this work, has already been performed [57–59], so we will limit ourselves in recalling the fundamental steps in creating and cooling the gas. The basic process consists of the procedure described in the following. First of all, Lithium-6 is evaporated in the oven and then expelled by a thin nozzle; here the atoms enter in the Zeeman slower, where their velocity indeed reduces to arrive in the science chamber. Now, a magneto-optical trapping is performed before using evaporative cooling to reach temperature around tenth of nanokelvin. At this point, the gas is loaded in an oblate geometry and then it is manipulated with optical potential imprinted thanks to a digital micromirror device (DMD). Finally, the measurements consists in taking a picture of the gas with an high resolution imaging system.

In figure 2.1, a picture of the experimental apparatus is show; we will proceed the narration following the image from left to right i.e. from the genesis of the atoms to the effective measurements of the gas properties.

Clearly everything happens in ultra-high-vacuum (UHV) conditions, using a system isolating cold atoms from hot thermal background ones.

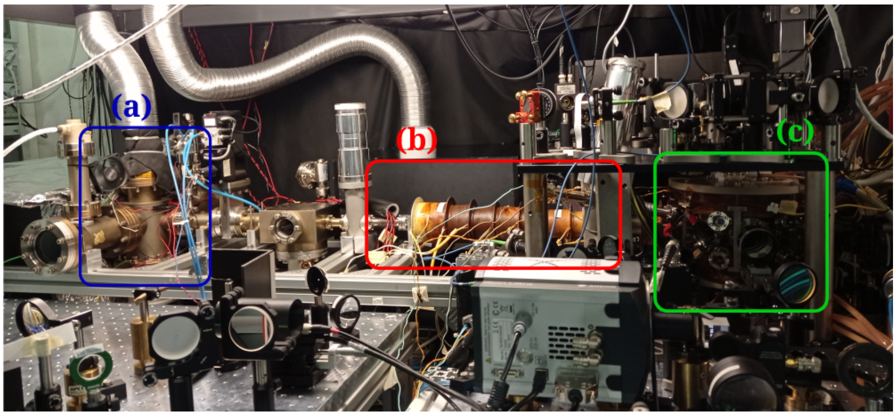


Figure 2.1: Picture of apparatus for production of ultracold fermionic gases. An overall view of the ultra-high-vacuum system is given: first lithium atoms are loaded in the oven (a), then expelled through a nozzle; they are then decelerated in the Zeeman slower (b) in order to be trapped in the science chamber (c). Image from [57]

### 2.1.1 Genesis of the gas

**Oven** Lithium at room temperature is in a solid state. To obtain a significant vapor pressure it needs to be heated up to temperatures above 400 °C. In our system samples of artificially enriched $^6$Li is held in a cup at 430 °C. The vapor flow is then collimated and expelled through a thin nozzle. In order to avoid obstructions, the nozzle is heated up to 460 °C. The flow is then collimated further by a cooper cold finger.

**Zeeman slower** Atoms need now to be decelerated in order to enter the science chamber and be trapped by the magneto-optical trap (MOT). Intending to achieve strong deceleration, we employ a Zeeman slower [60, 61], which is able to decrease atom velocity from 800 m/s ca. to a final velocity of 30 m/s.

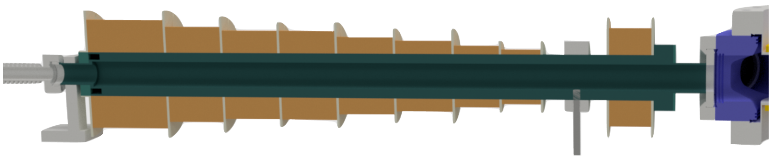

Figure 2.2: Image from [57]

A representation of the structure of the Zeeman slower is given in figure 2.2: it is a tube wrapped in 9 coils carefully designed to obtain a spatially inhomogeneous magnetic field. The idea is to combine the action of a counter propagating laser beam resonant with the $D_2$ transition (see Appendix A), with that of the magnetic field. The task of the magnetic field is to always keep the atoms resonant with the incoming laser beam, which propagates in the opposite direction with respect to the lithium flow. It is needed because the deceleration causes a different intensity of the Doppler shift along the tube.

The Zeeman slower in the apparatus is in a spin-flip configuration: in fact, the magnetic field profile passes through zero value, causing some atoms to depolarize and forces the usage of a repumper light to recover those atoms. In this way, at the end of the tube, the atoms are off-resonant with the laser beam and ready to enter in the science chamber.

**MOT** Once atoms are inside the science chamber, they are trapped by a magneto-optical trapping system (MOT). A pair of coils in anti-Helmholtz configuration are used to generate a quadrupolar magnetic field: by combining it with three pairs of counter propagating laser beams (one for each direction), at the same time a trapping and a cooling of the atoms will take place [62]. During this stage it is usually possible to trap around $10^9$ atoms with a temperature of the order of 500 $\mu$K. This process is 7-9 sec long. Still, there is a lower theoretical bound for cooling atoms in the MOT, which is the Doppler temperature. For our $^6$Li atoms, this value is $T_D = 140$ $\mu$K. Therefore, another cooling process takes place right after switching off MOT laser beams, which consists of gray molasses acting on the $D_1$ transition to achieve a sub-Doppler cooling [59]. After this process the gas temperature is around 50 $\mu$K.

In order to adjust spatial position of the gas with regards to the next optical traps, some compensation coils are also placed. There is a pair of coil in a similar Helmholtz configuration for each direction, in order to make possible to shift the center of the MOT in any direction.

**Crossing trap and evaporative cooling** The next step is the loading the gas in a Optical Dipole Trap (ODT) generated with an IPG laser. This high power (max 200 W) beam, having 1070 nm wavelength, enters in the science chamber with an angle of 7 degrees respect to the MOT beam. Once IPG is on, a fast modulation of the central frequency and the amplitude of the IPG's AOM is performed, in order to catch more atoms from the MOT.

Once atoms are loaded in the IPG, a second stage of gray molasses is performed in the trap; then we ramp the magnetic field (generated by some Feshbach coils) up to 834 G, which is the top of the $|1\rangle - |2\rangle$ resonance. Here it is then performed evaporation in order to produce fermionic superfluids. Finally, the IPG is crossed with a Mephisto ODT, which has an angle of 14 degrees respect to the IPG, and a wavelength of 1064 nm. The so-built trap assumes indeed a cigar shape which contains 100-200 thousand atoms at temperatures of the order of 20 nK.

Once the evaporation is over, it is possible to change the field applied by the Feshbach coils in order to change the interaction strength by acting on the scattering length (see Appendix A); it is thus possible to explore different regime across the BEC-BCS crossover (in fig. 2.3, some examples of cigar trapping plus $\mathrm{TEM}_{0,1}$ for UFG and BEC are shown).

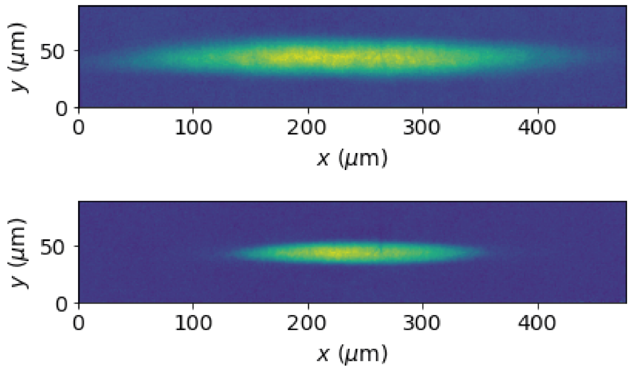


Figure 2.3: Images of fermionic superfluids in harmonic trap. The density distribution of the gas is shown in the Unitary (upper) and BEC (lower) regime. Gas are captured in the crossing trap and then loaded in the $TEM_{0,1}$; at the end, a vertical absorption imaging is taken.

### 2.1.2 Loading in the $TEM_{0,1}$

During recent years, increasing interest has showed up in studying ultracold gases in homogeneous traps. Indeed, in the usual harmonic trap the translational symmetry is broken, and moreover the nonuniform density can undergo spatially variations in energy and length scales. This is actually a non negligible problem in studying critical phenomena for which the correlation length diverges. To overcome this problem uniform trapping potentials seem to be a good solution, and they've been used to create both uniform Bose-Einstein condensates [62–65] and fermionic gases [66].

In order to create quasi homogeneous fermionic gas in our experimental setup, we employ two main methods: concerning the vertical direction, we apply a $TEM_{0,1}$ beam to squeeze the atoms, and then we shape them with a digital micromirror device. For both the methods we employ a 532 nm light originating from a Coherent Verdi V-8 laser, which acts as a repulsive potential for $^6$Li atoms.

The $TEM_{0,1}$ beam is designed to squeeze the gas in the vertical direction; by varying the power of the beam, different regimes are available to be explored. It is thus possible to vary from an oblate regime to a quasi 2D regime at high power (2 W). This beam has a waist of $\sigma = 8.73\ \mu$m in the z direction, and a 400 $\mu$m waist in the y direction. The beam profile is shown in figure 2.4a: by providing confinement in the vertical direction, it also helps in compensating the residual harmonic trap produced by the Feshbach field of about 8 Hz (at high power).

The effect of the $TEM_{0,1}$ on the atoms is shown in figure 2.4b: acting as a repulsive beam, the atoms gets trapped inside the intensity node and so the gravity is defeated. The condition in which $TEM_{0,1}$ is used in this work is the low power regime, in which

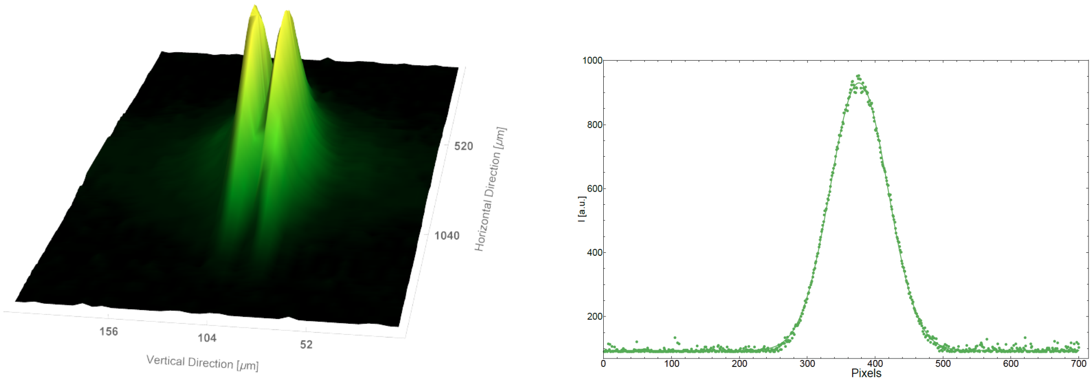


(a) (b)

Figure 2.4: $TEM_{0,1}$ beam profile (a) is shown: since the 532 nm light act as a repulsive potential, the atoms are squeezed in the vertical direction resulting in a density profile (b) which is Gaussian with a waist of $\sigma$=8.73 nm

the gas is oblate and a good number of atoms is preserved without interfering in the homogeneity of the density profile.

### 2.1.3 High resolution objective

It is possible to manipulate the obtained superfluid it by means of optical potentials. An essential tool to achieve this goal is the presence of an high resolution objective which allows to reach the sub-micrometer precision in spatial resolution. For the characteristics of the objective and the setup we refer to [38]. This is a fundamental tool also for the imaging technique: indeed, both DMD and imaging beams pass through the objective which focuses the light on the atomic cloud.

The objective we employ is custom made by Special Optics, and its optical properties are listed in tab. 2.1. It is designed to feature the same focal point for both resonant light at 671 nm and blue-detuned light at 532 nm, so that it can be employed not only for imaging in absorption the atomic cloud at high resolution, but also for imprinting optical potentials from the DMD defined over a micrometer length scale.

In particular, to compute the resolution of the objective, a good practical quantity to be calculated is the full width at half maximum (FWHM) of the point spread func-

| | |
|---|---|
| Numerical Aperture (NA) | 0.45 |
| Effective focal length | 47 mm |
| Field of view | 0.33 mm |
| Working distance | 25.1 mm |
| AR coating | 670 nm, 532 nm, 1064 nm |

Table 2.1: High-resolution microscope objective optical properties.

tion (PSF), which fully characterizes any composite imaging system. This definition extends the validity of the Rayleigh criterion also in presence of aberration. It is possible to compute the FWHM as FWHM $= 0.51\frac{\lambda}{\mathrm{NA}}$. The resulting expected FWHM for the microscope objective is thus 760 nm for $\lambda$=671 nm, and 603 nm for $\lambda$=532 nm. It is possible to also characterize experimentally the objective features and the following results have been found: the resolution of the objective is observed to be almost constant over a region of about 150 $\mu$m radius, which is compatible with the nominal field of view of 300 $\mu$m of the objective. The measured resolutions are instead 630(10) nnm for $\lambda$=532 nm and 830 at the wavelength of $\lambda$=671 nm. Both the resolutions agrees with the nominal ones within 10%. It has been also verified that the focal length of the objective is the same at 532 nm and 671, and finally the total magnification of the composite optical system is measured to be $M = 21.8$.

### 2.1.4 DMD for arbitrary optical potentials

As mentioned, arbitrary optical potentials are applied thanks to a digital micromirror device; the structure of the device is shown in figure 2.5: it consists of a $1024 \times 768$ array of pixel, where each pixel is a square micromirror of pitch 13.68 $\mu$m. It is possible to control the inclination of each micromirror by the application of external voltage: as a consequence, the pixel changes its status. Three states are available, as depicted in figure 2.5(b): when the DMD is OFF, and no external field is applied, the pixels are not tilted and stay in the rest mode, otherwise +12° and -12° configurations are allowed, corresponding respectively to ON and OFF states. When a pixel is ON, the incident light is reflected to the atoms, otherwise it is not.

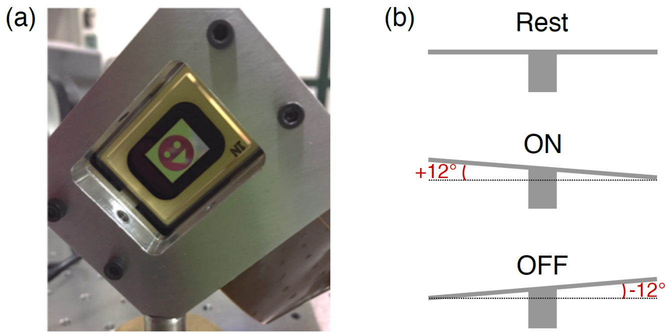


Figure 2.5: DMD structure. The device consists mainly of a chip which is composed of a $1024 \times 768$ array of pixel. Each pixel is a digital micromirror in which three configurations are available (b): rest, ON, and OFF. In case an external voltage is applied, the desired micromirror tilts to shine - or not - the light on the atoms. The desired potential is given in input to the DMD as a binary image which is then reflected (a) on the sample.

The arbitrary optical potential is passed to the DMD as a binary image (e.g. the smile in fig 2.5(a), and the reflected image is projected on the atomic cloud. Since the light source is blue-detuned beam at 532 nm, it acts as a repulsive potential for the atoms. As a matter of fact, the laser beam has a Gaussian shape, and the DMD acts as a mask in reflection, thus also the potential applied to the atoms result in a Gaussian profile. Since in usual application this light profile is not suitable (e.g. for moving an obstacle, shaping the cloud, or adding a barrier), a feedback program is needed to overcome this problem and obtain uniform potential. The idea is to shine the light on a camera first, and then adjust the state of the pixel by the comparison between the obtained image and the target one. To achieve the goal, a pixel-by-pixel error correction matrix is applied on the on the DMD mirror array configuration, so that the error between the two images is minimized: the result is an homogeneous profile over a large area ( 120 $\mu$m).

One of the most useful properties of the DMD is the possibility to create also dynamical potentials. The DMD has indeed two modalities in which it can be run: a static image can be applied or a dynamical sequence of images can be given as input. The input can be an arbitrary long sequence of images which are triggered by an input set to the device by the control program. The time between two different images is called *Picture Time* (PT). The maximum frame rate allowed in the running modality is 22 kHz, corresponding to a minimum PT of 44 $\mu$s. Anyway the Picture Time can be tune willingly from its minimum value to any desired timing with regards to the potentials to be applied.

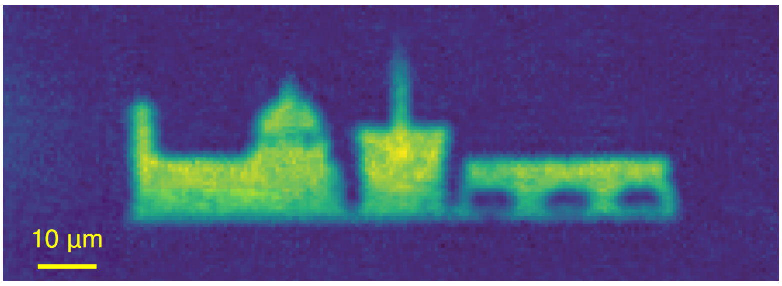


(a) Florence skyline: from left to right the Florence cathedral is visible, with Giotto's Campanile and Brunelleschi's Dome, Palazzo Vecchio and Ponte Vecchio bridge.

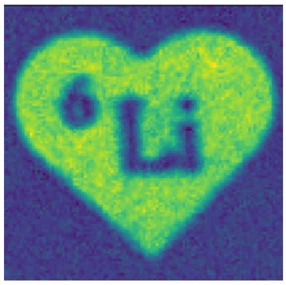


(b) Arbitrary heart shaped atomic cloud with arbitrary text.

Figure 2.6: Arbitrary optical potential with the DMD. Thanks to the high resolution achieved, it is possible to generate arbitrary uniform optical potential on the atoms, in order to create the desired shapes and geometries.

Therefore it is possible by combining $TEM_{0,1}$ beam and the DMD, to produce arbitrary uniform optical potential: after the gas is loaded in the cigar trap, it is squeezed vertically by the $TEM_{0,1}$ and then the DMD is ramped on with the desired image. Some examples are shown in figure 2.6: it is possible to generate a Florence skyline atom density distribution or any other desired shape. Moreover an iris is placed before the high resolution objective so that it is possible to tune the spatial resolution and obtain smoother or sharper optical potentials.

### 2.1.5 Imaging technique

All the measures that we are able to extract from the sample, such as number of atoms, temperature or density distribution, are derived by analyzing the image of the atomic cloud. In order to take an image, an high intensity absorption imaging is performed. The image of the sample is acquired shining high power resonant light to the atoms and then collecting the resulting shadows. By using two different optical paths, it is possible to perform horizontal or vertical imaging.

The horizontal one is less sophisticated and used mainly for calibrations. It has a magnification of 6.87 and it runs in Fast Kinetic Series (FKS) mode, so that it is able to capture three images with the short delay time of 200 $\mu$s, by using one third of the chip dedicated to each image. The camera pixels are $16 \times 16$ $\mu$m, so taking into account the magnification they correspond to 2.3 $\mu$m side square on the atoms. Another low magnification (0.5) camera can be placed manually in the optical path in order to check the loading of the gas in the MOT.

The vertical imaging is indeed the most sophisticated one. As for the DMD, the high resolution objective is implemented to focus the light on the atoms. It allows to reach a sub-micrometer resolution in the imaging setup (where the resolution is defined as the minimum distance for which two objects appear separated in the imaging plane). The total magnification achieved with the optical setup for the vertical imaging is 21.8; since the camera pixel are $13 \times 13$ $\mu$m, each pixel corresponds to a 0.6 $\mu$m square on the atoms. Also in the vertical direction, the camera is used in FKS acquisition mode by capturing three images with a very short delay time. This procedure is necessary to obtain information from the images, since from the Lambert-Beer law it is clear that the atomic density (integrated over the vertical direction) depends on incident and transmitted intensities:

$$n_{2D}(x,y) = -\frac{\alpha}{\sigma_0} ln\left(\frac{I_{out}}{I_{in}}\right) + \frac{\alpha}{\beta}\frac{1}{\sigma_0}\frac{I_{in} - I_{out}}{I_s} \; . \tag{2.1}$$

In equation 2.1, $\sigma = \frac{3\lambda^2}{2\pi}$ is the ideal value of the absorption cross section, while $\alpha$ and $\beta$ are parameters which relate the saturation intensities to ideal and effective cross section respectively. $I_s$ is the intensity of the resonant light which we shine on the atoms. Finally $I_{in}$ and $I_{out}$ are incident and transmitted intensities. It is possible to obtain them by analyzing the three images: we remove the third image (the background) from the other two, then the incident intensity is obtained from the second image (just light without atoms), and the transmitted light is the one collected in the first image i.e. the part of the beam which is not absorbed by the atoms.

A representation of the main discussed features acting in the science chamber is given in figure 2.7: both vertical imaging and DMD share the same final optical path to reach atomic sample, thanks to the high resolution objective which focuses both resonant light at 671 nm and blue-detuned light at 532 nm. More details on objective and imaging setup can be found in ref [38].

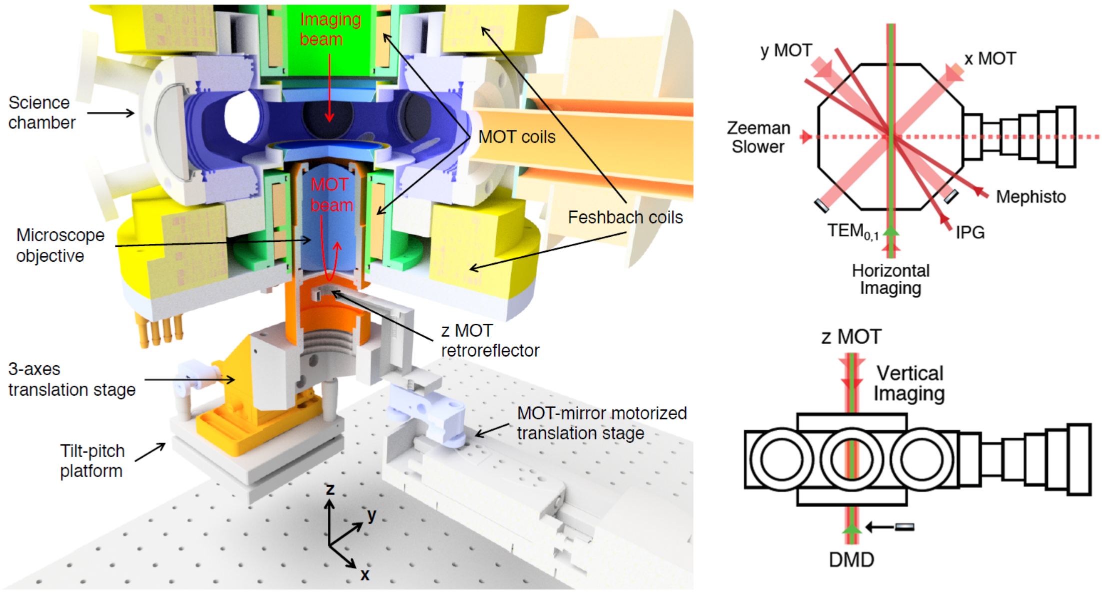


Figure 2.7: Representation of the science chamber. On the left panel a 3D scheme is show: around science chamber MOT coils and Feshbach coils are winded, while laser beams can enter thanks to openings on the sides and on the top/bottom of the chamber. The high resolution objective is places in the optical path of both DMD beam and vertical imaging. On the right panel a more schematic representation of the laser beams inside the chamber is given (above a view from the top while below a section seen from the side): a first confinement is due to the 3-dimensional MOT beams after the atoms are decelerated by the Zeeman slower. Then the gas is trapped by a crossing of Mephisto and IPG laser beams, before being loaded in an oblate geometry thanks to the $TEM_{0,1}$. Once in the oblate geometry, arbitrary optical potentials can be applied by the DMD, and the atomic cloud is finally imaged by integrating vertically the absorption light.

## 2.2 Ring geometry and characterization

The main focus of this work concerns a particular geometry in which atoms are shaped, that is the annular one. By employing the DMD and the $TEM_{0,1}$ beam, it is possible to imprint any desired shape on the atomic cloud. A very interesting geometry in which it is possible to study persistent currents is the annular one, i.e. a ring-shaped geometry. Actually the ring geometry is very interesting for investigate different fields of superfluidity, such as Josephson effect, phase fluctuations, high-precision Sagnac or gravitational interferometry [67], and also Kibble-Zurek mechanism [68]. Some other fancy applications regard the construction of a mode-locked atom laser [69] and the creation of sonic black holes in tight ring-shaped condensates [70]. The investigation is led both experimentally and theoretically [71–73]; indeed this is the most practical geometry in which periodic boundary conditions can be really implemented, making closer the possible theoretical calculations with experimentally accessible physical quantities.

The goal of this section is thus to explain how we generate a ring geometry on the atoms. Since in a ring shape, the first excitation modes concern the rotation of the atoms, some space will be dedicated to show how we prepare a very still cloud of atoms.

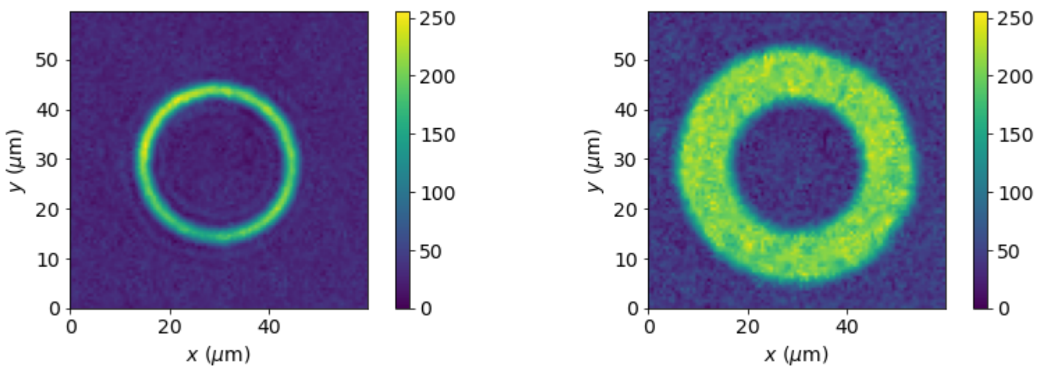


(a) 3.7 $\mu$m width ring.

(b) 10.3 $\mu$m width ring.

Figure 2.8: Realization of tunable annular fermionic superfluids. Thanks to the use of the DMD it is possible to manipulate the atoms to obtain tunable ring geometries, from a 1D-like (a) to ticker ones (b).

As we explained, thanks to the DMD it is possible to generate arbitrary optical potentials on the atoms (see sect. 2.1.4). Moreover, we employ a $TEM_{0,1}$ beam which helps to obtain an uniform confinement (see sect. 2.1.2). In this way we are able to create tunable ring geometries as shown in fig. 2.8: it is possible to create very thin rings (2.8a) which mimic a 1D geometry with periodic boundary conditions very well; on the other side we can decide to work with more atoms in ticker rings, in which the radial motion is not completely suppressed.

In order to perform a characterization, some information are needed about the ring; for example the DMD center should be fixed, but it can undergo to day-to-day fluctua-


Figure 2.9: Image processing to detect the center of the ring. First some blur is applied (a) to the image in order to denoise and process the edges, then it is transformed in binary image (b), in order to detect the contours and save them (c). Finally, chosen the right contours, it is possible to fit them with two circumferences and average the obtained centers.

tions. Moreover, the ring's width is set in DMD pixel units, and it is not straightforward the exact conversion since a bit of resolution is loss due to the closure of the iris [1]. Finding the center of the ring is very useful also in order to unwrap it, which is a basic step for many procedures as we will see in a while and in chapter 3.

In order to find the center and the radius of the ring, we perform some image post-production as shown in fig. 2.9: first, a median $5 \times 5$ blur is applied, meaning that each pixel is replaced by the median value over a square of $5 \times 5$ pixel around it. This step is used for processing the edges while removing the noise. Then another simple blurring with a larger kernel ($7 \times 7$ pixels) is applied to further smooth the image and prepare it to edge detection. The result of these two blurs is show in figure 2.9(a). Then, a threshold is carefully chosen and applied, so that the image con be converted to a binary image (fig. 2.9(b)). It is now possible to detect the contours by using the `findContours` function from `OpenCV` library in Python, and obtain an array with the contours of the image (fig. 2.9(c)). Just the first two contours are needed, i.e. those delimiting the ring, and they can be fitted with two circumferences. The final center is obtained by averaging the centers of the obtained circles (red and blue crosses in fig. 2.9(d)) and the width of the ring is given by the subtraction between the two radii.

It is now possible to unwrap the ring from its center and transfer the radial and angular coordinates into Cartesian ones. An example is provided in fig. 2.10. The ring shown in figure corresponds to the geometry used in this work, with the following characteristics: the inner radius is 9.94 $\mu$m wide, the external one has a width of 20.22 $\mu$m, resulting in a ring width of 10.28 $\mu$m. In fig. 2.10 it is also shown the radial density profile at different angular cuts. A black line represents the average over all the cuts, and it is possible to see that a quasi-homogeneous annular geometry is achieved.

The final question we have to discuss is the creation of the trap. First of all, in order to perform detection methods based on interference, a reference is needed. As

[1]We decided to keep the iris close (see sect. 2.1.4) for reason that will be explained later in section 2.3. We loss a bit of resolution but we confirmed the no result depend on the iris closure ar opening.

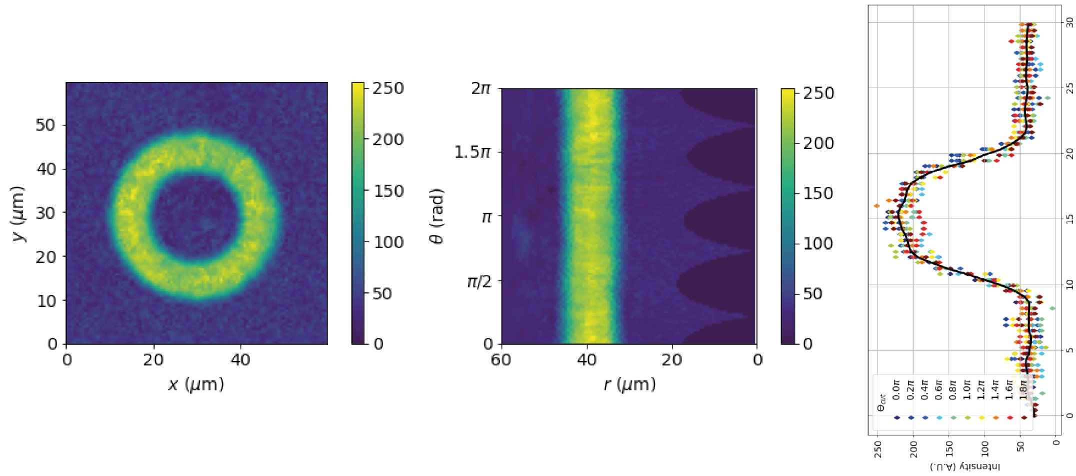


Figure 2.10: Annular geometry characterization. In the left panel the final chosen ring for measurements is shown, whose width is about 10 $\mu$m. In the central panel it is visible the unwrapping of the ring in Cartesian coordinates. On the right panel the radial density profile is plotted for cuts at different angles: each color stands for an angle and the average is represented as a black solid line.

a reference, we add a disc inside the ring, separated with a 2.4 $\mu$m barrier which - we verified - creates an hole in the density. The barrier width is tunable, therefore to perform some kind of measurements it has been used a larger barrier i.e wide 6 $\mu$m. Since it is very easy to excite rotational movement in an annular geometry, we optimized a method to load the atoms in the trap so that at the end of the procedure the gas is very still. The procedure is represented in fig. 2.11 and it consists of the following steps. First the gas is loaded in two hemispheres which are separated by a 2.4 $\mu$m wide barrier. The height of the barrier is well above the chemical potential, so there is effectively an hole in the density profile. At this point a circular barrier is ramped up adiabatically in order to avoid creation of any kind of excitations. The time-step used is 0.1 ms, which is the delay time of DMD's action of switching images (PT) (see sect. 2.1.4), and 15 steps are employed to reach the final barrier height. After waiting 40 ms, the next step is performed, so the stopping barrier which used to divide in the the cloud is ramped down. Also in this case the operation is done adiabatically, with a PT of 5 ms. This operation requires 15 steps to be completed and, at the end, the gas is still in the trap and ready to be further manipulated.

The methods we employ to verify that no rotational movement takes place at the end of the loading in the trap, is the one based on interference and will be explained in chapter 3.1. The optimization of every parameter has been done by checking if any unwanted excitation forms, and by finding the correct ranges in which it is possible to create a very still gas.

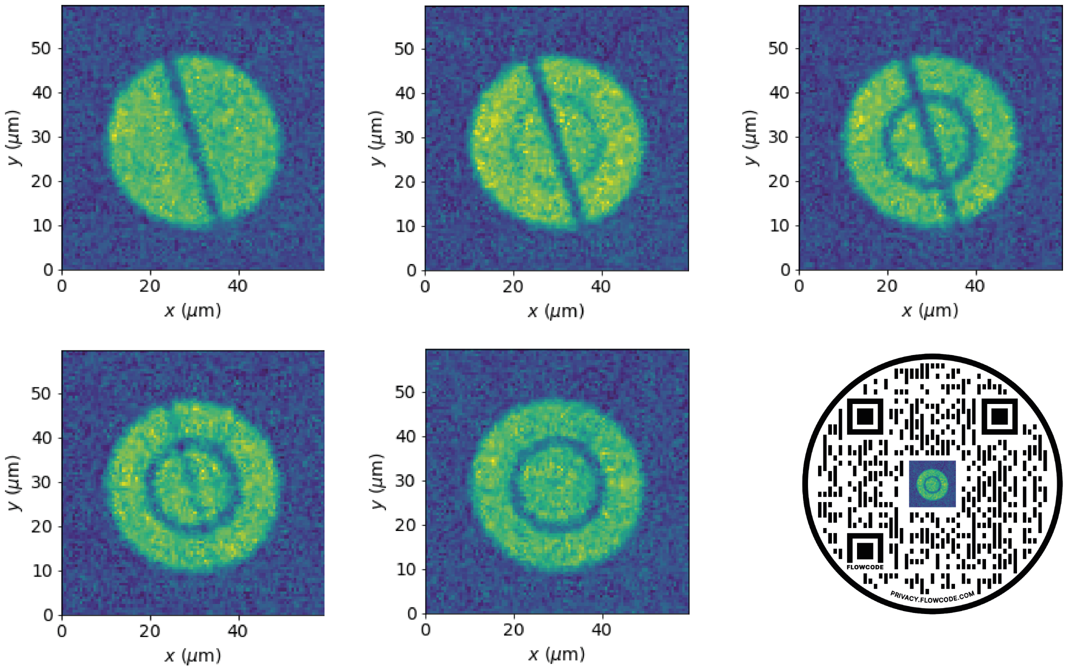


Figure 2.11: Procedure for the creation of the trap. The trap is created by loading two hemispheres on the atoms. Then, a round barrier is ramped up in 15 steps with 0.1 ms PT, and the linear "stopping" barrier is ramped down in 15 steps with 5 ms PT. An animated gif of the creation of the trap is available by scanning the QR code.

This is how the gas is trapped in the desired geometry, now it can be moved. In the next section it will be discussed how we are able to confer an angular velocity to the atoms to make them rotate and study the persistent current phenomenon.

## 2.3 Phase imprinting technique

Usual methods to make a superfluid rotate have been discussed in ch. 1.3.2, and mainly consist in stirring the atoms with a laser beam or give them angular momentum through a two-photon Raman transfer. Although these methods are quite reliable in giving a well-defined winding number $W$, they are restricted to low $W$ values; moreover the preparation usually takes long time, which can be quite an issue if the lifetime of the sample is short or if fast operations on the wavefunction have to be performed. The technique we are going to present is instead based on the idea of imprinting a phase to the atoms by shining the cloud with an optical potential for a very short time; this technique is indeed called phase imprinting.

The phase imprinting method was first proposed in 1999 [74] for generation of vortices in Bose-Einstein condensates and the employed in studying dark solitons in BECs [75, 76]. The concept is to employ a far off resonant laser beam, in our case a blue-detuned 532 nm beam, and shine it on the atoms. As we will see below, if the application time (i.e. imprinting time) is fast enough, no density perturbation should appear in the condensate, just a modification of the macroscopic wave function's phase. More recently, this technique has been studied and proposed to imprint circulations in superfluids [77], which is very similar to the approach we are going to follow. A big difference consists in the fact that their proposal includes the usage of a barrier in order to make everything work, that it is not needed in our system thanks to the high resolution achievable.

Now basic concepts of phase imprinting will be explained. Since our geometry is annular we will work with polar coordinates. We shine a far-off-resonance laser beam on the sample, which has a spatial variable intensity profile $I(r, \vartheta)$ on the plane. When pulsed, it gives rise to a potential on the atoms

$$U(r, \vartheta) = \alpha I(r, \vartheta) \tag{2.2}$$

which is linearly proportional to the local beam intensity. The factor $\alpha$ is proportional to the polarizability and it can be written in a two-level atom approximation as:

$$\alpha = \frac{\Gamma}{\Delta} \frac{\hbar\Gamma}{8I_s} \tag{2.3}$$

where $\Delta$ is the detuning, i.e. the difference between the frequency of the incoming light and that of the atomic resonance, $\Gamma$ is the transition line width, and $I_s$ is the saturation intensity. When shining the light on the atoms for a time $\tau$ which is much smaller than the timescales playing a role in the system, it is possible to write the final wave function of the system as:

$$\psi(r, \vartheta, \tau) = e^{-\frac{i}{\hbar} U(r,\vartheta)\tau} \psi_0(r, \vartheta) \tag{2.4}$$

where $\psi_0(r,\vartheta)$ is the initial wave function of the ground state. Thus, the effect of the imprinting is just to add to the ground state wavefunction the phase:

$$\varphi(r,\vartheta) = -\frac{U(r,\vartheta)\tau}{\hbar} = -\frac{\alpha}{\hbar} I(r,\vartheta)\tau \tag{2.5}$$

At this point it is clear that it is possible to arbitrary imprint a phase on the atoms by employing the suitable planar intensity profile. By recalling what discussed in ch. 1.3.2, and in particular equations 1.31 and 1.29, we know that a linear phase profile would produce a velocity field in the angular direction. It means that we can apply a linear intensity profile to obtain the circulation of the atoms.

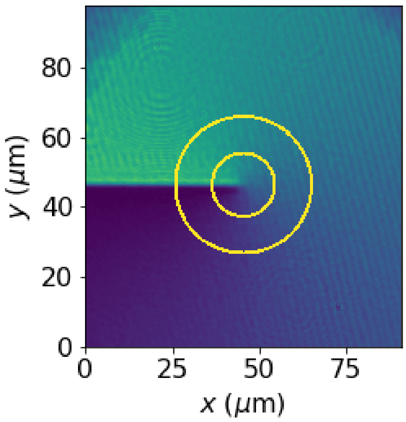


(a) Image of the profile imprinted with the DMD. Just the yellow ring-shaped mask is cut and applied to the atoms to make them rotate.

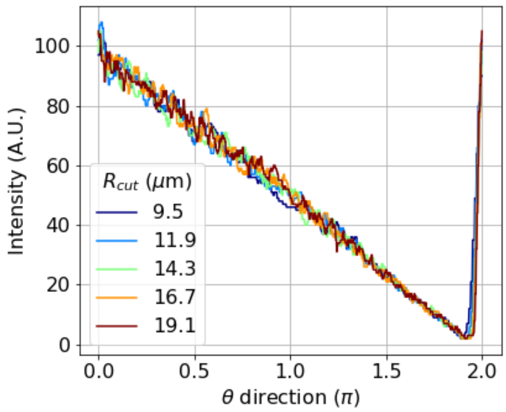


(b) Angular intensity profile for different radial cuts is plotted after the feedback has been performed to obtain a linear profile.

Figure 2.12: Gradient profile of the applied intensity beam. With the DMD it is possible to imprint a linear (b) phase profile on the atoms. From the whole image we cut (a) only the region of interest to imprint a circulation to the atoms in the annulus.

We will thus employ a phase dependence which is linear on the angular variable $\varphi(r,\vartheta) \propto \vartheta$, as shown in fig. 2.12; it is there provided the shape of the light profile we shine on the atoms: with the DMD, the distribution in fig. 2.12a is generated. Then, we select only the region of interest (i.e. the one between the two yellow circumferences) and we shine it on the atoms for a variable time $\tau$. A feedback has been performed on the image sent from DMD, in order to obtain a truly linear profile (as in fig. 2.12b is plotted). In figure, some cuts at different radii are shown: in the region of interest for our geometry the linear profile is always well defined. It is also worth to point out the high resolution of the anti-gradient in fig. 2.12b which enables us to work without adding a barrier in correspondence to the phase jump.

The other parameter which plays a role in equation 2.5 is the imprinting time $\tau$. Since superfluid velocity depends on the gradient of the phase $v_s(r,\vartheta) = \frac{\hbar}{m}\nabla\varphi$, the im-

| | B (G) | $1/k_F a$ | $\nu_z$ (Hz) | $\tau_z$ (ms) | $\hbar/\mu$ ($\mu$s) |
|---|---|---|---|---|---|
| BEC | 702 | 5.53 | $396 \pm 2$ | 2.5 | 155 |
| UFG | 834 | 0 | $523 \pm 8$ | 1.9 | 35 |
| BCS | 862 | -0.42 | $470 \pm 6$ | 2.1 | 20 |

Table 2.2: Properties of the gas used in this work with associated timescales. From left to right: magnetic field, interaction parameter, vertical trap frequency and period, and characteristic timescale are reported for each regime of fermionic superfluidity.

printing time acts in changing the applied winding number. Thus, by using lower imprinting times we are able to excite lower states of circulations, but also higher winding number can be imprinted by increasing the time duration of the pulse. As mentioned, it is important to keep in mind the limits in which this procedure is valid, i.e. the imprinting time must be much lower than the trap frequencies [77].

In the context of this work, the three fermionic superfluid regimes are explored and for each one has been measured its trap frequency. The fastest one, so the one that gives the upper limit, is the vertical frequency which assumes the values reported in tab. 2.2.

In the table, we compare also another timescale playing a role which is the the response of the atoms to an external stimulus. The time scale is set by $\hbar/\mu$ and it is actually the most restricting one.

As a matter of fact, it is impossible to imprint for a time shorter than $\hbar/\mu$ in UFG and BCS regimes due to the minimum delay time of our DMD; anyway, we have verified that, working inside the reasonable ranges in which $\tau_{\text{imprinting}} \ll \tau_z$, phase imprinting is a powerful tool which allows to generate arbitrary circulation in a deterministic way, as will be explained in the following of the thesis. We are going to conclude this chapter with an introduction to the method employed to detect the motion of the atoms.

## 2.4 Detection by interference methods

Since the first experimental realization of interference between two Bose-Einstein condensates [78], a lot of experimental and theoretical efforts have been devoted in studying and analyzing properties of the interference [79–87]. During the recent years, interference methods have been proposed [88] and realized [89] also for fermionic gases, in order to explore a lot of properties of the systems, even not trivial ones such as the vector nature of the order parameter are predicted to be accessible [90].

### 2.4.1 Interference in Bose-Einstein condensates

The very first interference pattern between two condensates was seen in 1997 at the MIT: they created to condensates by evaporating sodium atoms in a double well potential, so that the separation was 40 $\mu$m. After a 40 ms time-of-flight (TOF) the trap

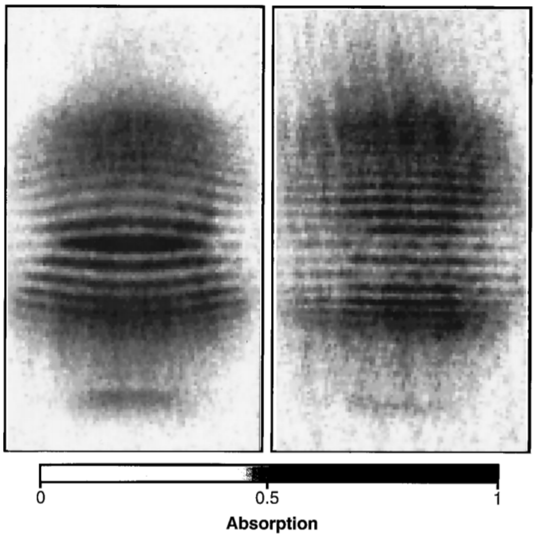


Figure 2.13: First observation of interference pattern in BEC. Two condensates are prepared in a double well potential with a separation of 40 $\mu$m; then, the trap is released and the condensates are allowed to expand and overlap. The presence of the fringes is an evidence that condensed Bose atoms are coherent and show long-range correlations. Image from [78].

was released and the gas was let expand and overlap. Then, an absorption imaging is performed and the results are reported in fig. 2.13.

In fig. 2.13 it is possible to observe the presence of fringes when the two condensates interfere. This is a direct measure of the relative phase between the two condensates. In fact, an interference producing fringes can only happen if a macroscopic phase can be attributed to each condensate. In that case it is possible to obtain the expected interference pattern by modeling the condensates as two point like sources in harmonic confinement and separated by a Gaussian barrier [82]. Thus, the fringes period can be written as if two point-like pulsed source at a distance $d$ interfere, and it is given by the de Broglie wavelength $\lambda$ associated with the relative motion of atoms with mass $m$:

$$\lambda = \frac{ht}{md} \tag{2.6}$$

where $h$ is the Planck's constant, and $d/t$ the speed of the condensates in any point of the space.

Over all the theoretical work following the experimental results, two years later it was explicitly shown that the observed interference pattern is related to the existence of a macroscopic phase coherence inside the condensates [79]. The idea of the paper is to explore the behavior of the condensate in momentum rather than in coordinate space, leading a straightforward relation with experimental measurable quantities. In the paper, two parallel trapped condensates are taken into account, located at a distance

$d$ along the $x$ axis. They've associated the order parameters $\psi_a$ and $\psi_b$. The starting point is the assumption of the presence of the coherence, so that the order parameter of the whole system can be written as:

$$\psi_c = \psi_a + e^{i\phi}\psi_b \ . \tag{2.7}$$

By going into the momentum space, it is possible to derive the momentum distribution

$$\langle \hat{n}(\mathbf{p}) \rangle = 2\left[1 + \cos\left(p_x\frac{d}{\hbar} + \phi\right)\right] n_0(\mathbf{p}) \tag{2.8}$$

where $n_0(\mathbf{p})$ is the momentum distribution of each condensate.

Fringes-like interference pattern is clearly predicted with the cosine periodicity, while it results that without phase coherence the density distribution does not exhibit interference. In fact, in that case the many-body wavefunction would be separable, and the average of the momentum distribution operator would take the value $n(\mathbf{p}) = 2n_0(\mathbf{p})$, which clearly does not exhibit interference.

### 2.4.2 The problem of interference in fermionic systems

Everything is thus very clear and linear for what concerns Bose-Einstein condensates, but when dealing with fermionic superfluids things get more complicated. This is mainly due to the fact that different fermionic regimes are experimentally accessible, and it seems that the interaction strength plays indeed a significant role in the visibility of the interference pattern.

Interference among fermionic systems has firstly been achieved in 2011 by overlapping two parallel mBECs [89]. As expected, in the weak interacting regime the fringes are well visible but, increasing the interactions, the visibility decreases.

In fig. 2.14, the contrast of interference is plotted against the interaction parameter in unity of magnetic fields. The results can be summed up as follows: since the interference pattern shows coherence over the spatial extension of the cloud, the contrast of interference vanishes above the critical temperature of condensation, demonstrating that the interference is established by condensed molecules only. On the other side, it is found out that non-forward elastic scattering processes can lead to a depletion of the condensate wave function while the clouds overlap. Since this effect increases with the interaction strength, it prevents from observing interference in the strongly interacting regime. Therefore at unitarity what is seen is not an overlapping but instead a collision and a deformation which can be explained as an hydrodynamic behavior.

Then, some theoretic paper have confirmed the conjecture that the strong interaction profoundly affect fringe formations during the expansion and overlapping of two superfluid Fermi gases [88]. Therefore from both theoretical and experimental prospects, interference between superfluid Fermi gases in the strongly interacting regime is so far unknown.

Still, a method has been suggested to suppress the non-forward collision and try to access the unitary or even the BCS regime, and it is employing fast magnetic field

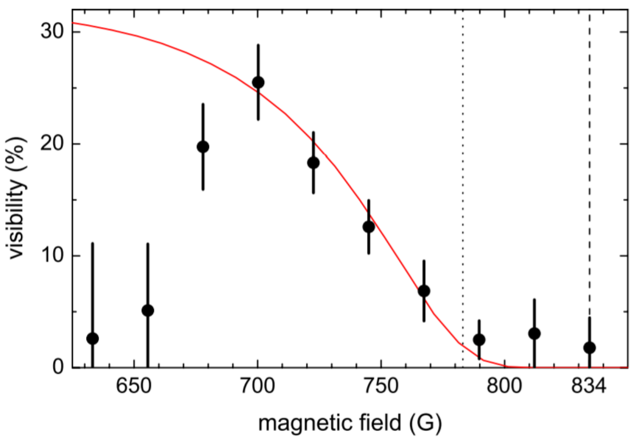


Figure 2.14: Visibility of fringes against interaction strength. Black point and bars represent data and standard deviations from 20 realizations, while the solid line is the predicted visibility from the simple calculation modeling the non-forward scattering events. Adapted from [89]

ramping techniques [41, 91]. In this work we have actually used magnetic field ramp techniques both fast and slow with different purposes: we are able to study persistent currents across the BEC-BCS crossover and detect them by interference methods. In fact, after having excited the current, a sweep of the field is performed. Since strong interactions prevent the formation of fringes, we sweep the field from the region of work (which can be 834 G for unitarity or even 862 G for BCS) to a deep BEC regime (at field of 702 G, so $1/k_F a \simeq 5.5$).

We usually perform one of two kinds of sweep: since we are interested in the detection of a residual current, in order to study persistent currents, a 50 ms sweep is performed, and after 10 ms of waiting time (for the stabilization of the field) an absorption image is taken. Otherwise it is also possible to perform a fast "jump" to BEC regime, which is 2/3 ms long and allows to monitor the millisecond dynamics of the atoms. This method will be mainly employed in ch. 4.

# Chapter 3

# Measurements of persistent currents and decay in fermionic superfluids

In this chapter, we are going to present and discuss the main results achieved in this thesis work: we provide the observation of currents whose lifetime is limited only by experimental resolution of imaging with a low number of atoms. More in detail, the currents we observe are detected up to a few seconds and a decay is never observed for all the regimes across the BEC-BCS crossover. The way in which we observe currents consists in counting the number of spirals that appear in the interference pattern.
We will also provide the results of the phase imprinting technique as a reliable method to excite desired quantized circulations. After having proved that the currents are long-lived, we will discuss on the methods to damp them and make the circulation decay, presenting a Landau-like excitation above critical velocity, and the effect of a disordered potential on the currents.

## 3.1 Detection of spirals

As we have already discussed, we employ interference methods to detect the existence of a current. This technique is available only when dealing with condensates, since requires a macroscopic phase coherence, as widely discussed in chapter 2.4. We are going now to follow the way indicated in ref [79], and apply the method to our geometry to find out what is the expected interference pattern in presence or absence of currents.

The model we take into account to simulate our geometry is shown in fig. 3.1. We consider two condensates such as those we have in the experiment, so a disc and a concentric ring. The first step is now transfer in polar coordinates the procedure: we assume for simplicity that the condensates contain the same avarage number of atoms, and describe the inner condensate as $\psi_a$ and the outer with $\psi_b$, where thus $N_a = N_b = N/2$.

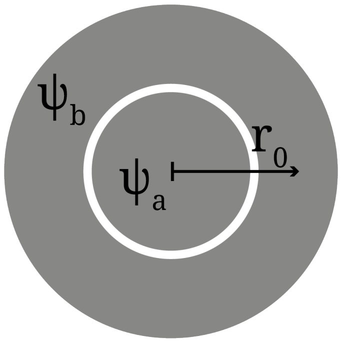


Figure 3.1: Model of the geometry employed in the calculation. We consider to condensates at radii zero and $r_0$, each one described by a macroscopic wave function $\psi_a$ and $\psi_b$ respectively.

It is possible to write the order parameter of the whole system as a linear combination of two:

$$\psi_c = \psi_a + e^{i\phi}\psi_b \ . \tag{3.1}$$

Please note that the relative phase, without any imprinted potential, is just a constant difference. We follow ref [79] in the definition of the order parameter $\psi_0$ of a single condensate obeying Gross-Pitaevskii equations and normalized to $\int d\mathbf{r}|\psi_0|^2 = N/2$, so that in the momentum space the order parameter takes the form

$$\tilde{\psi}(\mathbf{p}) = \tilde{\psi}_0(\mathbf{p}) + e^{i(\phi - \frac{k}{\hbar}r_0)}\tilde{\psi}_0(\mathbf{p}) \tag{3.2}$$

from which follows the density distribution in the momentum space

$$n(p_r) = \langle \hat{n}(p_r) \rangle = 2\left[1 + \cos\left(\frac{p_r r}{\hbar} + \phi\right)\right] n_0(p_r) \tag{3.3}$$

where $n_0(p_r) = |\psi_0(p_r)|^2$ is the momentum distribution of each condensate. We report in fig. 3.2 the resulting profile density. Since in the atomic sample, the time-of-flight (TOF) expansion gives the information about the momentum space [33], the obtained profile should be the one that the atoms reproduce.

What is thus expected is the Mexican-hat-like 3D pattern in fig. 3.2a, which would then results in concentric circles pattern in fig. 3.2b viewed by vertically integrating. So, periodic circular fringes are expected in case of interference of non-moving condensates in our disc plus ring geometry.

What is instead not trivial and indeed interesting is to explain what happens in presence of a circulation. As discussed in chapter 2.3, our method to make the atom rotate consists in imprinting a phase on the external ring. The phase we choose to use in the model is a function which is linear with the angular coordinate, since it is the ideal phase profile that we imprint in order to gives rise to an uniform velocity in the angular direction as explained in ch. 1.3.2. Always referring to figure 3.1 we can write

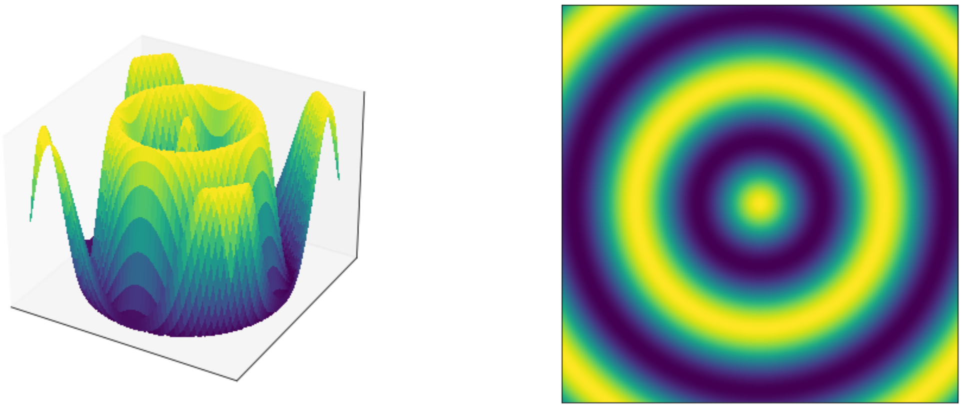

(a) (b)

Figure 3.2: Resulting profile of the interference pattern between two non-moving condensates in a 3D picture (a) and viewed from above (b). Concentric fringes appear as a sign of macroscopic phase coherence with a constant phase difference between the two condensates.

the order parameter of the whole condensate as

$$\psi_c(r,\vartheta) = \psi_a(r) + e^{i(\phi+\varphi(\vartheta))}\psi_b(r) = \psi_a(r) + e^{i(\phi+W\cdot\vartheta)}\psi_b(r) \tag{3.4}$$

where in the last step we've inserted the linear phase profile which we imprint on the atoms $\varphi(\vartheta)$ that is linear with $\vartheta$.

To access the momentum phase we perform Fourier transform. Since the interference takes place during the clouds expansion only in radial direction, we will transform only in that coordinate. We obtain:

$$\begin{aligned}\tilde{\psi}_c(p_r,\vartheta) &= \int \frac{dr}{(2\pi\hbar)^{3/2}}\psi_0(r)e^{-\frac{i}{\hbar}p_r r} + e^{i\phi}\int \frac{dr}{(2\pi\hbar)^{3/2}}\psi_0(r)e^{-\frac{i}{\hbar}p_r(r+r_0)}e^{im\vartheta} = \\ &= \tilde{\psi}_0(p_r) + e^{i\left(\phi+W\cdot\vartheta-\frac{p_r}{\hbar}r\right)}\tilde{\psi}_0(p_r)\end{aligned} \tag{3.5}$$

from which it is possible to derive the average value of the momentum distribution operator by computing $\hat{n}(p_r) \equiv \hat{n}_c(p_r) = \hat{\psi}^\dagger(p_r)\hat{\psi}(p_r)$ obtaining:

$$\begin{aligned}n(p_r,\vartheta) &= \langle\hat{n}(p_r)\rangle = |\psi_0(p_r)|^2\left[1 + e^{i\left(\phi+W\cdot\vartheta-\frac{p_r}{\hbar}r\right)} + e^{-i\left(\phi+W\cdot\vartheta-\frac{p_r}{\hbar}r\right)} + 1\right] = \\ &= 2|\psi_0(p_r)|^2\left[1+\cos\left(-\frac{p_r}{\hbar}r+\phi+W\cdot\vartheta\right)\right] .\end{aligned} \tag{3.6}$$

It is now worth to compare the obtained result in eq. 3.6 with the previous one in eq. 3.3: in presence of phase difference between the two condensates that varies in the space, also in the final profile a new contribution arises. Namely, the imprinted phase acts in the argument of the cosine function by changing its periodicity. The result in equation 3.6 defines indeed an interference pattern which, seen from above, is made of spirals. It particular, what defines the number of counted spirals is the winding number $W$. We obtain therefore concentric circles (no spirals) when no phase is imprinted, 1 spiral when $2\pi$ phase gradient is imprinted, 2 spirals for $4\pi$ and so on.

We remark that we can also produce circulation with same magnitude and opposite sign by imprinting a phase gradient in the opposite direction. As a result from eq. 3.6, we address $W > 0$ to clockwise spirals (see fig. 3.3) and $W < 0$ to anticlockwise ones; the result is a spiral (or more than one whit respect to the imprinted phase) in the opposite direction. The results obtained in eq. 3.6, are presented for different values of the winding number $W$ in the upper panels of fig. 3.3: as explained, it is possible to detect the imprinted winding number by counting the number of spirals. In correspondence of each simulated image is reported below also the experimentally achieved interference pattern. The spirals presented in figure 3.3 are relative to the unitary regime. Then, in order to perform the measurement of the interference, before switching off the confinement traps, a sweep of the magnetic field to the BEC side is performed.

We report in fig. 3.4(a) the comparison between spirals in the three different regimes for low imprinted circulations. In figure 3.4(b) we show the procedure we employ to detect the current in the non-BEC regime of fermionic superfluidity: since, as explained in ch. 2.4.2, interactions prevent the possibility to see clearly interference pattern in the unitary and BCS regimes, we perform a sweep to the BEC side of the resonance. More in detail, we follow the procedure in figure: first we imprint a phase gradient for a time $\tau$ short enough to satisfy requirements explained in ch. 2.3. Then a time $T$ for evolution is given to the system; during this time some manipulation can be performed, as we will see in the next chapters. Before taking the image, the magnetic field is ramped to 702 G, which is the value for a BEC superfluid at $1/k_F a \simeq -5.4$. At the end of this sweep, we hold 10 ms that the magnetic field stabilizes, and then we switch off the optical traps and take a time-of-flight (TOF) image. The TOF duration determines the pattern periodicity and the thickness of the fringes, but not the quantitative result i.e. if there is - or there is not - a circulation. Usually 1.2 ms of TOF are used to obtain spirals in this work.

Once obtained the interference pattern, the first available information is contained in the number of spirals showing up. As said, the number of spirals is related to the winding number, therefore it stands for a direct quantitative measurement of the current which is circulating in the ring. The most trivial way to obtain $W$ is counting by eye the number of spirals. Anyway, some more quantitative methods are now presented.

The first method consist in performing a fit of the image, after a bit of processing, with the function in eq. 3.6. The main problem concerns the possibility to perform a fit in which one of the parameters to be optimized has to be kept discrete. Standard optimization algorithms do not allow this possibility due to the employed optimization methods. It is anyway possible to perform a fit keeping $W$ as a real number, and then approximated it to the nearest signed integer. It is worth to point out that the function in eq. 3.6 is not continue for non-integer values of $W$; therefore it is not possible to keep

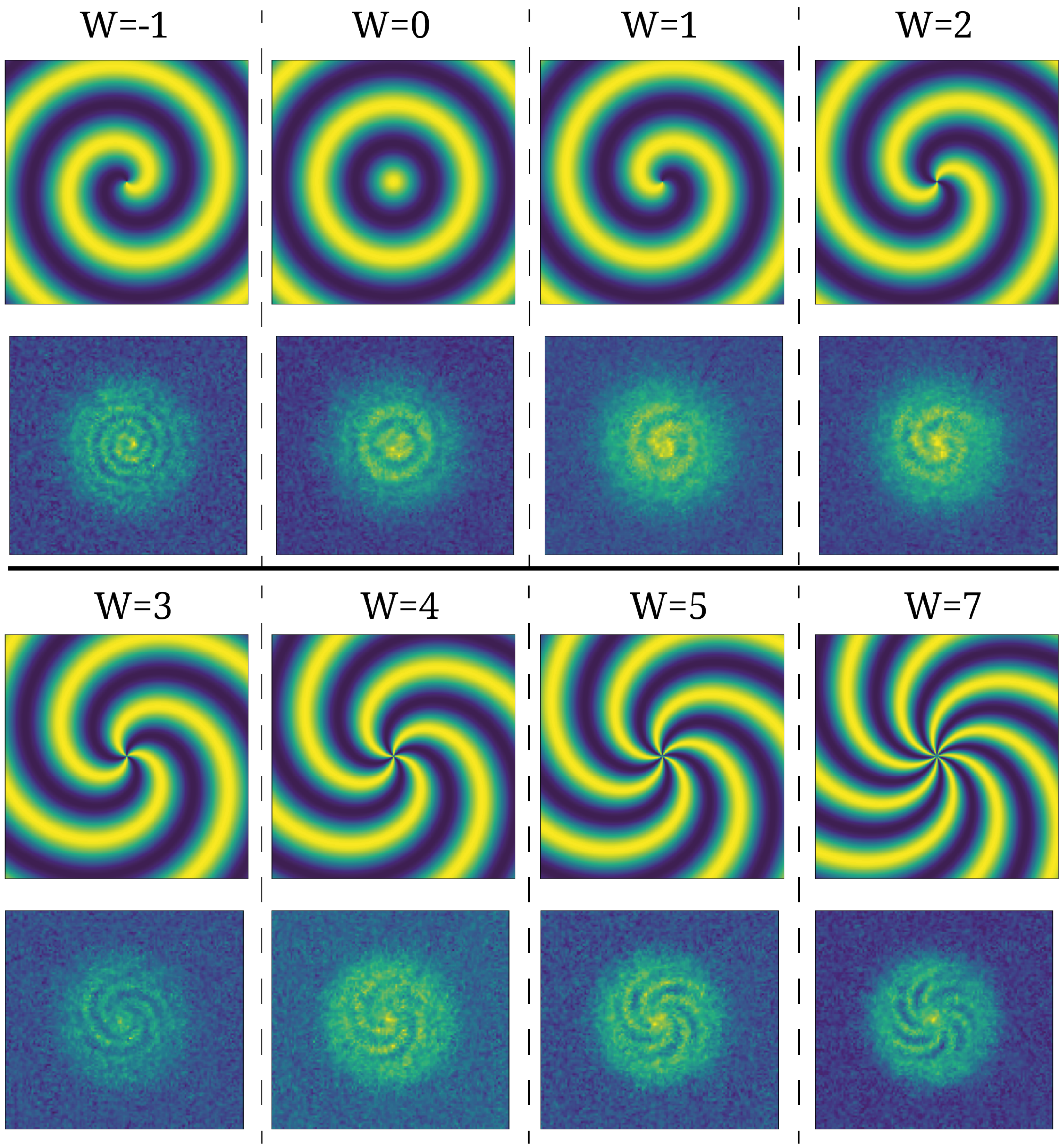


Figure 3.3: Simulated and real spirals in unitary Fermi gas (UFG). In the upper panels what is shown are the results of expected interference pattern between annular condensate and reference disc: the different number of spirals is related to the winding number i.e. to the phase difference imprinted on the atoms. In the lower panels we report the obtained spirals corresponding to the expected upper ones. The spirals reported in this figure are relative to UFG dynamics, and then a sweep to the BEC is performed to obtain the interference pattern. Each image is the result on the average of more (from 4 to 6) images.

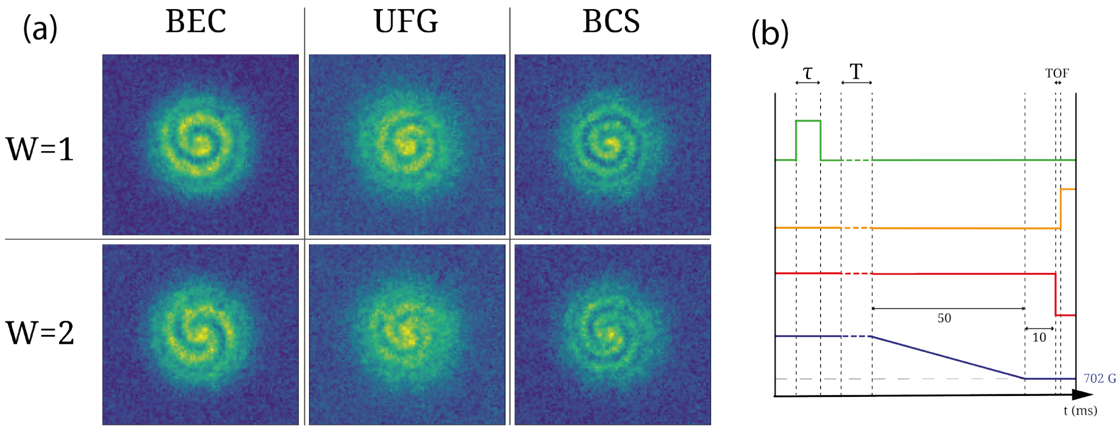


Figure 3.4: (a) Gallery of spirals across the three fermionic superfluid regimes for low imprinted circulations. Each image is averaged over four different realizations. (b) A scheme of the procedure to detect currents in different fermionic superfluids: we imprint (green) the circulation for a time $\tau$, then the evolution and eventually other manipulations are performed; when we want to perform the measurement we sweep the magnetic field (blue) to the BEC side in a 50 ms ramp and, after 10 ms of stabilization of the field, we switch off the trapping (red) and take an image (orange) in time-of-flight (TOF).

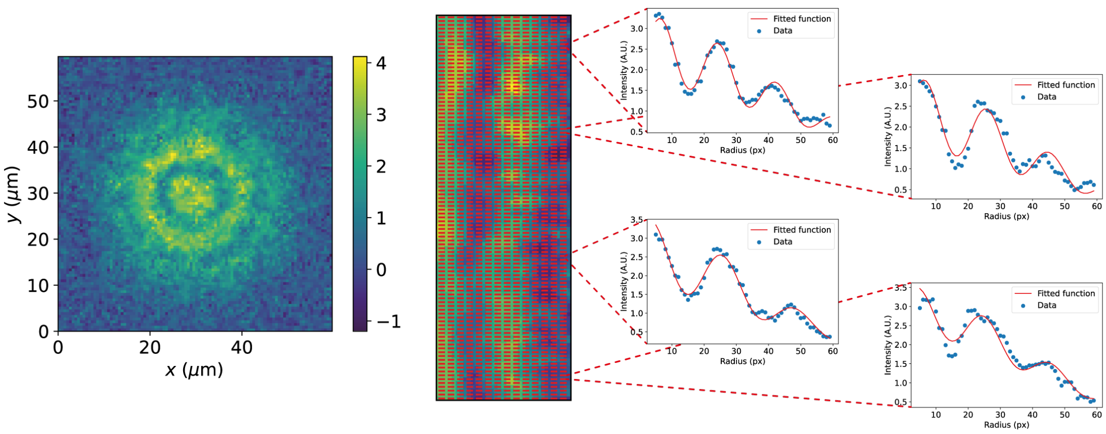


Figure 3.5: Graphical explanation of the devised technique to count spirals. On the left panel the starter point is shown: as an example we used a BEC interference pattern. After a blur, the image is unwrapped from its center, the first noisy columns of pixels are removed, and horizontal cuts are performed (central panel). Each horizontal strip is then fitted with a cosine convoluted with a Gaussian function to extract the phase shift.

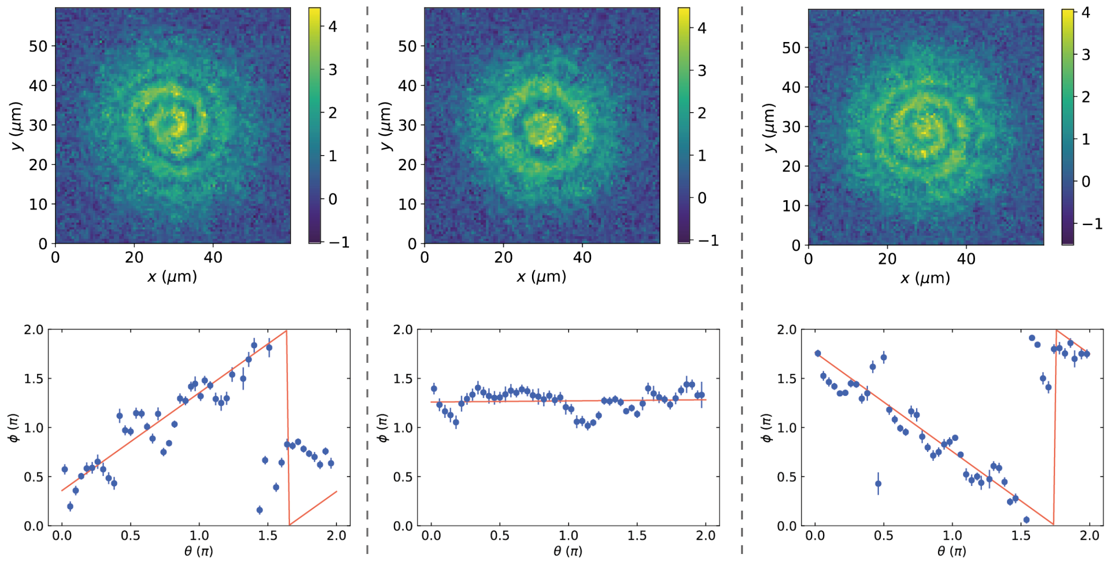


Figure 3.6: Results of the methods to quantitatively count the spirals. Three example of BEC interference pattern are shown with anticlockwise spiral, no spiral, and one spiral respectively in left, central, and right panels. Under each image it is reported the result of the analysis of the relative image: slope from linear fits is consistent with values of 1, 0, and -1 respectively.

the real value of $W$ since it would end up with a discontinuity in the density distribution profile.

Another method we come up with, is described in the following and explained graphically in fig. 3.5: once obtained the interference pattern (left panel of fig 3.5), we first perform a Gaussian blur, and then we unwrap it as described in the methods chapter 2.2. Once unwrapped, the first columns of pixel in the image are removed (since we noticed they're the most affected by noise) and then we perform a lot of horizontal cuts. For each row cut, we vertically average the pixels and then perform a fit in the horizontal direction. We fit the profile with a cosine function convoluted with a Gaussian, in order to mimic the damping due to the lack of atoms when going far from the center. In particular we fit it with the function:

$$f(x) = N\cos(kx + \varphi)e^{-x^2/\sigma} \ . \tag{3.7}$$

The parameter we are interested in, is the phase shift $\varphi$: from each row, a value of $\varphi$ is extracted and then they are collected together modulo $2\pi$.

In figure 3.6 some examples of the obtained results are reported: when no circulation is detected we've already discussed that concentric circles appear. When dealing with circumferences, no phase shift takes place since the radius is - by definition - constant. Thus, what is observed (central panel of fig. 3.6) is that the measured phase is always constant, and the slope of the fitted straight line is compatible with zero; for ex-

ample in the data reported in figure, the obtained coefficient is $m = 0.011 \pm 0.02$. On the other side, when detecting a circulation (thus a current), we said a spiral appears. What differentiates a spiral from a circumference is that in the first case the radius is not constant but varies with the angle, so that the line never closes on itself. As a consequence, a phase shift arises. Moreover, since the spiral line never closes on itself, a phase jump has to take place. In the right panel of fig. 3.6 we observed exactly this phenomenon. We have performed also a linear fit (modulo $2\pi$) and obtained the following results: for the right panel (clockwise spiral) the slope value is $m = -1.007 \pm 0.093$, while for the left panel (anti-clockwise spiral) we obtained $m = 0.995 \pm 0.093$. The results are indeed in extremely good agreement with values +1 and -1, which means that it is possible to detect also the direction of the current.
The same procedure can be applied to images with more spirals, where the line profile winds up more than once. In that case we observe - as expected - more severe slopes, since $W > 1$ phase jumps have to take place in the same space of $2\pi$. Because of this reason, images with high winding numbers ($W > 5$) are not very suitable for this analysis, since an extremely high resolution would be needed to identify different very close lines. In that cases, an human-eye based approach has still revealed to be the most efficient one.

## 3.2 Phase gradient calibration: the results of phase imprinting technique

As we have seen, we are able to obtain currents with high winding numbers and detect them from the interference pattern they exhibit, by counting the number of spiral across the different fermionic regimes of superfluidity. In this section, we want to provide a characterization of the phase imprinting technique we employ to obtain circulations of the ring, in order to show how we can excite the wanted winding numbers in a deterministic way.

The method of phase imprinting has been widely discussed in ch. 2.3: what most matters is that we are able to imprint on the atoms the desired phase profile. Since a superfluid velocity arises from the gradient of the macroscopic phase, by imprinting a phase which depends linearly on the angular coordinate it is possible to excite rotational motion. There are some tunable parameters, among which the most important are the intensity of the imprinted phase gradient and the imprinting time $\tau$. The importance of being capable of changing intensity of the optical potential relies on the fact that the regimes across the BEC-BCS crossover have different values of the chemical potential; thus, in order to explore all of them, it is necessary to be able to tune the intensity of the phase profile imprinted (beyond the trapping obviously).

On the other side, by changing the imprinting time it is possible to decide the number of circulations we want to imprint. We've already seen in sect. 2.3 that the winding number results depending on $\tau$, therefore a longer pulse duration will result in higher imprinted circulations. We report in fig. 3.7 the result for a calibration performed at

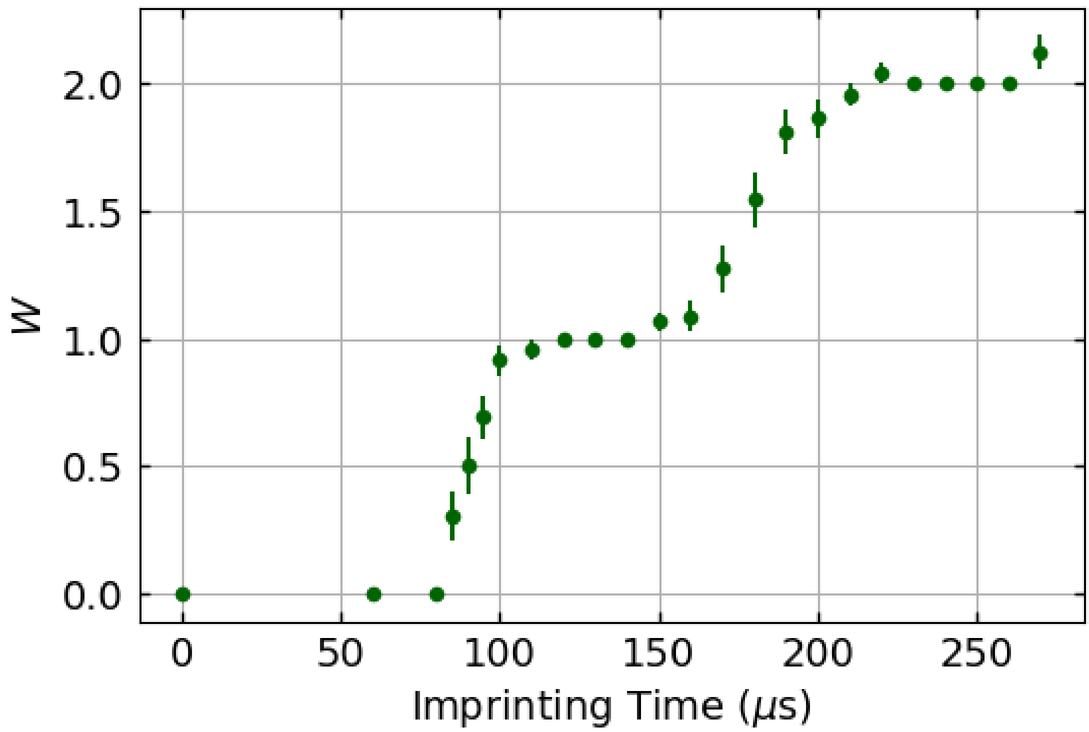


Figure 3.7: Resulting winding numbers for different values of imprinting time in the BEC regime. It is possible to tune the number of spirals obtainable by changing the pulse duration of the phase gradient, and so access to different quantized circulating states. Each point is the average over more than 20 realization, and the error bars are the standard deviation of the mean; points without error bars correspond to 100% of realization with the same output.

low winding numbers. At first sight, we remark the incredible similarity with fig. 1.7 regarding quantization of the magnetic flux in superconductors, highlighting again the strong analogies between these systems. Indeed, as shown in fig. 3.7, the quantized quantity here is the circulation, in units of $h/m$. What we show in the figure is the winding number, obtained by counting the spirals as explained in sect. 3.1. Each point of the figure is obtained by averaging at least 20 realizations of the experiment in the BEC regime with the same parameters. Finished one point, we change the imprinting time and repeat the same procedure. The error bars in the figure are obtained as the standard deviation of the mean over the different realizations. It is worth to point out that there are some points, at stable circulating states, where no error bars are present: it means that we obtained the same result over all the realizations of the experiment.

The results show the possibility to excite desired circulation states in a deterministic way. Just as a proof of principle, we report the results obtained in the unitary regime for the excitation of the state with $W = 1$: we've taken hundreds of images and found out that the imprinted circulating $W = 1$ state is reliable at least at 99.47%.

The plateaus in the figure correspond to stable quantized states, namely when the imprinting time has a duration which is exactly equivalent to imprint a gradient of phase that is a multiple of $2\pi$. Interestingly, we observe a slightly difference switching from BEC to UFG or BCS regimes of fermionic superfluidity. As said, we are able to perform measurements in the different kinds of superfluids by changing the interaction strength. The results shown in fig. 3.7 refer to a 702 G BEC, so the interaction parameter $1/k_F a \simeq 5.4$. We performed the same measurements also in the unitary regime and in the BCS, with the results reported in fig. 3.8. In order to compare the results we have scaled the x-axis: each regime has different chemical potential $\mu$, so different trapping powers and imprinted intensity. It is indeed possible to use eq. 2.5 to obtain the phase gradient imprinted on the atoms.

Comparing the three regimes, one would maybe expect a superposition of the calibrations, as if it is possible to lead back the phenomenon to a more universal characteristic of the system. Actually, what is observed is a rigid shift in the phase between BEC regime and the other two. Due to the importance of the unitary regime and the relative facility (compared to the BCS regime) in the realization, we focused our attention in investigate the differences between BEC and UFG results. As a matter of fact, if a $-0.26\pi$ phase shift is applied to the UFG curve, the results in the two regimes would perfectly overlap.

Therefore, we proceed to analyze possible reason to explain the observed discrepancy. The first check we performed concerns the duration of the imprinting time. It's been largely discussed about the necessity to avoid to set big imprinting time $\tau$ values to not exceed the regime of validity of the phase imprinting. In that case, also the density would be affected and the effect of the imprinting would be more complex to be investigated; in fact, we would have that both the phase and the amplitude of the order parameter are influenced and their effects cannot be decoupled. In order to verify this hypothesis, some experiments have been carried on both from the BEC and the UFG side. First, we try to lower the intensity of the gradient as much as possible with a BEC

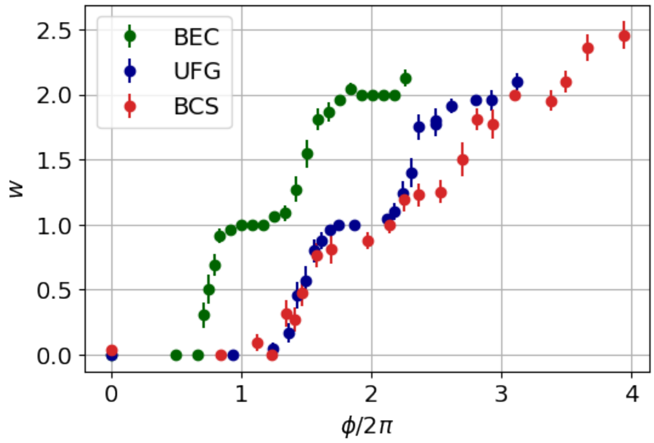


Figure 3.8: Results of phase imprinting in the three regimes across the BEC-BCS crossover. Scaling the imprinting time with the formula in eq. 2.5, it is possible to use the imprinted phase gradient as x-axis, and thus compare the BEC (green) results with the unitary (blue) and BCS (red) ones. The $0.26\pi$ shift of the last two calibrations is not expected and we propose to address it to the role of interactions.

superfluid: we thus entered in a regime where the timescale are larger than those of the unitary gas. We also repeat the measurement at different holding time $T$. More in detail, we present in fig. 3.9a the obtained calibration for $T = 2$ ms and $T = 90$ ms with longer pulses compared to the already presented BEC calibration (used as a reference).

By analyzing experimental data reported in figure 3.9a, some considerations can be done. First of all we note that there is a small shift between the trends, which mainly concerns the point in which the fluid starts to rotate. The shift is small, so it is not very compatible with the big difference detected with the UFG. We note moreover that it seems easier to detect currents when looking right after the imprinting compared to what happens after 90 ms. We will prove in the next section that these currents are long-living, so this is surely not an effort of current decay. Instead, this is due to excitations generated with the anti-gradient that we unwillingly apply on the atoms where the phase jump takes place. In fact, by looking at fig. 2.12b, it is possible to observe that, due to the finite resolution achievable in experimental setups, together with the gradient we imprint also an anti-gradient in a very localized region of the ring. A more detailed description of these excitations can be found in Appendix B; anyway, it is observed to decay at most in 20 ms (it differs for BEC, BCS, or UFG).

The second kind of measurements we performed to study more in detail this hypothesis, takes place in the unitary regime. Here, we repeat the experiment using different values of intensity for the gradient. By changing it, what differs is the imprinting time needed to achieve the desired circulation. For example, taking $W = 1$ state as a reference, we can call $\tau_1$ the imprinting time needed to imprint one circulation. We find out that for 100 $\mu s \leq \tau_1 \leq 250\mu s$ the results are compatible, while a dataset with $\tau_1 = 700$ $\mu$s

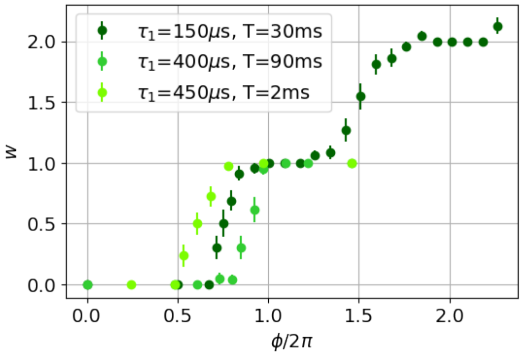


(a) Here, the calibrations obtained with the lowest possible gradient (light green ones) in BEC at different holding time $T$, are compared to the normal one (darker green) at $T = 30$ ms. A small shift is observed, but not compatible with the discrepancy from the UFG regime.

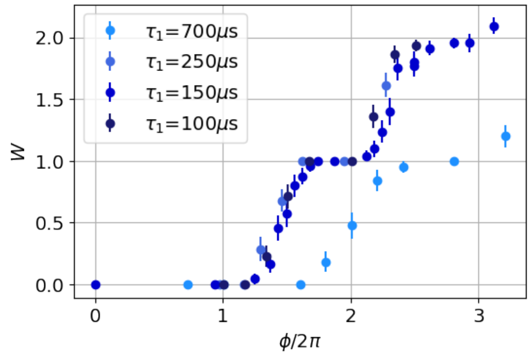


(b) Calibration of the phase gradient for different values of intensity imprinted in a unitary superfluid (UFG). The $\tau_1$=700 $\mu s$ is affected by the limits of validity of the phase imprinting approximation. Values of $\tau_1$ lower than 250 $\mu s$ are instead acceptable.

Figure 3.9: Calibration of the phase gradient with low intensity imprinting in BEC (a) and UFG (b) regimes. With $\tau_1$ it is identified the pulse duration needed to generate $W = 1$ state; we conclude that the discrepancy in the results presented in fig. 3.8 is not due to an excessively long imprinting time.

resulted in a significant shift, as clearly visible in figure 3.9b. We address this shift to the fact that we exceeded the limit of confidence for the phase imprinting approximation. On the other side, it means that in the range between 100 $\mu s \leq \tau_1 \leq 250$ $\mu s$ everything should work fine. Since we usually put ourselves in the conditions for which $\tau_1 = 150$ $\mu$s, we can exclude that the discrepancy is due to a too long imprinting time, so the reason has to be searched somewhere else.

Another possibility we conjectured is that the different nature of the superfluids can play a significant role. To this purpose, we performed some measurements to better understand the role of interactions. Since it is possible to change the scattering length by means of Feshbach resonance (see Appendix A), not only usual 702 G BEC is accessible, but also other regimes in which the interaction parameter $1/k_F a$ is lower. More in detail, we report in fig. 3.10 the measurements performed in the following regimes: BEC at 702 G of magnetic field (usual), BEC at 744 G, BEC at 782 G, and finally the unitary regime in which the magnetic field value is 834 G. As visible in the figure, we noticed that the three BEC regimes do not show the same behavior. Instead, a shift appears and it depends on the applied magnetic field. What is observed is that increasing the interactions in the system, the phase difference needed to excite the state with one circulation increases as well. Better, since the by definition a $W = 1$ state is generated by a $2\pi$ phase difference, what is most likely is that some of the phase we imprint is lost due to an interaction-dependent mechanism which is needed to be further investigated.

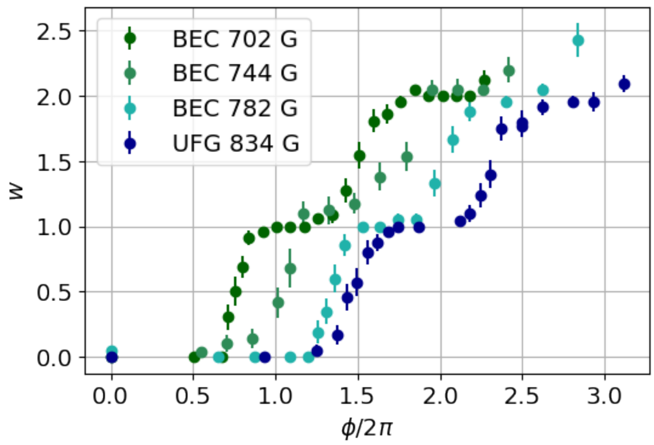


Figure 3.10: Calibration of the phase gradient for low winding numbers in different superfluid regimes. By changing the magnetic field, we explore gases with low to strong interactions and we detect a phase shift. We can thus address the phase difference between UFG and 702 G BEC to the role of interactions in the system.

As a conclusion of this section, we sum up the most relevant conclusions. We characterized the phase imprinting technique which has thus been used for the first time in order to excite currents. We also demonstrated the possibility to generate states with the desired winding number in a very deterministic way, for all the different regimes across the BEC-BCS crossover. We also detected a discrepancy between the BEC regime and the other two that we addressed to the role of interactions in the fermionic superfluids.
It is now possible to study the currents themselves, regardless the way in which they were generated, to investigate their persistence and eventually the decay-mechanisms.

## 3.3 Persistence of the currents

In this section, we are going to provide proof of the persistence of the current. We will demonstrate that they are persistent by proving that no decay is observed for all the time in which the system is detectable. In metallic superconducting systems that currents can sustain flow almost forever, in the sense that no decay is observed for all the lifetime of the system. In the same way our system has strong analogies with that solid state superconductors: in theory, the lifetime of the supercurrents we observe should be limited by the time in which the system remains superfluid. Interestingly, we observe that the supercurrents are limited only by the resolution of our imaging detection, since the atom number decay results faster than the decay of the superfluid fraction.

Actually, in usual superconductors, the lifetime of the system is often willingly tuned without many restrictions. Instead, when dealing with ultracold gases, this is

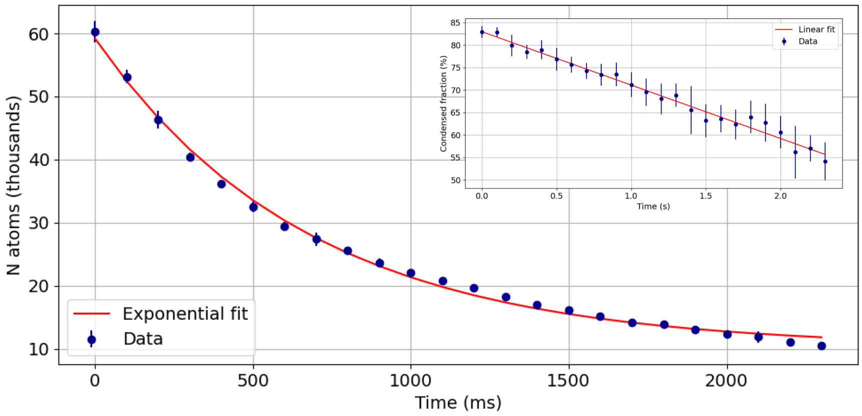


Figure 3.11: Lifetime of the atoms in the superfluid BEC regime. To monitor the lifetime of the system, the sample is loaded in the harmonic cigar trap, and the number of atoms is measured at different times; each point is the mean over 10 realizations. By fitting the points with an exponential function (in red), it is possible to extract the decay rate of $\tau = 674 \pm 24$ ms; thus, our imaging system allows us to measure currents up to $\sim$1.5 seconds. In the inset, the simultaneously measured condensed fraction is shown: at 1.5 seconds the condensed fraction is 65%, thus it is not the most limiting timescale.

not quite true. Because of the confinement system, and due to the inter-particle scattering events, the system is not stable for long times in the prepared conditions. Thus, the lifetime strongly depends on the experimental apparatus and the kind of measurements that have to be performed. As an example, it is clear that after evaporative cooling it is very easy for an atom that randomly acquires a small amount of energy to escape the low confinement that is needed to keep the cloud at a very low temperature.

To have an order of magnitude of the timescales in our systems, we perform a measurement of the lifetime of a gas in the optical crossing trap. In this harmonic trap it is also possible to measure the temperature of the gas in a unitary regime (as explain in chapter 1.2.2) by fitting the density distribution from an absorption image. Or in the same way it is possible to measure the condensed fraction if the measurement is performed in the BEC regime by fitting the bimodal density distribution.

In figure 3.11, it is reported the result of a lifetime measurement of a BEC superfluid whose initial condensate fraction is about 83%. As said, to perform the measurement the gas is loaded in the crossing trap and then is cooled down to reach the degeneracy regime. This operation is performed - as usually - at 834 G (at the resonance), but right after the field is ramped to the desired value, which in this case is 702 G ($1/k_F a \simeq 5.4$). At this point the lifetime is measured by let the gas evolve for different times and measuring the number of atoms and the condensed fraction. Ten images of the gas (so ten different realizations) are taken for each time of evolution, and their averages with the standard deviations are shown in figure as blue points with error bars. To obtain a lifetime, the data are fitted with an exponential function, from which the decay time

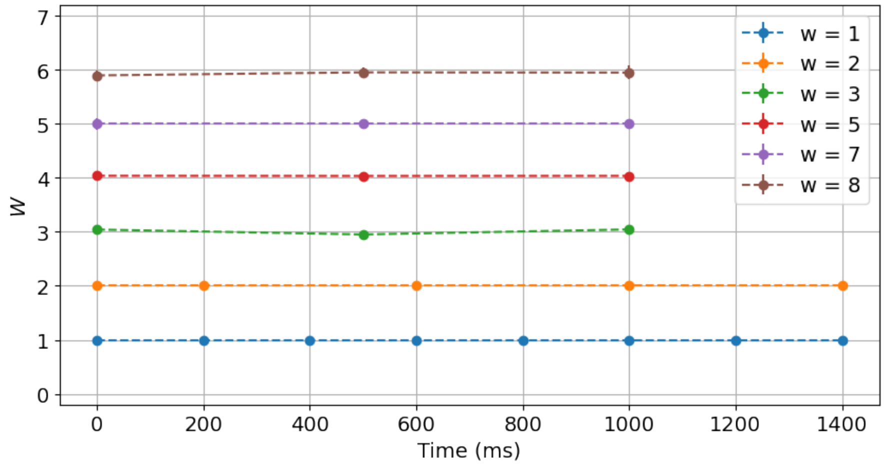


Figure 3.12: Persistent currents in unitary Fermi gas. Here the lifetimes of the currents generated in the UFG regime are shown: there is no decay and the flow is observed to be persistent more than the lifetime of the system itself. Different lines correspond to measurements at different winding numbers $W$.

$\tau$ can be extracted. The obtained result is $\tau = 674 \pm 24$ ms. We also report the results concerning the condensed fraction: as visible in the inset of figure 3.11, the decay in this case is linear (up to the 2.5 seconds at least) and its value is $\sim$65% when the atom number is at the limit of being detectable ($\sim$1.5 seconds).

Therefore, we observe that the fastest lifetime to take into account is that of the number of atoms, since no current can clearly flow without atoms. Moreover, also the imaging detection becomes more and more difficult by "loosing" atoms. As a consequence, we will consider *persistent* the currents that, from eq. 1.22, will result having a decay rate slower or comparable with the one extracted above. What we will provide is thus a lower limit for the lifetime of the currents, since no decay is observed up to when the currents are detectable, as we are going to see.

We are going now to present the obtained results. The procedure is explained in the previous sections: when the superfluid is ready, we load it into the trap made of a ring and an inner disc (as a reference); then we imprint the desired circulation. After the phase imprinting, we wait an holding time $T$ and then we take an image in time-of-flight (TOF). If operating in UFG or BCS regime, before taking the image we perform a sweep of the magnetic field to the BEC side to observe the interference pattern (see fig.3.4 for details). What we vary, to observe the persistence or decay rate of the currents, is the holding time $T$, from a few milliseconds to a few seconds. It results that for high-circulating samples, the number of atoms decay faster than in those with low winding numbers, therefore it is not always possible to explore the same time duration.

We report in fig. 3.12 the typical result obtainable (in the case in figure in the UFG regime): we excite states with different winding numbers, and check if the currents survive or not for different times. Not only we are able to check the existence of a cur-

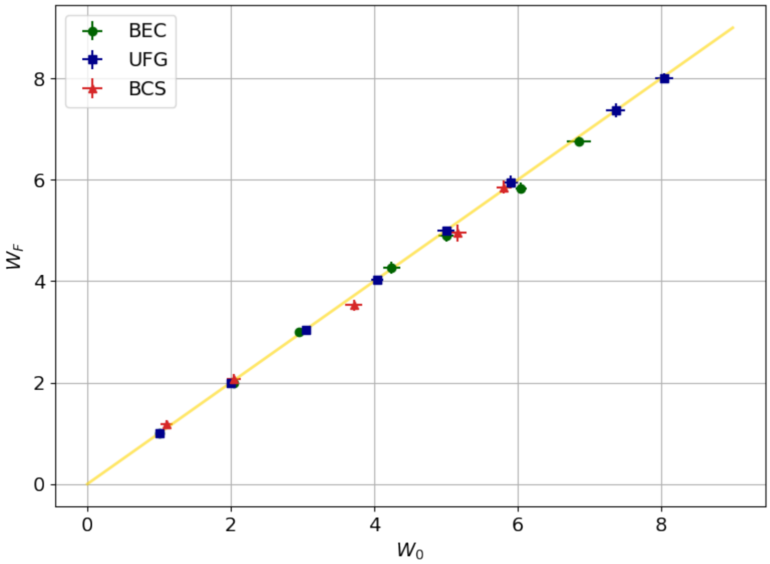


Figure 3.13: Persistent currents in the BEC-BCS crossover. The final winding number is plotted against the initial imprinted circulation to proof that no decay takes place neither in unitary, BEC, or BCS regime. This powerful result re-open the way to investigate fermionic superfluids as paradigms for other kind of superconductivity.

rent but, as widely discussed in sect. 3.1, also to determine the number of circulations present.

As a result of the experiment, as visible in the figure, no decay is observed. Instead, the states with quantized circulations last in time longer then the decay rate of the system itself. This is indeed a powerful result which demonstrates that the currents produced in these systems are really persistent. This is the very first work which detects persistent currents in fermionic superfluids with winding number higher than one, and the second time that long-living currents are observed in Fermi systems.

Up to now, just results for the unitary regime have been shown, but a lot of measurements have been performed also in the other superfluid regimes. The results are summed in fig. 3.13: since persistent flows is observed in all the three regimes, it is not possible to extract a decay rate (because the currents are indeed constant in value). Therefore the plotted results are the final winding number against the initial imprinted circulation. In particular, the final winding number corresponds to the number of spirals counted (i.e. the circulations) at the last possible time of acquisition of the measurements. Since - as said - the atom number decays faster for higher circulating states, the final winding number is extracted at different holding times.

The graph in fig. 3.13 contains thus the same information on the persistence of the currents, but allows to compare directly the three different regimes across the BEC-BCS crossover: in all the regimes persistent currents are observed in a very stable way. This is the first time that high circulating persistent flows are observed and studied in different regimes of fermionic superfluidity. These results also open the field to investigate more deeply these systems and the analogies of ultracold quantum fermionic gases with common or high-temperature superconductors. Being the firsts much more controllable systems, the mechanisms of superconductivity can be studied more in detail to comprehend also the many unknown phenomena in other kind of superconductors.

## 3.4 Critical velocity

After having verified the persistence of the currents we generate in the three regimes of the BEC-BCS crossover, the attention now is focused on the mechanisms that can possibly induce a decay of the current. We will investigate in the following of the chapter some of these phenomena. Since the decay of persistent currents due to a tunable barrier has already been widely studied (although always with bosonic condensates) [16], we investigate the role played by the presence of point-like obstacles in the system. In particular, a superfluid can be described by two main parameters, which are the chemical potential $\mu$, defining the energy scale, and the healing length $\xi$, defining the length scale. The healing length is defined by $\xi = \frac{1}{\sqrt{2}} \frac{\hbar}{m v_{\mathrm{sound}}}$, and it is the length scale in which the density and phase fluctuations in the condensate are removed by the interaction between condensed particles. It is thus interesting to study defects and spatial modification of the landscape whose dimensions are comparable with the healing length. This is not often possible in solid state superconductors, where the healing length is of the order of 1 nm, and thus the engineering of this kind of impurities often becomes unfeasible. Instead, in our systems the healing length (depending on the kind of superfluid, see tab. 3.1) is of the order of 1 $\mu$m, and thus we have the possibility to study the fundamental mechanisms od decay of the persistent currents. What is extremely powerful of the approach we employ, is the possibility to make the superfluid rotate around the obstacle for any desired time, thanks to the usage of persistent currents. Common approaches to critical velocity are usually on the idea of moving an obstacle inside the superfluid at different velocities for a certain time and then monitor the effect on the system. We are instead able to study a longer dynamics since there is no need to continuously move the obstacle considering that the current is already flowing. The narration will flow by the following path: in this section a few obstacles, far between each other, will be inserted in the ring, to access at the critical Landau velocity. Then, in the following section, the considerations on the obtained results will bring us to discuss of the role of a many obstacles disordered pattern potential applied to the atoms.

Let's proceed in the explanation of the first mentioned experiment. As said, the role of the presence of a few obstacle in the ring is investigated. To achieve this goal, the experimental sequence has to be changed a little. In fact, during the holding time the obstacles have to be ramped up adiabatically. We optimized this sequence to avoid create excitations in the system. As a result, the procedure consists of ramping the obstacles up in 26 steps with 0.5 ms of Picture Time (PT). When acquiring an image, the obstacles are switched off together with the trap. The procedure is a little more tricky when the measurements are performed in the UFG or BCS regime: since we try to

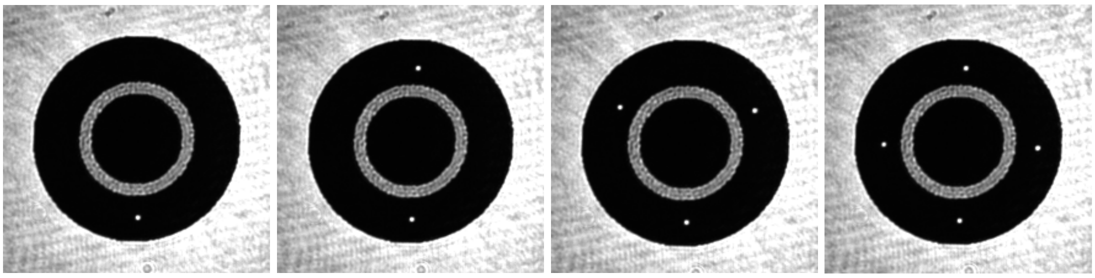

(a) (b) (c) (d)

Figure 3.14: Potential experimented by the atoms when adding a few obstacles. From left to right one (a), two (b), three (c), and four (d) obstacles are inserted in the ring. The lighter areas represent the intensity of the light imprinted on the atoms. The obstacle are uniformly distributed over the $2\pi$ angular distance to be as far as possible between each other.

work at a constant value of $\Delta/\mu$ (intensity of the obstacles over chemical potential), it is not possible to switch off the obstacles with the trap. In that case indeed, during the sweep of the magnetic field to the BEC side to see the interference pattern, the chemical potential changes its value and thus the ration $\Delta/\mu$ would not be kept constant; therefore we would not be investigating for sure the UFG (or BCS) regime but instead the sweep would affect the measurement. As a solution we ramp down the obstacles before changing the magnetic field: since it has been proven in section 3.3 that the currents are persistent in all the regimes, the 60 ms of magnetic field sweep plus wait time will not affect the existence of the current at all.

The obstacles we insert in the ring have the following characteristics: they are Gaussian shaped with the characteristic radius of 1.1 $\mu$m in the $x$ direction and of 1.4 $\mu$m in the $y$ direction. The intensity of the obstacles is abut $1.1\mu$. The disposition of the obstacles is reported in fig. 3.14: here, the images of the potential applied to the atoms during the evolution time are shown. The images are taken by redirecting the beam coming from the DMD to a camera: it is thus possible to directly access to the potential experimented by the atoms. The position of the obstacles is as far as possible, i.e. uniformly distributed over $2\pi$ angular distance. This choice is because we want to decouple the effects due to somehow interacting or ordered distributed obstacles, and just access to the effect of single disturbances in the system.

As first step, we studied the presence of a single obstacle in the ring. The main measurement performed is the lifetime of the excited currents in presence of the obstacle, for different imprinted winding numbers. We report an example in figure 3.15: for each selected initial winding number, we vary the holding time with the obstacle ON, and measure the number of visible spirals. We repeat the procedure at least 20 times, and then the evolution time is changed. At the end, we obtain a lifetime curve. What is observed, as reported in figure, is that for lower circulations no decay is observed also

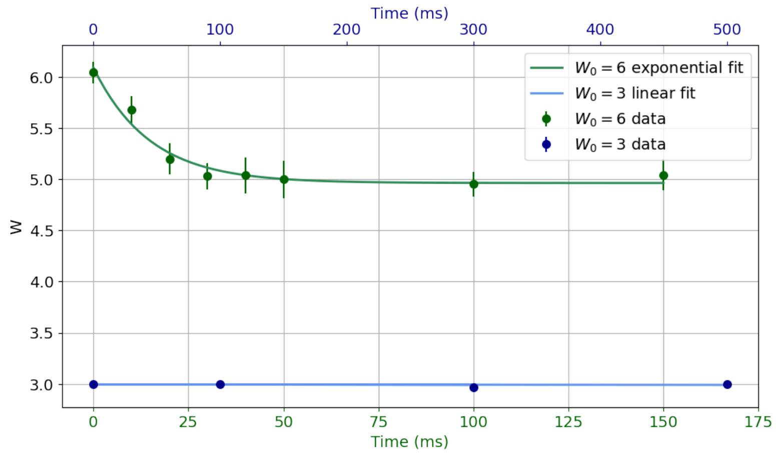


Figure 3.15: Example of lifetime measurements with one obstacle. Different timescales are used to show the long-time persistence of lower circulating states and the quick decay of currents with high winding numbers. Each point consists of the average over more than 20 realizations, and the error bars are the standard deviation of the mean. From an exponential fit (solid green line) to the $W_0 = 6$ state, it is possible to extract the decay rate and the offset i.e. final winding number.

for longer times; instead, when higher winding numbers are excited, the current is no longer stable and quickly decays into a lower circulating state.

By fitting the datasets exhibiting a decay, it is possible to derive some useful information. First of all, the decay rate can be extracted from the exponential constant of the fit. We performed measurements not only with one obstacle, but also adding more obstacles (up to 20) and we investigated how the number of disturbances affect the behavior of the system. The results of the constant of decay are reported in fig. 3.16: a faster decay is observed by increasing the number of obstacles. In figure, also the results for different winding numbers are reported: it is possible to note that in general also the number of circulations affects the decay rate, i.e. faster decay takes place when higher W is imprinted.

Another meaningful quantity that is available from the exponential fit is indeed the offset. The offset represents the final value of $W$ at which the system rests after the transitory phase. This is thus what in fig. 3.13 is called final winding number $W_F$. Since we noticed that the number of obstacles affects the decay rate but not the final value of the circulation, it is possible to use a single obstacle and investigate the post-transitory phase changing $W_0$. This measurement would indeed give as a result the critical velocity above which the current is damped, due to some kind of excitation arising in the system. Moreover, we perform the measurements in all the regimes to compare the results.

We sum up the obtained results in fig. 3.17: we plot the final winding number $W_F$ against the initial one $W_0$ for the three explored regimes in the BEC-BCS crossover.

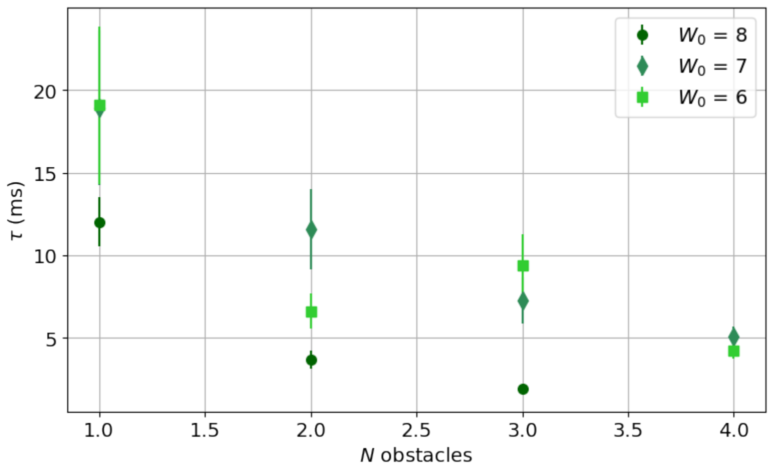


Figure 3.16: Constant of decay of the currents varying initial circulation and number of obstacles. The constant of decay is computed from an exponential fit of the lifetimes of the currents, and then plotted against the number of obstacles inserted. The groups represent measurements with different initial winding numbers $W_0$. A faster decay is observed increasing both number of obstacles and initial circulation.

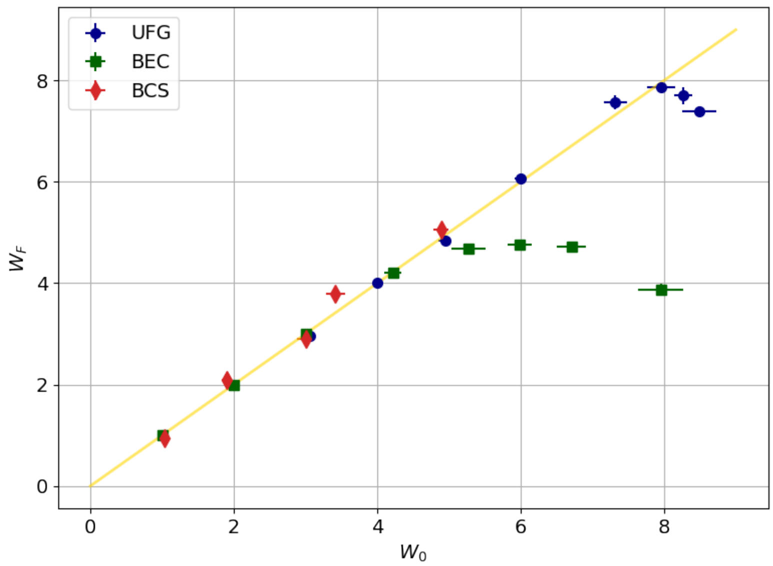


Figure 3.17: Critical velocities in the BEC-BCS crossover. The final winding number is plotted against the initial one: when the points deviates from the persistent flow prediction (solid yellow line), it means that a decay takes place and thus the superfluid flow is not stable anymore due to the presence of some kind of excitations.

Let's take a look at the BEC results; it is clear that, at a certain point around $W_0 = 5$, the data significantly deviate from the persistent flow predictions. As expected, the same behavior arises in the UFG at higher circulations, namely at $W_0 = 8$. Instead, in the BCS, it was not possible to achieve this point to the low-visibility of the spirals. It is anyway possible to assert that $W_0 = 5$ is a lower limit, while recalling the elementary excitation spectra in the different regimes, we expect the critical velocity to be lower than that of the unitary value.

Before discussing what has been obtained, we complete the presentation of the results by providing them in more comparable re-scaled quantities in tab. 3.1: we report the healing length for comparison with the obstacle size, the critical measured winding number $W_C$ and the respective real units critical velocities; we finally re-scaled them over the Fermi velocity and over the sound speed to ease the comparison with other experimental data or predictions.

| | $1/k_F a$ | $\xi$ ($\mu$m) | $W_C$ | $v_C$ (mm/s) | $v_C/v_F$ | $v_C/c_s$ |
|---|---|---|---|---|---|---|
| BEC | 5.53 | 1.11 | 5 | 2,287 | 0.115 | 0,392 |
| UFG | 0 | 0.58 | 8 | 3,660 | 0.124 | 0,329[1] |

Table 3.1: Critical measured velocities for UFG and BEC regime. We provide interaction parameter $k_F a$, re-scaled critical velocity over Fermi velocity $v_C/v_F$, and re-scaled critical velocity over sound speed $v_C/c_s$ for comparison with other experiments or theories, although no theories exist yet to describe an obstacle with size comparable to the healing length $\xi$.

Let's now try to go more deeply in the meaning of the results.
As said, a critical velocity arises as a proof of superfluid behavior and depends on the excitation spectrum of the system under investigation. This is stated from the Landau criterion for a point like object (see ch 1.2.3). Let's for a while restrict ourselves to the BEC side. A source of heating for the system is the excitation of phonons; these excitations are predicted by Landau to have a critical velocity $v_C$ equal to the speed of sound $v_S$. $v_S$ can indeed be predicted in the Bogoliubov approximation of weakly interacting gas which results a good approximation since we are working in the $1/k_F a \geq 5$ regime.

By considering thus Bogoliubov waves as first excitations, we would obtain as critical velocity $v_C^{Bog.} = c_S = 5.84$ mm/s. As reported in tab. 3.1, we instead find $v_C = 2.29$ mm/s, which correspond respectively to $c_s = 0.29 v_F$ and $v_C = 0.12 v_F$. The agreement is not good, and the reason has to be mainly researched in the nature of the lowest kind of excitations. It is indeed well known that there are lower energy excitations: a

[1]For the unitary regime, there is no theoretical prediction on the lowest excitation, but an interplay of Bogoliubov sound waves and pair breaking excitations gives the critical velocity. Since from quantum MonteCarlo simulations the pair breaking critical velocity has resulted to be $v_{pb}^{UFG} \simeq 0.39 v_F$, which is a bit higher than the speed of sound in our system $v_s^{UFG} = 0,38 v_F$, we re-scaled the value over the lower predicted energy excitation.

possible excitation with lower energy is due to the formation of a vortex when moving a macroscopic obstacle in the superfluids. In this regime the theories are indeed well consolidated: firstly, Feynman gave an estimation [92] of this phenomenon where the critical velocity results to be $v_C \approx (\hbar/mD)\ln D/\xi \ll c_S$ for superfluid flow in a long channel with diameter $D \gg \xi$. More recently works [93] derived an analytical criterion for the critical velocity of superfluid flow around macroscopic obstacles, obtaining the prediction $v_C \sim \hbar/mR$ with $R$ being the size of the object. This is pretty consistent with experiments carried on to measure $v_C$ in ultracold weakly interacting Bose gases which have been performed both in the three-dimensional [94, 95] and two-dimensional [96] regimes. The experiments are usually based on obtaining the rate of dissipation either by measuring the amount of heating via the resulting depletion of the condensate [94] or, more directly, by observing the asymmetry in density associated with a finite pressure difference across the moving object [95]. With these methods, critical velocities between 10% and 26% are observed. Yet, as said, it is expected that $v_C$ is limited by vortex excitations since the healing length is much smaller than the obstacle size.

A possible way to overcome this limitation consists in using obstacles whose size is comparable to the healing length. This is a powerful tool of our system, since the micrometer resolution of the obstacle has been reached. Previously, an heating measurement has been performed [97] with a $\sim$2 $\mu$m large obstacle in fermions. The obstacle used in that work, is a red-detuned laser beam which acts as attractive potential to the atoms, and it is a little larger than our obstacle, but still comparable with the healing length of the system. What is found in the paper is a critical velocity significantly lower than the speed of sound, and thanks to numerical simulations in the BEC side, they were able to address this fact to different phenomena, such as the circular (instead of linear) motion of the stirrer and finite temperature effects (which can induce vortex-antivortex excitations), that cause 15% of decreasing. Another 39% of decreasing is finally addressed to the inhomogeneous system in the trap. By interpolating experimental and simulated points at $1/k_F a = 3.5$ with the simulated one at $1/k_F a = 6.5$, we find an acceptable agreement with our results, considering the fact that the gas we are working with is quasi-homogeneous.

As a conclusion, we're currently investigating the decay mechanisms occurring in our system when the currents are observed decaying. In particular, it has been detected the presence of vortices which arises and that can cause phase slippage excitations. We report in fig. 3.18 the observation of some vortices that appear in presence of an obstacle and high circulations. To see them better, we also removed the inner disk and perform a time-of-flight imaging of the sole ring (fig 3.18b). The vortices are excited inside the ring by the presence of the obstacle between 0 and 10 ms of currents flowing. Once excited the vortices can "enter" inside the ring or "exit" from the outer boundaries. These decay of vortices causes - on average - a loss of the circulation and thus the observed behavior.

For what concerns the unitary regime, it is expected the highest critical velocity. The agreement with the results of ref. [97] is not good: they claim to observe a maximum value of $v_C = 0.31 v_F$ (actually not exactly at unitarity) while in our case the critical velocity observed at 834 G is $v_C = 0.12 v_F$. We are pretty confident that our result is

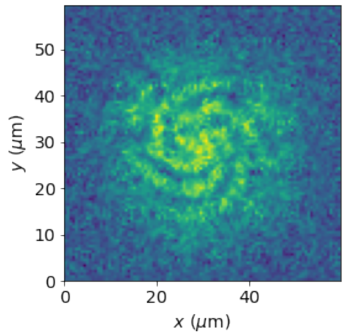


(a)

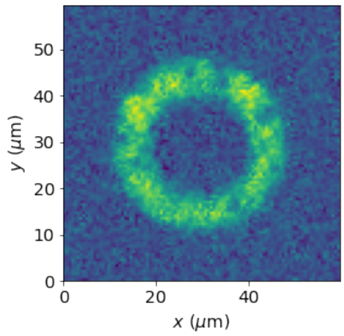


(b)

Figure 3.18: Examples of the detection of vortices which appear when an obstacle and high winding numbers are employed. The decay of the vortices inside or outside the ring, causes a decrement of the current. The vortices are less visible with the spirals (a), and thus to observe them we removed the inner disk (b).

not affected by the interplay of the boundaries of the trap, since without obstacles the current is stable. Anyway it is worth to recall that the critical velocity we measure is a consequence of the direct measurement of the superfluid phase by interference methods. Thus, the results does not represent an inconsistency, since an excitation that produces phase slip and not heat, can take place and vice-versa. Instead, our results provide a benchmark for future studies and theories investigating critical velocities due to phase slip excitations in the BEC-BCS crossover.

## 3.5 Disorder effects on persistent currents

Another aspect which we can investigate is what are the effects of a disordered matrix of impurities on the persistent currents. Disorder is indeed ubiquitous in a variety of natural phenomena, such as mechanics, wave physics, solid-state physics, quantum fluid physics or atomic physics [98]. In single particle picture of non-interacting systems, it leads to the celebrated Anderson localization, which was proposed in 1958 by the Nobel prize P. W. Anderson for the localization of electron wave function in certain random lattice potentials [99]. What is interesting to study is the effect of a disordered potentials on the persistent currents. It is expected a decrement of the currents due to disorder [100], but it is indeed not trivial to predict the scaling with the number of impurities in the system.

In this chapter, we are thus going to study the effects on the persistent currents of a potential made of a disordered pattern of obstacle. We have the possibility to change five main parameters of the disorder, in particular: the dimension, distance and intensities of the obstacles, the number of impurities, and the statistical kind of disorder. The size of the obstacles is the same as in sect. 3.4, i.e. with radius $\sim$1 $\mu$m;

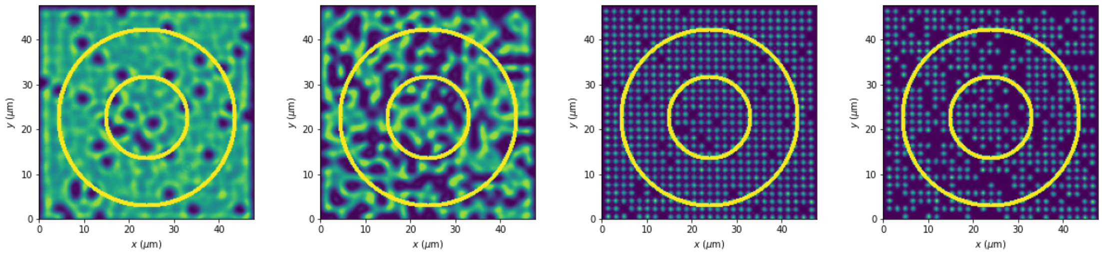


(a) Iris closed, $1 - p =$ 5%. (b) Iris closed, $1 - p =$ 30%. (c) Iris open, $1 - p =$ 5%. (d) Iris open, $1 - p =$ 30%.

Figure 3.19: Images of the potential applied to the atoms for different resolutions and probabilities of disorder. By opening (closing) an iris placed before the high resolution objective, it is possible to make more (less) light engraving the atoms and thus to achieve higher (lower) resolution of the applied potential. See the text for the definition of $p$.

the distance between impurities is instead chosen to guarantee that the obstacles are well separated, as we will discuss more in detail later. The intensity of the obstacles can also be tuned, and it will be re-scaled in units of the chemical potential $\mu$, which is the energy scale of the system; moreover, we can change the number of impurities by removing more or less obstacles from the initial ordered lattice configuration. The last degree of freedom we can tune is the resolution of the potential applied to the atoms. We report in fig. 3.19 the effective potential imprinted onthe cloud: the first two images (figs. 3.19a and 3.19d) correspond to the configuration employed up to now: potential for different disorder densities are shown. As mentioned, we can also tune the resolution as an further degree of freedom, obtaining the two images on the right (figs. 3.19c and 3.19d): this allows us to explore different kind of static-based disorder, opening the field to more comprehensive studies on a so complex phenomenon. In particular, it is possible to work with a speckle or Bernoulli kind of disorders: with low resolution the speckle disorder would cause large dimension localization and thus promotes a classical trapping mechanisms. On the other side with high resolution we can achieve Bernoulli disorder where obstacles are more defined in the micrometric scale and thus quantistic localization phenomena are encouraged.

As mentioned in ch. 2, we performed all the measurement with a closed iris before the high resolution objective. This helps in make the phase gradient and the trap walls smoother and not very sharp. As a consequence, also the obstacles result in a more shallow shape, and the overlap between each other is not negligible. From the measurement we reported, this does not constitute a problem for the current to flow, since also with all the sites occupied by obstacles the currents can be long-living. Actually, he high-resolution pattern has been tested on the atoms. We found very promising results which indeed strongly depend on the precise obstacle configuration potential applied. More in detail, we observed a strong dependence not only on the disorder type and density, but also we reported same exactly disorder densities obtained with different disorder configuration causing significantly different effects on the currents.

Now we are going to provide the results obtained by investigating the cited tunable parameters; in particular, we focused our attention on the role that is played by a disordered configuration of obstacles in presence of a persistent current. The results that will be presented, constitute just a first step in approaching this very complex phenomenon, and will provide indications and a launchpad for further more comprehensive studies. Also for this reason, the measurements are performed only the BEC regime, which is the easiest to access experimentally with the following methods and it is also a regime where numerical simulations can provide strong support.

Thanks to the results obtained in section 3.4, in order to study the effect of the disorder we can safely decide to work imprinting one circulation. The idea of the measurements is to study if the current decays due to disorder effects; sine one circulation is surely under the measured critical velocity (since up to 5 circulations the flow was persistent), and the number of obstacles does not affect it, if a decay is observed it will not be addressable to phenomena of excitations in the gas.

We are going to report mainly two kind of analysis, i.e. we investigated the effect of the intensity of the obstacles and of the quantity of the disorder in the applied potential. The meaning of the first parameter is quite intuitive: since obstacles are applied by means of optical potentials imprinted with the DMD, the intensity of the beam can be tuned to imprint more or less light on the atoms. An example of a typical measurement performed is reported in fig. 3.20b: the sequence is very similar to that of section 3.4, but instead of ramping up a single obstacle (or just a few) we ramp up a pattern full of obstacles in a way that will be described in few moments. Once defined the pattern, at least 20 images are taken for each evolution time and from the image it is determined the presence or the absence of a circulation. Then, a timestep is performed and another point is acquired. When enough evolution times are explored, it is possible to change the intensity of the obstacles and repeat the procedure to obtain another dataset of a lifetime.
In figure 3.20b the same disorder quantity has been employed, and just the intensity of the obstacles has been varied: as expected, increasing the applied power, the lifetime of the previously imprinted current decreases. Instead, when too low intensities are applied, the atoms do not feel the presence of the obstacles and continue to flow dissipationlessly. The qualitative results will be made more quantitative in a while, but before it is necessary to spend a few words describing the kind of disorder we generate.

The parameter that was called *disorder density*, is indeed more tricky to be understood. The first cornerstone to which pay attention is that we want to investigate the effects of obstacles, not those of a barrier. So, a first requirement is that the obstacle can never touch each other. To do so, we define a squared unitary cell which is bigger that the obstacle size and at the beginning each cell contains exactly one obstacle, creating thus an equally spaced lattice of obstacles. Then a probability value $p$ is set, and each obstacle is removed from its site with a probability $1 - p$. Since this operation is random, what results is a disordered potential. Two tunable parameters clearly becomes

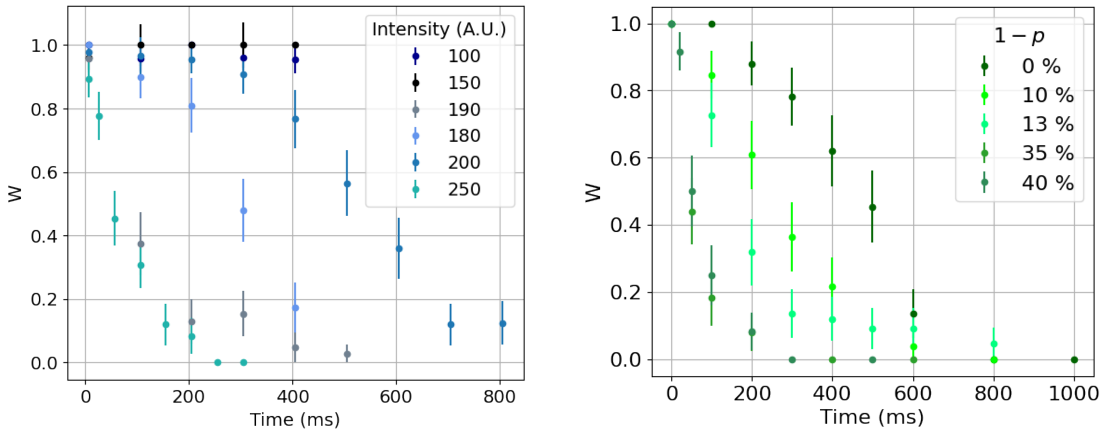


(a) Measurement of the lifetime of the current in presence of obstacles with the same disorder probability (see the text for the definition). Increasing the intensity of the obstacles, a decay appears and it becomes faster and faster.

(b) Measurement of the lifetime of the current in presence of obstacles with the same intensity. Increasing the probability of disorder (see the text for the definition) the lifetime of the current decrease.

Figure 3.20: Examples of typical measurements to extract the lifetime of the currents for different intensity of obstacles (a) and probability of disorder (b). Each point in the plot is the average of at least 20 points, and the error bars represent the standard deviation of the mean. Different kind of behavior are observed regarding whether the decay immediately takes place or instead a plateau at the initial circulation appear.

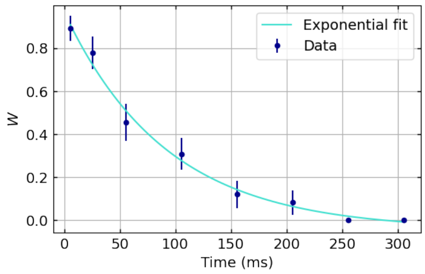


(a) Exponential fit (solid light line) over data (dark blue dots) exhibiting a fast decay rate. The half time constant of decay (see the text for the definition) in this dataset is found to be $\tau_{1/2} = 63 \pm 16$ ms.

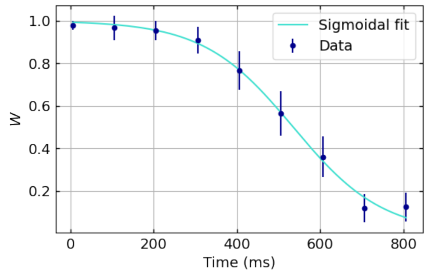


(b) Logistic fit (solid light line) over data (dark blue dots) exhibiting a slow decay rate. The half time constant of decay extracted from the fit in this dataset is found to be $\tau_0 = 534 \pm 18$ ms.

Figure 3.21: Examples of the fit performed to extract the lifetime of the currents. The systems exhibits different behaviors depending on the decay rate of the current: when the decay is fast, an exponential behavior is fitted with great confidence (a), otherwise a plateau appears and a good agreement is obtained by fitting a logistic curve (b).

very important: the probability of removing an obstacle, which is indirectly related to the density of resulting obstacles in the torus, and the size of the unitary cell. This last, is indeed a very relevant parameter, since it directly defines the inter-obstacle distance. We have optimized it for obtaining the the most visible effects and, at the same time, to guarantee the possibility for the superfluid to flow between two obstacles. To optimize it, a lattice with all sites occupied (full lattice, in the latter) is taken into account: we observed the system at long evolution times (750 ms) and varied the cell size. It was found that, increasing the cell size, a critical value appear, for which the circulation from being still, starts to flow. The critical behavior appears when the cell size is between $5/4$ and 2 times the obstacle size (which is 1 $\mu$m). Therefore in the following, the data that will be presented are obtained with the optimized parameter of $7/4$ times the obstacle size.

We are now able to define the disorder density by counting the number of removed obstacles inside the torus, over all the available sites. The second kind of measurement performed is indeed based on the variation of the disorder density: a typical example is reported in fig. 3.20a where the lifetime measurements are shown for different disorder probabilities $1 - p$.

From each dataset it is possible to extract the corresponding decay rate. From fig. 3.20, it is possible to observe that not all the datasets exhibit the same trend. Indeed, when a faster decay takes place we observe an exponential behavior, as reported in fig. 3.21a. Instead, when the decay happens later, a previous plateau at the initial circulation is detected, and we fit this behavior in excellent agreement with a sigmoid function (see fig. 3.21b). In particular, above the class of sigmoid functions, to perform the fit we employ a logistic curve, defined in general by $f(x) = \frac{L}{1+e^{-(t-t_0)/\sigma}}$. In our case, we have the restriction to work between 0 and 1, and the steepness must be decreasing,

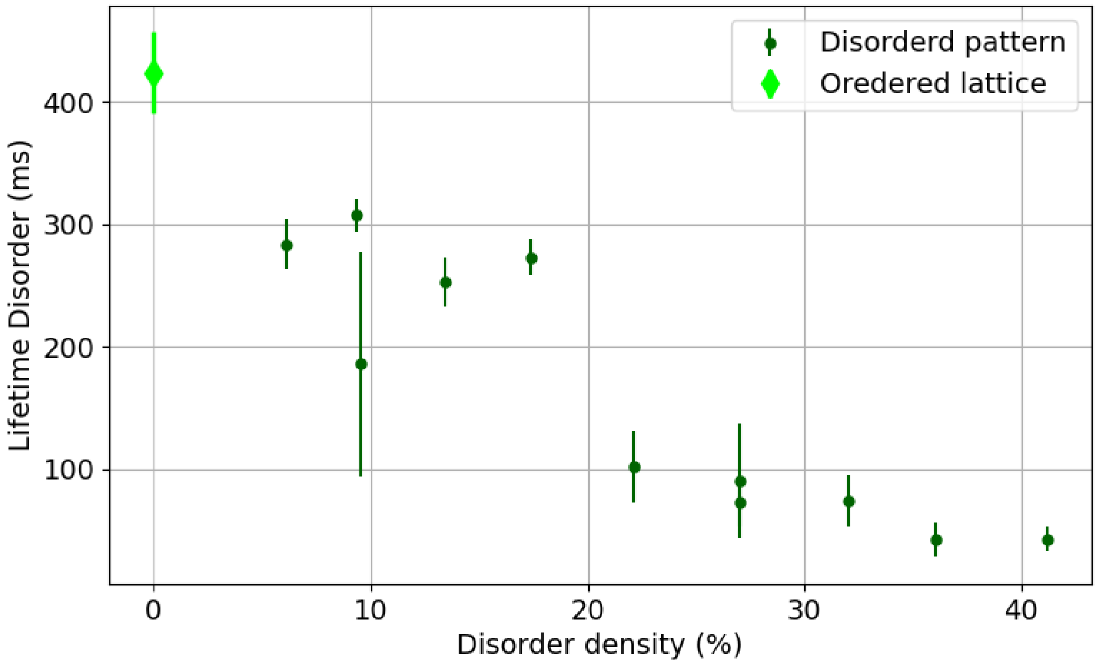


Figure 3.22: Extracted constant of current decay for different densities of disorder. The light green point is an average of all the measurements performed with a full lattice: when the disorder intensity is increased, the decay happens in faster time-scales. The monotonic behavior seems to have a critical point at disorder density 20% after which lifetime are significantly shorter.

so:

$$f(x) = 1 - \frac{1}{1 + e^{-(t-t_0)/\sigma}} \,. \tag{3.8}$$

The parameters that are thus entering in the fit are $\sigma$, which is the steepness of the curve, and $t_0$, which is the point in which the function assumes its half value. In order to be able to compare results from logistic and exponential fit, we extract the halftime constant from the exponential constant $\tau$ of the exponential fit:

$$\tau_{1/2} = \tau \cdot \ln 2 \,. \tag{3.9}$$

The first results we report concern the analysis of the behavior of the current with respect to the density of disorder. We keep the intensity of the obstacles fixed (such as in measurement of fig. 3.20a) and we vary the probability of disorder. Then we re-scaled it into the disorder density, as explained above, and extract the constant of decay from the lifetime measurements. Results are reported in fig. 3.22: since datasets are taken in different days[2], more lifetimes of the ordered full lattice are measured as a reference:

[2]Since every point of the image is an extracted constant of decay, we usually need around 10 points of the lifetime measurement to obtain a reasonable fit. Every of those points is then an average over at

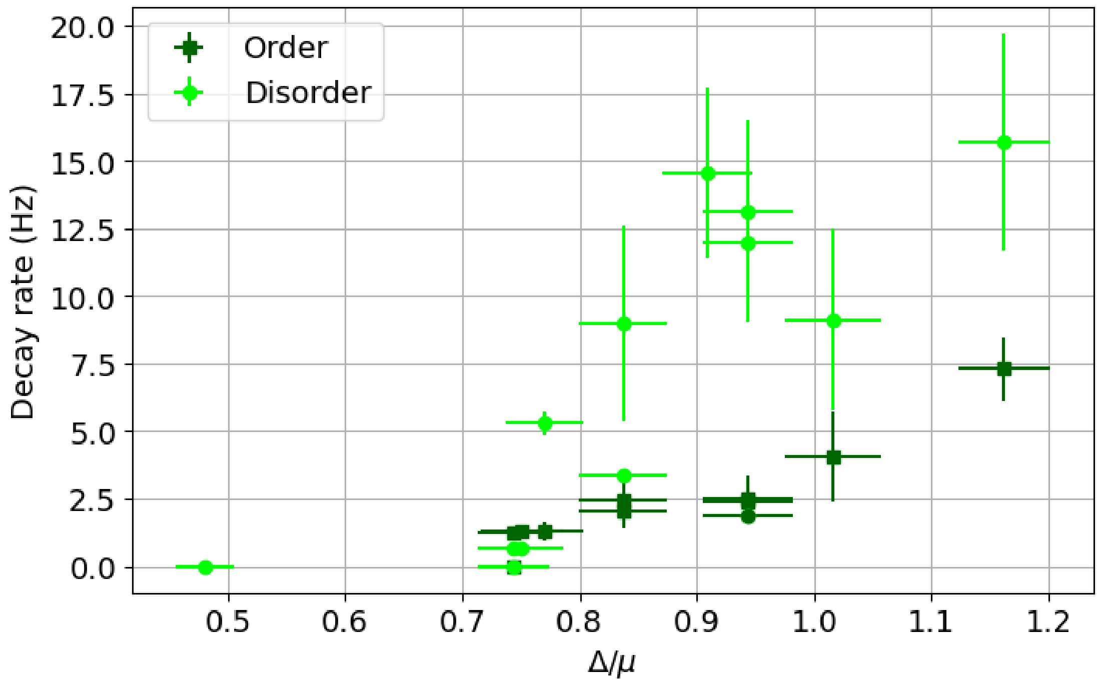


Figure 3.23: Results for the decay rate of the current versus intensity of the obstacles re-scaled over the chemical potential. Both ordered (dark green) and disordered (light green) cases are studied: when $\Delta \approx \mu$, the disordered patterns cause a decay that can be up to 5 times faster than that of the ordered full lattice.

they are all consistent and they've been averaged constituting point at 0% of disorder density.

From figure 3.22, it is possible to observe a very peculiar trend: it behaves like a two-valued step function, with a critical disorder density of about 20%. First of all, a clear sign of faster decay is observed in presence of disorder. Moreover, it seems that the increase of disorder density affects the currents, and make them decay quicker. This dependence is not trivial but it seems to be triggered by some critical value: first, if a small quantity of disorder is added by removing a few number of obstacles from an ordered full lattice, the current decays a bit faster. But when the number of removed obstacles reaches the critical value of 20% of the total available sites, the decay is much faster, quicker than 100 ms.

Since the procedure we follow is based on the idea of removing the obstacles, it is impossible to assert that the observed effect is due to the fact that we stop the current by creating a barrier or similar, and has to be addressed to the disorder itself.

least 20 images, and the sequence to capture an image lasts around 14 seconds. As a consequence, it is not possible to perform measurements in a single working day. This is indeed a good proof of reliability of the results.

The second main result is plotted in fig. 3.23: in that case the quantity we keep fixed is the disorder probability (as in the measurements of fig. 3.20b) and instead we vary the intensity of the obstacles. The interesting thing is to compare the effect of the disordered pattern with that of an ordered one: we indeed performed the same measurements both at disorder probability $1 - p = 30\%$ (light green in the figure) and with an ordered full lattice (dark green points). In figure, we show the decay rate, measured as the inverse of the decay constant, as a function of the intensity of the obstacles re-scaled over the chemical potential ($\Delta/\mu$). Both the datasets exhibit a faster decay rate with increasing the intensity of the obstacles, but a clear difference arises in the slope of the trend. When $\Delta \approx \mu$, the disordered pattern causes a decay which is up to 5 times faster than what the ordered pattern does.

The results we found are very promising and clearly indicate that a disordered potential plays a non-trivial role in the dynamics of the persistent currents and in superfluid systems in general. The system is indeed very complex, and many phenomena takes place; in particular, impurities and vortex pinning that can arise from them (see sect. 3.4), strongly correlates the studied phenomenology with that of granular high-temperature superconductors, opening the field to more comprehensive studies to investigate the nature of superconductivity.

# Chapter 4

# Outlooks to dynamical instabilities

In the chapter we are approaching, the main focus is to provide some outlooks to the studies already performed. Thanks to the tunability of most of the parameters of the system presented in the previous chapters, some more complex geometries can be explored. A straightforward very interesting outcome of this job consists in the creation of a double ring geometry, and the consequent study of the dynamical instabilities emerging from the counter propagating flows in the two rings.
Some analysis and measurements have been performed as a proof o principle for the realization of these proposals, and they constitute the basis of work for future studies that are now possible. Therefore we will firstly present the accessible geometry and the arising critical phenomena such as the Kelvin-Helmholtz (KH) instability; then, we will provide the results of preliminary analysis and simulations acting as a background for near-future studies. All the results that will be presented in this chapter are relative to the unitary regime of superfluidity.

## 4.1 Double ring geometry and KH instability

The interest to create a double ring geometry arises from the possibility to study non trivial phenomena concerning the interactions between the two rings. Since in the previous chapters we've extensively presented the persistent currents in fermionic superfluids, the double ring geometry would allow to investigate the possibility to transfer angular momentum - and thus current - from one ring to the other, Josephson effects between annular condensates, or even quantum hydrodynamical instabilities in the interface between the rings. One of the most fascinating instabilities concerning two parallel fluid streams is the Kelvin-Helmholtz (KH) instability: it was firstly formulated by Lord Kelvin [101] and Helmholtz [102] in the 19th century in the field of classical fluid theory: it foresees that when two fluids with different velocities enter in contact, the interface is not stable and rolls up forming the very famous Kelvin-Helmholtz waves, that are present in a variety of physical systems such as cloud formation on Earth, at-

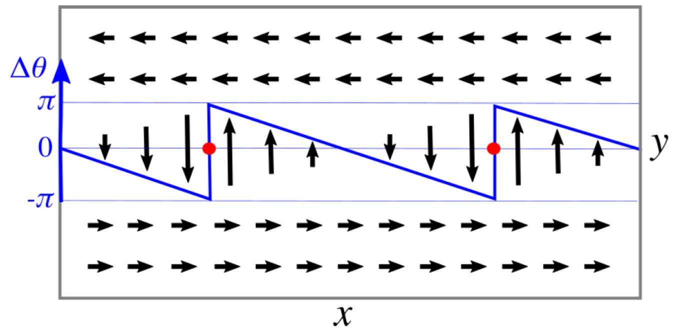


(a) Explanation of the formation of vortices at the interface between two counter flowing identical superfluids: since the phase has $2\pi$ jumps, the velocity field along the interface rapidly switches direction. The combination of this motion with the initial one, gives born to topological defects in correspondence to the phase jumps.

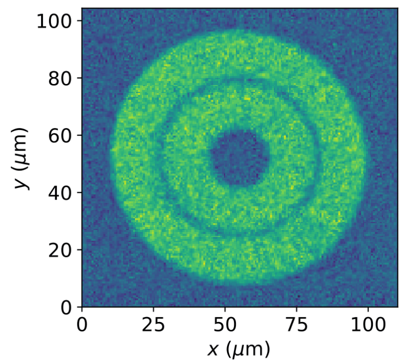


(b) In situ image of the geometry used for KH experiment: the gas is loaded in two homogeneous rings, with dimensions: internal radius 15 $\mu$m, radius of the separation barrier 30 $\mu$m, external radius 45 $\mu$m.

Figure 4.1

mospheres of planets and moons, Red Spot on Jupiter, plasma coronas of Sun and other stars, and also in the deep ocean.

In the field of superfluidity, a lot of works have studied instabilities (including also KH effects) arising at the interface between two different superfluids [103, 104]. Also the interface between superfluid and normal fluid [105, 106] and that between two immiscible binary BEC [107–109] have been widely investigated. Still, no experimental observations of a single superfluid KH instability have been obtained yet. It is indeed not trivial to detect this kind of instability, since it is usually not possible to easily distinguish the interface between two touching sides of a single superfluid moving with different velocities. Recently, it has been proposed to study KH instability by using persistent currents [110]: two binaries were simulated in which persistent currents flow in opposite directions; the binaries are separated by a Gaussian barrier.

When removing the barrier, the two flows come into contact. Now, at the interference, there exists a discontinuity in the condensate phase $\theta$, as shown in fig. 4.1a. This phase difference has a saw-tooth profile along the channel because the phase wraps between -$\pi$ and +$\pi$. Since the velocity is proportional to the gradient of the phase, also a saw-tooth velocity field appears along the channel. In the interface, when the phase jumps of $2\pi$, the velocity discontinuosulsy switches its direction, and this happens $\Delta W$ times (where $\Delta W$ is the difference between the winding number of the two persistent currents). When superposing this velocity field with the original one due to the persistent currents motion, it gives rise to a circulating flow around this points at the interface, which thus immediately evolve into quantized vortices.

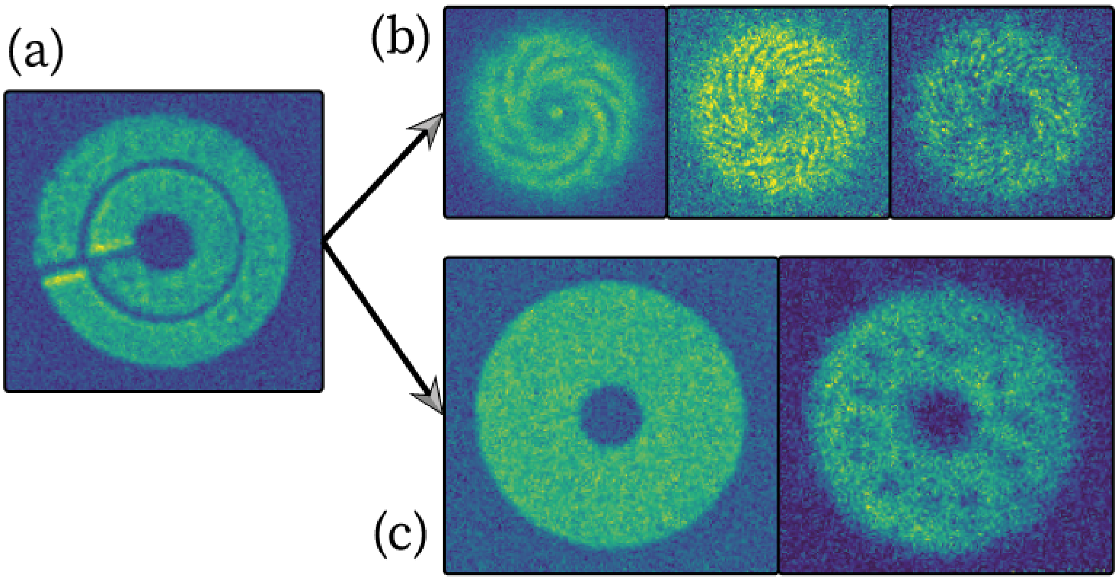


Figure 4.2: Procedures to obtain spirals and vortices in a double ring geometry. In both cases persistent currents are excited by phase imprinting opposite phase gradients on the two rings (a); then, if the trap is switched off and we make the rings interfere (b), it is possible to obtain the relative winding number. In the upper right panel it is shown that higher winding numbers are easier to be excited in this geometry (respectively we counted 7, 14, and 30 spirals from left to right). On the other side, if the separating barrier is removed (c), the flows enter in contact and by time-of-flight imaging it is possible to monitor the evolution of the interface between the two flows by looking at the position of the vortices.

The formation of vortices becomes thus the sign of the interface between the two parts of the superfluid, and thus by looking at the vortex dynamics it is possible to monitor the interface instability. The idea of the experiment proposed in this outlook, it is exactly this one. Experimentally, it is possible to work in a geometry such as that presented in fig. 4.1b: with respect to the previous experiments, we added an external ring: the inner disc is not necessary anymore, since it is possible to make the two rings interfere and look directly at their relative phase difference. As visible in the figure, we work with a larger geometry in order to be able to study also the vortices dynamics after their generation. The procedure to load the gas in the trap is similar to the one described in fig. 2.11; the difference in the process is that now we add a step in which the internal hole is carved very slowly and adiabatically. Then, as usual, the separation barrier is ramped up and the diametrical barrier is ramped down. When the gas is ready, we generate persistent currents by phase imprinting (see ch. 2.3) opposite phase gradients on the two rings (the result is shown in fig. 4.2(a) ).

At this point, as shown if fig. 4.2(b), a possibility is to make the two rings interfere in time-of-flight (TOF) to calibrate the phase imprinting technique on this new geometry.

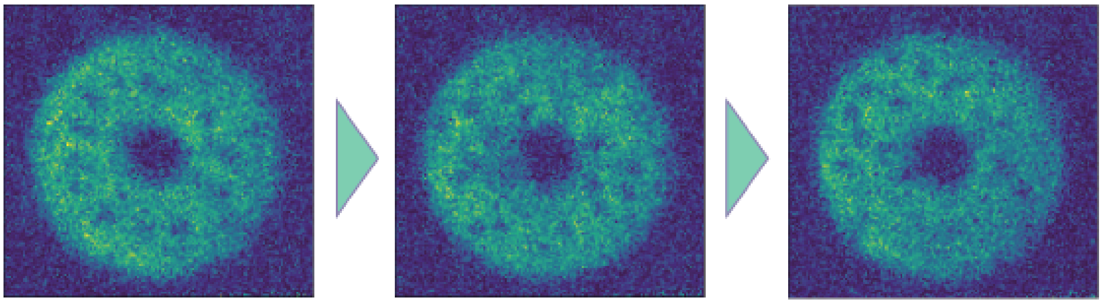

Figure 4.3: Evolution of the interface monitored by the presence of the vortices. From left to right the images correspond to 5 ms, 35 ms, and 45 ms of evolution time after the two rings have come into contact. The interference is clearly unstable and sometime it seems to detect clusters of vortices.

As is it visible in the figure, in this new geometry it is easier to obtain also higher circulating superfluids (we observed up to 30 spirals) without loosing accuracy in the excitation of low winding number states. The measure of the number of spirals, is in this case the exactly measurement of the number of phase jumps that would result by lowering the separating barrier and bringing the flows into contact. Therefore, by counting the number of spirals, it is possible to predict the relative winding number and thus the number of vortices expected in a KH-like experiment. The procedure to explore KH instability is instead shown in fig. 4.2(c): after the phase imprinting the barrier is lowered without turning off the trap. Since the superfluid in the two ring is identical, it is not be possible to distinguish the interference by in-situ imaging the cloud. Instead, by taking a TOF absorption imaging, holes appear in presence of quantized vortices, since the density in the core is vanishing (see ch. 1.3.2). By looking at the position of the vortices, it is then possible to monitor the interface evolution.

An evolution in time of the interface is reported in fig. 4.3: at the beginning the interface seems to be stable for a couple of time (10-20 ms), while then it becomes unstable. We observed that the typical time in which the instability occurs depend on the number of vortices. As a qualitative result, more vortices cause the instability to happen faster. It was also observed in some images, that the evolution of the position of the vortices sometimes brings them to agglomerate and form clusters. The KH instability indeed would consists in this phenomenon: the counter propagating flows, cause the interface, and thus the vortices, to start to roll up and, as simulated in ref. [110], to form clusters. Actually, the measurement is more accurate when an high number of vortices defines the interference between the counter propagating flows, so this would be an important aspect to take into account for high-quantitative analysis in future experiments.

## 4.2 Analysis to detect KH instability

As possible ways to quantify the presence of the KH instability, we report now some quantitative analysis which can be performed. The route we propose is based on the detection of the vortices positions from the acquired images. The possibility of extracting vortices coordinates from the images is very powerful, since it is then possible to work with a relative small amount of data, and obtaining at the same time a great amount of information, as we will see in the following sections. Therefore the first step consists in building a procedure to detect vortices from an image.

### 4.2.1 Image processing for vortex detection

In order to study the evolution of the vortices position in time to detect the arising of the KH instability, many images need to be taken at different times. Moreover, since the timescales seem to vary a lot depending on vortices number (and thus difference of velocity in the counter propagating flows), a dense sampling is often required. It is now clear that in order to obtain statistically relevant results, a large amount of data has to be taken; thus, an automatized procedure to analyze the images becomes essential.

The procedure that we have employed is shown in fig. 4.4: after loading the raw image, we select only the doughnut region in which there are the atoms; to do this, we find the active region with usual methods as explained in ch. 2.2, and then we manually put zero value everywhere else. Then, the values measured by the camera are normalized to obtain the result in fig. 4.4(b). It is now possible to perform an image denoising using the Non-local Means Denoising algorithm, which considers the noise as Gaussian and white. A parameter regulating filter strength is carefully chosen to remove noise but preserving image details. Then the image is re-normalized with a 32 floating point precision resulting in fig. 4.4(c) and finally the exponential of the image is taken (fig. 4.4(d) ). At this point the image is ready to start the research for vortices: an algorithm which finds local maxima has been lunched, with some constrains. In particular, a peak is considered if its value is at least 55% of the maximum value of the image, and two peaks are considered separated if their distance is greater than 10 pixels. Every peak is thus collected (a found peak correspond to a sign in fig. 4.4(e) ): if its distance from the borders is lower than 8 pixel, the peak is discarded. Otherwise, a two-dimensional Gaussian fit is performed in a region of $16\times16$ pixels around the position of the peak. In case the fit satisfies given requirements (concerning minimal and maximal amplitude, and goodness of the fit estimated thanks to the $R^2$ parameter) the coordinates of the vortex are collected, otherwise it is discarded. This operation is repeated for each image of the dataset, and thus the obtained information mainly concerns: number of vortices per image and coordinates (both in Cartesian or polar systems) of each vortex.

The obtained results are quite affordable although some of the discussed parameters have to be tuned from dataset to dataset, because their optimal value strongly depends on day-to-day variable characteristics such as number of atoms in the ring and visibility of the vortices.

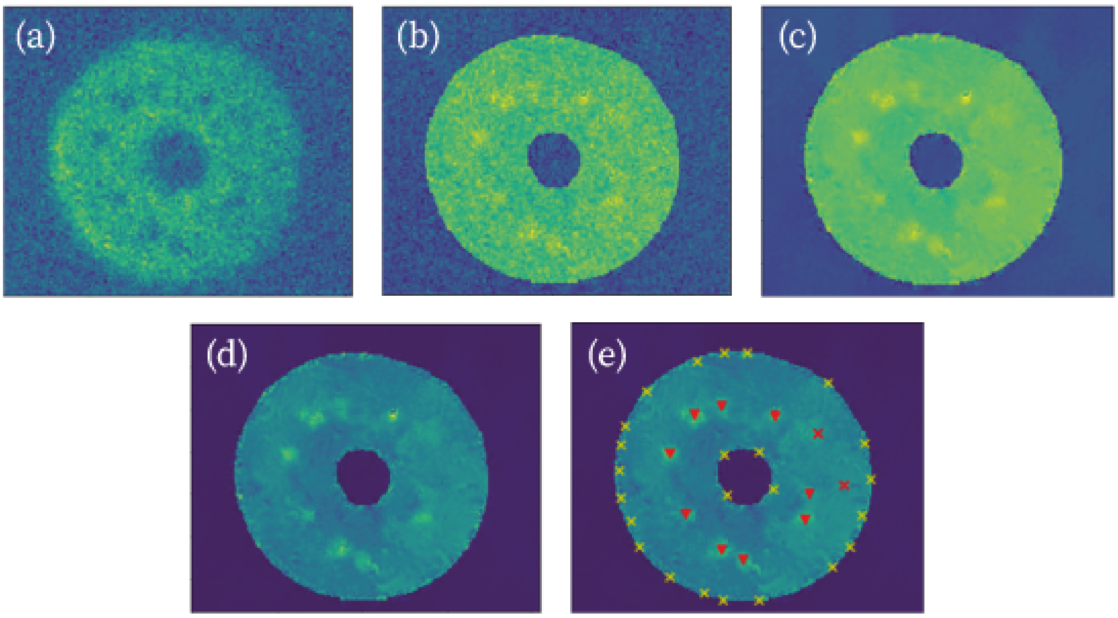


Figure 4.4: Image processing to detect vortices: a raw image (a) is collected from absorption imaging of the atomic cloud, the image is then cleaned by considering only the active area of the doughnut (b), and a denoising algorithm is performed (c). Finally the exponential of the image is taken (d) and the peaks of the resulting image are searched and collected. The peak has to be far enough from the borders of the ring and it must satisfy requirements of goodness after a 2D Gaussian fit is performed. In image (e) the yellow crossing points are the peaks discarded because they are too close to the borders, the red crosses are those that do not satisfy good results from the fit and finally the triangular red ones are the accepted vortices.

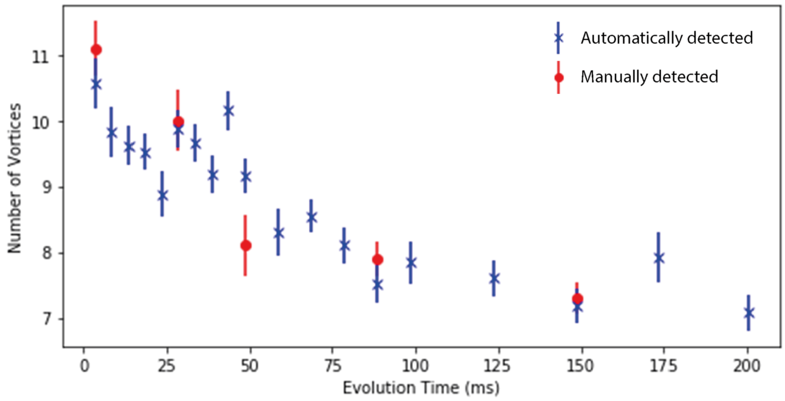


Figure 4.5: Evolution in time of the mean number of vortices in the the ring. Each point of the graph (blue crosses) is the average over 20 images of the extracted number of vortices, with the relative errors due to the standard deviation of the mean. A comparison with the data detected by hand (red dots) is provided to proof the reliability of the automatized discussed procedure.

We report, as an example, the results obtained for the evolution of the number of vortices in time: in figure 4.5, the results from the discussed automatic procedure are compared to some manually obtained results. By "manually obtained" we mean that, for some evolution times, vortices are detected by eye. For each evolution time, 20 images are taken and the number of vortices for each image is collected. Their averages are then plotted and the results is that the mean number of vortices decreases in time. This can be due mainly to two phenomena: the first possibility is that the vortices exit from the ring and goes inside it (increasing the circulation of the atoms) or outside it (lowering it). Another possibility is that the vortices merge with one another while moving. Although this last hypothesis is not supported by the observation of larger holes (which actually we are not sure to be able to detect the difference), it is indeed suggested by the fact that in general faster decays are observed with higher initial number of vortices. This is not actually a proof, since a lot of reasons can be adduced to explain it, such as the fact that, when just a few vortices are present, each vortex feels a lower velocity field due to the contribution of the others, thus the dynamics is slower; as a consequence, also the motion to the borders would maybe be affected by the number of vortices in the ring.

Let's now discuss about the other important information we can extract from the procedure to analyze the images, i.e. the coordinates of the vortices. This is indeed the most powerful information, since it can be used to monitor the dynamics and extract relevant physical quantities of the system.

### 4.2.2 Point vortex model

A first analysis which can be performed with the coordinates of the vortices is based on the idea of simulating the velocity field generated by the given configuration of vortices. The goal is to be able, following the method suggested in ref. [110], to extract a "shear viscosity" of the superfluid.

It is possible to compute the velocity field both with Gross-Pitaevskii simulations (whose validity is though restricted to the BEC regime only) or modeling the vortices with the point-vortex model, whose regime of validity across the BEC-BCS crossover has recently been proved [111]. The idea of the point-vortex model is to consider each vortex as a point-like object, thus neglecting the finite size of the core. The generated velocity field is trivially dependent only by the distance of the center of the vortex and has no radial component: $v = \frac{\hbar}{m}\frac{1}{r}\hat{\mathbf{e}}_\vartheta$ where $\mathbf{r}$ and $\boldsymbol{\theta}$ are respectively the radial and angular coordinates of the system having center corresponding with the position of the vortex.

The main issue concerning the usage of the point-vortex model, is constituted by the problem of the boundary conditions. What is necessary is that the total velocity field of the system has vanishing normal component at the torus boundaries. This is due to the definition of the boundaries, since they cannot be pierced. When dealing with linear geometries, in which the boundary is constituted by a straight line, the problem is solved in a quite simple way: a fictitious image vortex is placed on the other side of the boundary at the same distance, and thus all the boundary conditions are satisfied. Such as the image charge in electromagnetic problems, a simple solution is obtained also when dealing with spheres (or circles in two dimensions). What is not trivial is indeed to find a way to respect the boundary conditions in a simply connected geometry such as the annular one, which we are dealing with. The main problem is that there are two separated boundaries on which the normal component of the velocity has to vanish. If an image vortex is placed outside the ring, on the external boundary everything is right, while, on the internal one, the normal component can never be zero.
The solution consists in considering, for each vortex in the torus, an infinite number of fictitious image vortices [112], each one with an appropriate position and circulation. Let's consider the case of a torus with internal radius $R_1$, an external radius $R_2$, and a vortex inside the ring with winding number $W$ (the procedure has to be repeated for each vortex) located at $\mathbf{r}$ from the center of the torus (taken as the origin of the frame). To cancel the normal component at the boundaries, we have to consider two classes of image vortices: to fulfill boundary conditions on the inner radius, a first image vortex with charge $-W$ and position $r_{im1} = \frac{R_1^2}{r^2}\mathbf{r}$ has to be placed, together with an image vortex at the origin with charge $W$. The image vortex located at $r_{im1}$ now produces a normal component on the outer radius, that has to be erased with an image vortex at $r_{im2} = \frac{R_2^2}{r_{im1}r}\mathbf{r} = \frac{R_2^2}{R_1^2}\mathbf{r}$ having winding number $W$. This external image vortex, induces a normal component on the inner radius, therefore another internal image vortex has to be placed at $r_{im2} = \frac{R_1^2}{r_{im2}r}\mathbf{r} = \frac{R_1^4}{R_2^2 r^2}\mathbf{r}$ with circulation $-W$ together with an image vortex placed at

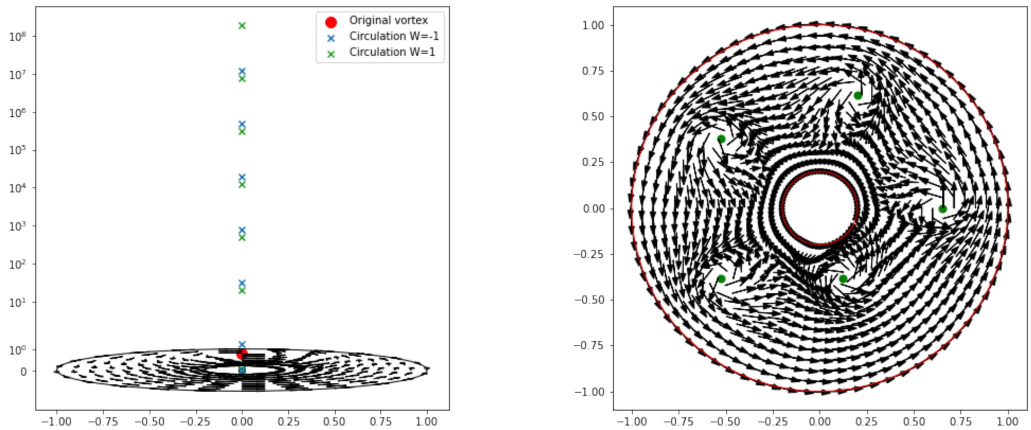


(a) Scaling of the position of the fictitious image vortices used to fulfill boundary conditions on both inner and outer radii of the torus. Note the logarithmic y-axis. An infinite number of vortices would be needed, but actually after 11 simulating steps the accuracy is of the order of $10^{-9}$. Image vortices are indicated with crosses, while the real one is a red dot.

(b) Simulation of the velocity field inside the torus generated by a generic five vortices distribution. Vortices are represented as blue dots, while torus boundaries (on which normal component of the velocity field vanishes) are highlighted by a red line. At each point of the space, the direction of the intensity field is given by the direction of the arrow based in that point.

Figure 4.6: Simulation of the vortices velocity field in a torus with condition of vanishing normal component on the boundaries.

the origin with charge $W$. These last vortices induce again a normal component of the velocity field on the outer radius that has to be erased by adding another external image vortex and so on and so forth. To sum up, this first class of vortices - when completed - erases entirely the normal component of the velocity field on the internal boundary, and, on the external radius, erases the normal component of the velocity field due to all the image vortices placed. The second class of image vortices will finish the job fulfilling the boundary condition on the external radius. To do so, an image vortex is placed at $r'_{im1} = \frac{R_2^2}{r^2}\mathbf{r}$ with $-W$; its velocity field's normal component on the inner boundary is erased by an image vortex at $r'_{im2} = \frac{R_1^2}{r'_{im1}r}\mathbf{r} = \frac{R_1^2}{R_2^2}\mathbf{r}$ with charge $W$ and another in the center with circulation $-W$. To balance them another external fictitious vortex at $r'_{im3} = \frac{R_2^2}{r'_{im2}r}\mathbf{r} = \frac{R_2^4}{R_1^2 r^2}\mathbf{r}$ with $-W$ will be placed, and so on and so forth.

Computationally it is observed that the convergence of this method is quite fast: a precision can be arbitrarily set and the procedure continues until it is reached. In our simulations, the given $1{\cdot}10^{-8}$ precision of vanishing normal component on both the boundaries has been achieved within 11 steps. It is also observed that the maximum computational available precision is $2{\cdot}10^{-14}$.

We report in figure 4.6 the results of our simulation with the discussed characteristics. On fig. 4.6 a logarithmic y-axis is used to show the spatial scaling of the image vortices, while in fig. 4.6b the simulation of a generic 5 vortices velocity field has been computed. With this analysis it is thus possible to obtain the velocity field of the superfluid (which is not a directly accessible quantity in experiments) starting from the coordinates of the vortices which are available thanks to the procedure discussed in section 4.2.1.

### 4.2.3 Cluster analysis

The last kind of analysis we want to propose, aims to detect quantitatively a trace of the Kelvin-Helmholtz instability. A clear sign of the presence of KH instability in our system, would be given by the clusterization of the vortices [110]. In order to quantify the presence of clusters in the torus, we apply the Ripley's $K$ function and its normalization known as Besag $L$ function to the vortices coordinates..

Ripley's function is a statistical pattern analysis method used as a measure of spatial clustering which has already been employed in order to classify quantized vortices in condensates [113]. Let's assume, as it should be in our case, that all the vortices have the same sign. Having $N$ vortices in a total area $A$ in which the condensate is trapped, the Ripley's function can be expressed as

$$K(r) = \frac{A}{N^2} \sum_{i=1}^{N} \sum_{j=1}^{N} f_{i,j}(r) \tag{4.1}$$

where $f_{i,j}(r)$ is a function assuming value 1 if the vortex $j$ is located within a distance $r$ from the reference vortex $i$, and 0 otherwise ($f_{i,j}(r) = 0$ also if $i = j$). In other words (as represented in fig. 4.7a), being $r_{i,j}$ the distance between two vortices $j$ and $i$, used as a reference, it is possible to define

$$f_{i,j}(r) = \begin{cases} 1 & \forall r_{i,j} < r, \quad i \neq j \\ 0 & \forall r_{i,j} > r \quad \text{or } i \neq j \end{cases} \tag{4.2}$$

The meaning of the $K$ function is to count the vortices within an area of radius $r$ and compare the density of vortices per unit of area in this region, with that of the whole area of the condensate. Clustering results in the $K(r)$ function, if it increases faster than $K^{Poiss}(r)$, which is the Ripley's function for random distributed vortices. In this last case, when the distribution of vortices follows the Poisson distribution, $K$ function scaling is $K^{Poiss}(r) = \pi r^2$, thus parabolic. Therefore, it is possible to detect the presence of cluster of vortices by comparing the obtained $K(r)$ with the predicted random value of $\pi r^2$: if the scaling is greater, it means that clusters are present.

When dealing with systems in which the size of the searched clusters is of the same magnitude order of that of the system, it happens that the finite size of the condensate

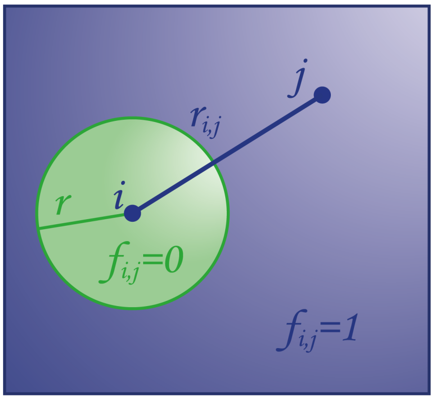


(a) Ripley's $K$ function computes the density of vortices in an area of radius $r$: if it is greater than the density of vortices in the total area, it is a sign of formation of clusters. Referring to eq. 4.1 in the text, $f_{i,j}(r)$ vanishes if vortices $i$ and $j$ are more distant than $r$ and equals 1 otherwise.

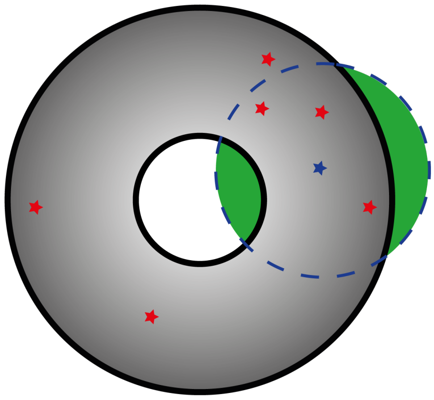

(b) Boundary corrections in Ripley's $K$ function. When computing $f_{i,j}(r)$, it is possible that a part of the area of radius $r$ exceeds the boundaries of the condensate area. In the example in figure, stars represent vortices: the green areas have to be subtracted because there cannot be vortices since there's no gas.

Figure 4.7: Explanation of the Ripley's $K$ function (a) and of its boundary corrections in a annular geometry (b).

fakes the value of Ripley's function. To understand this phenomenon and look for a solution, let's consider for example a vortex near a boundary: when this vortex is taken as a reference (as the vortex $i$ in eq. 4.1), by increasing the radius $r$ within which looking for other vortices, a great amount of the spanned area is not included in the region where the superfluid is. As a consequence, there can be no vortices and the density of vortices will for sure decrease. Thus, some boundary corrections have to be included, by taking into account the amount of area which effectively is a superposition of the two under consideration (see fig. 4.7b). In cases of simple geometries, such as circles or rectangular shapes, the correction have already been computed. In an annular geometry it has not been done yet.

Therefore we had to calculate the corrections for this geometry. Let's take a look at fig. 4.7b: the idea it to calculate the area enclosed in the dotted blue line, and subtracting the green areas which are not part of the condensate, by taking into account all the possibility values of $r$ (radius of the blue dotted circumference). We will consider an annular condensate with internal radius $R_{in}$, external radius $R_{ext}$, and we assume to being at the step of calculating the vortices within a radius $r$ from a vortex $i$ whose coordinates are $x$ and $y$. Let's define thus $d \equiv \sqrt{x^2+y^2}$ and the following useful quantities:

$$A_{in} = R_{in}^2 \arccos\left(\frac{R_{in}^2 - r^2 - d^2}{2R_{in}d}\right) + r^2 \arccos\left(\frac{r^2 - R_{in}^2 + d^2}{2rd}\right) + \\ - \frac{1}{2}\sqrt{(2R_{in}d)^2 - \left(R_{in}^2 - r^2 + d^2\right)^2} \quad (4.3)$$

and

$$A_{ext} = R_{ext}^2 \arccos\left(\frac{R_{ext}^2 - r^2 - d^2}{2R_{ext}d}\right) + r^2 \arccos\left(\frac{r^2 - R_{ext}^2 + d^2}{2rd}\right) + \\ - \frac{1}{2}\sqrt{(2R_{ext}d)^2 - \left(R_{ext}^2 - r^2 + d^2\right)^2} \quad (4.4)$$

It is now possible to split the problem in different sub-cases obtaining the following results: the area $A^{red}$ has been calculated, which is the superposition of the area of the circle of radius $r$ and the region is which the condensate is present. It holds:

$$A^{red} = \begin{cases} \pi r^2 & \text{if } r + R_{in} \leq d \leq |r - R_{ext}| \\ \pi r^2 - A_{in} & \text{if } d \leq |r - R_{ext}| \wedge r - R_{in} < d < r + R_{in} \\ \pi r^2 - \pi R_{in}^2 & \text{if } d < |r - R_{ext}| \wedge d < r - R_{in} \\ A_{ext} & \text{if } d > |r - R_{ext}| \wedge d \geq r + R_{in} \\ A_{ext} - A_{in} & \text{if } d > |r - R_{ext}| \wedge r - R_{in} < d < r + R_{in} \\ A_{ext} - \pi r^2 & \text{if } |r - R_{ext}| < d < r - R_{in} \end{cases} \quad (4.5)$$

As said, this correction has to be applied to each step in calculating Ripley's $K$ function, then a factor $A/A^{red}$ is multiplied, so that the corrected formula becomes:

$$K(r) = \frac{A^2}{N^2} \sum_{i=1}^{N} \frac{1}{A_i^{red}} \sum_{j=1}^{N} f_{i,j}(r) \quad (4.6)$$

To obtain a linear scaling of Poisson-distributed data, it is common to normalize the Ripley's function to obtain the so called Besag's function:

$$L(r) = \sqrt{K(r)/\pi} - r \quad (4.7)$$

which can be scaled to a characteristic radius of the condensate that we identify as $r_c = R_{ext}$ to obtain

$$L\left(\frac{r}{r_c}\right) = \sqrt{\frac{A}{\pi r_c^2 N^2} \sum_{i=1}^{N} \sum_{j=1}^{N} f_{i,j}\left(\frac{r}{r_c}\right) - \left(\frac{r}{r_c}\right)^2} - \frac{r}{r_c} \quad (4.8)$$

From Besag function is it straightforward to detect the presence of clusters or, on the contrary, of repulsive interaction: when the vortices are distributed in a Poisson distribution $L(r/r_c) = 0$, while it assumes positive values up to 1 in case of clusters, and negative values (up to -1) in case of dispersed vortices.

We report in fig. 4.8 the results for two example distributions of vortices obtained by the automatized procedure explained in sect. 4.2.1 applied to two images relative at different evolution times of the system. We plot the computed Ripley's $K$ functions on the left, and the Besag functions on the right. In the first reported case, a Poisson

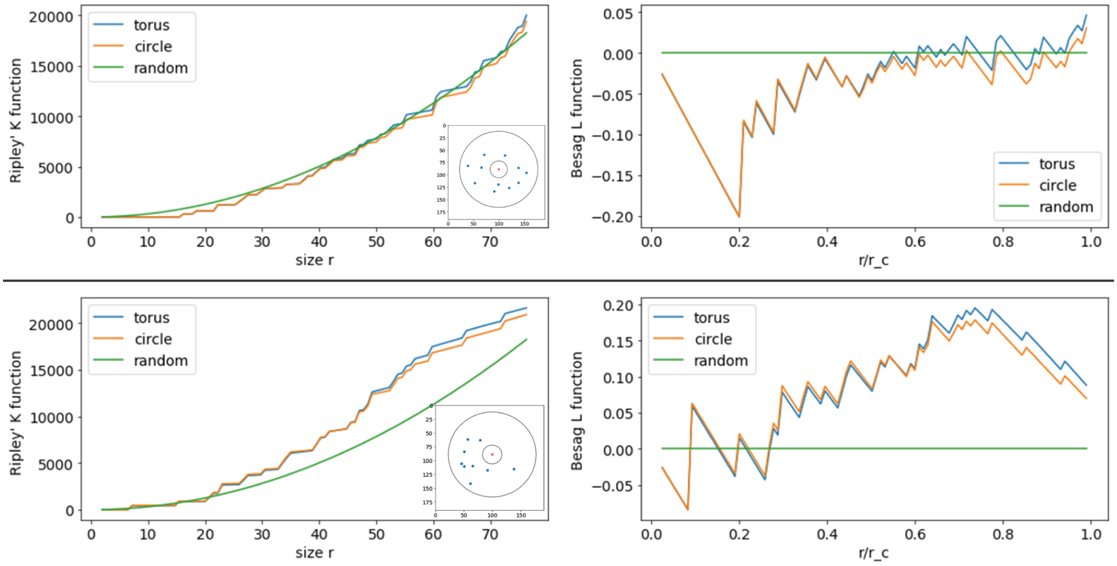


Figure 4.8: Examples of the computation of Ripley's $K$ function and Besag's one. Upper and lower panels represent different configurations of vortices, which are shown in the insets of images on the left. Upper, a Poisson distribution of vortices is detectable since Ripley's function (on the left) reproduces very well the predicted parabola, and the Besag function (on the right) is zero valued. Lower, from the same analysis, a cluster is detectable since the functions show a super Poisson trend. For each image, the effect of the boundary corrections in a torus (in blue) are compared with those that would be applied if the geometry would be a simple disk (in orange) and the predicted behavior for a Poisson distribution (in green).

distribution of vortices is detectable since the $K$ function follows a parabolic trend, and the Besag function is zero valued. On the other side, in the second example reported, a super Poisson trend is observed, indicating the presence of cluster of size $r = 0.6 \div 0.8 r_c$ (where the Besag function is positive valued).

As a conclusion of this chapter, we sum up what it has been presented. We have proven that an experiment investigating Kelvin-Helmholtz instability can be performed. We also provided some useful analysis both concerning automatically processing the images and numerical computations based on the coordinates of the vortices. We have thus presented the necessary background and information that can act as a launchpad for near-future experiments.

# Conclusions

In this thesis work we demonstrated the realization of a new versatile platform for the simulation of superfluidity across the BEC-BCS crossover, in particular studying persistent currents and investigating its main mechanisms of decay.

In detail, we observed the phenomenon of persistent currents in fermionic regimes of superfluidity trapped in annular geometries. For the first time, we employed phase imprinting technique to excite the currents and we characterized it, both by calibrating the imprinted time needed to deterministically generate the desired winding number in the system, and also by verifying the limits of validity of the method. We detected a discrepancy in the phase which needs to be imprinted in the unitary and BCS regimes with respect to that needed in the BEC regime. We also looked at how this quantity varies by changing the scattering length and concluded that the difference can be addressed to the role of correlations in the system.

In order to detect the currents, we made use of interference methods. We theoretically calculated the expected interference pattern generated by the time-of-flight expansion of two condensates shaped as a disk and a concentric external ring. The resulted function allowed us to directly link the winding number of the circulating superfluid to the number of spirals detectable in the interference pattern. In order to count them, we also provided quantitative analyses: by fitting the radial profile of the image with a sinusoidal-like function, the slope of the resulting linear trend of the phase shift gives the number of spirals in the observed pattern.

A central result that we discussed is the observation of persistence of the currents, since we found they live longer than the system itself. This is one of the first observations of persistent currents in fermionic superfluids and it has been reported for all the three regimes in the BEC-BCS crossover. It was indeed the very first time that circulations made of winding numbers higher than one are observed persisting in Fermi superfluids. This result is very powerful and opens the fields to future studies aimed to employ ultracold quantum gases as paradigmatic controllable environments to understand superconductivity also in less predictable systems.

As a further step, we investigated the decay phenomena affecting the currents: firstly, we inserted in the ring an obstacle whose radius is comparable with the healing length of the system: this allowed us to probe for real the Landau criterion of superfluidity. We observed a decay of the currents on a timescale which depends on the number of impurities we put in the system, and we were able to compare the results with previous experiments and provide benchmark for future theories.

As a natural consequence, we have increased the number of obstacles which the persistent flow faces. We were able to address to the disorder an effect of decaying on persistent currents, both by studying the lifetimes of the flows for various densities of disorder and by comparing them with the respective results obtained with an ordered lattice. In the exactly same conditions, an ordered pattern of obstacles conduces currents for longer time than the same pattern where some random obstacles are removed. We also highlighted the possibility of exploring different statistical kinds of disordered patterns by tuning the resolution of the applied optical potentials, opening the path to future more structured studies on the field.

In conclusion, we gave also a detailed analysis of possible outlooks of this thesis, providing experiments and analysis which support our assertions: we proposed to employ our system to study dynamical instabilities, and in particular to use a double ring geometry to detect Kelvin-Helmholtz instability. We reported how it is possible to monitor the dynamical evolution of the interface and provided some very preliminary results from experiments. Moreover, different methods of analysis have been developed: firstly, a routine to process and analyze the acquired images; then, a simulation of the velocity field of the obtained generic distribution of vortices has been developed by using the point vortex model in a non-trivial annular geometry; finally, theoretic corrections for this geometry have been calculated and implemented in a statistical function used to detect presence of clusters of vortices. The reported preliminary results and analysis constitute a solid background on which it is possible to move to further studies on KH and other dynamical instabilities.

This work opens the way for new prospects to explore the concept of superfluidity in versatile systems by using arbitrary optical potentials, and to investigate the decay mechanisms taking place when a supercurrent is damped. In particular the results achieved open up the possibility to investigate more complex phenomena such as dynamical instability, quantum turbulence, and disorder effects which are ubiquitous in a variety of natural systems.

# Appendix A

# Feshbach resonances and states in $^6$Li

Lithium-6 is the fermionic isotope of lithium, which is an alkali atom having 2 paired electrons in the core, and a single unpaired electron in the valence state. The first excitation concerns this last electron, and thus being $1s^2 2s^1$ the ground state, the first excited state is $1s^2 2p^1$. The transition between these two states is a so called D-line which has a wavelength of about 671 nm (visible red light).

By taking into account the spin-orbit coupling, as for all alkaline atoms, the D-line splits in two narrower lines, D1 and D2, which link the ground state to the $2p_{1/2}$ and $2p_{3/2}$ levels respectively, where $J = 1/2$ and $J = 3/2$ refers to the total angular momentum in the fine structure. D1 has a wavelength of 670.992 nm and D2 of 670.977 nm. The ground state instead remains unperturbed.

It is moreover possible to take into account also the electronic magnetic moment and the nuclear spin magnetic moment $\hat{\mathbf{I}}$ by looking at the hyperfine structure. It is therefore necessary to use new quantum number as eigenstates of the Hamiltonian by defining $\hat{\mathbf{F}} = \hat{\mathbf{J}} + \hat{\mathbf{I}}$. In image A.1a, the states of $^6$Li in absence of external field are represented.

When an external field $B$ is applied, the Zeeman effect takes place, so that hyperfine states split up. When $B$ is small, it can be treated as a perturbation of the hyperfine levels, using common quantum numbers and thus the effect becomes $\Delta E_Z = \frac{\mu_B}{\hbar} g_F m_F B$. Instead, when $B$ assumes high values, we enter in the strong-field regime and $F$ is not a good quantum number anymore. This limit is called Paschen-Back limit, and here the hyperfine interaction is considered a perturbation of the atom-field Hamiltonian. For intermediate magnetic fields, the effect has to be computed numerically.

In figure A.1b we reported the splitting of the hyperfine ground state manifold due to the presence of an external magnetic field. The useful states for application in ultracold gases, and in particular for this work, are those labeled with $|1\rangle$, $|2\rangle$ and $|3\rangle$.

So far, only not interacting systems have been considered. Anyway most interesting phenomena happen in the interacting regime. As already mentioned in the text, the

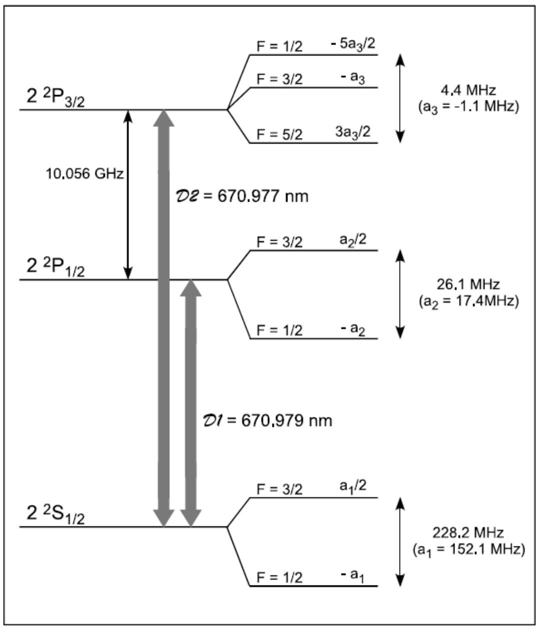


(a) Lithium-6 states at zero magnetic field. Here the structure of ground and first excited states of $^6$Li at zero magnetic field is shown; the spin orbit coupling splits the $^2$P levels and defines the D1 and D2 lines. Levels are then again split by the interaction with nuclear magnetic moment. Image taken from [114]

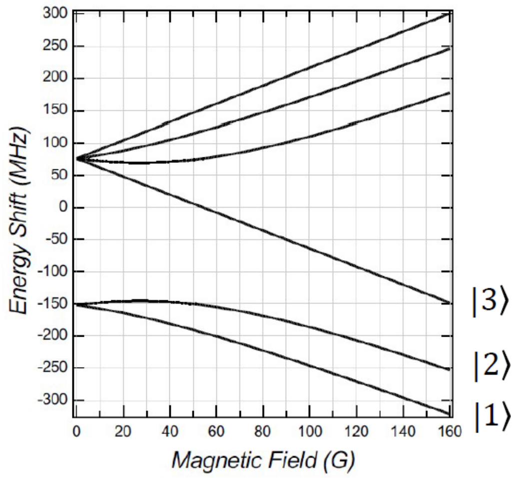


(b) Zeeman shift of the ground state hyperfine levels. By applying an external magnetic field, the hyperfine states of $^6Li$ are split: sublevels labeled as $|1\rangle$, $|2\rangle$ and $|3\rangle$ are those used for ultracold fermionic gases applications. Image taken from [114]

Figure A.1: Lithium-6 states in presence (a) and absence (b) of external magnetic field.

interactions in ultra-cold gases are well described by the Fermi pseudopotential, which mainly depends on the scattering length.

When dealing with interaction between alkali atoms in different hyperfine states, the electronic spin configuration defines a singlet and a triplet state. Before the scattering event, the incoming particles are in one of these two possible states, and therefore they define the so called open channel. The other is thus the closed channel. Now, the presence of a bound state in the close channel, modifies the scattering properties of the particles in the open one, because of the hyperfine coupling between triplet and singlet states. In case the energy of the bound state corresponds to that of the particles in the open channel, this resonance causes the scattering length to diverge. Actually this is not very common but it is a useful property: indeed, the two channels have different magnetic moments. It provides the possibility to tune an external magnetic field in order to match the two energy and make the scattering length diverge. This phenomenon is called Feshbach resonance [115].

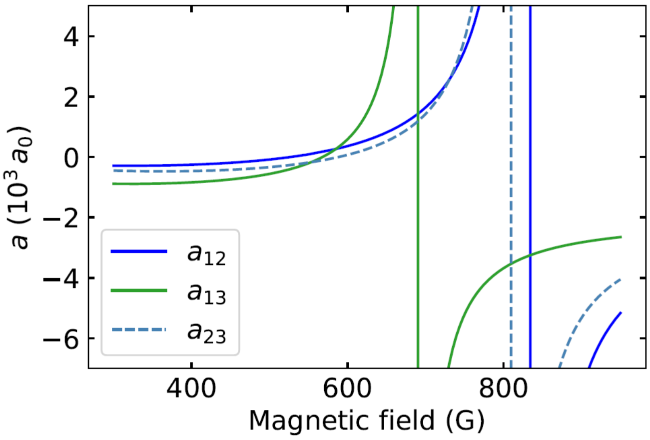


Figure A.2: Feshbach resonance in $^6$Li. Here the Feshbach resonance of the three lowest $^6$Li hyperfine states is shown against the external magnetic field $B$: by changing value of $B$ it is thus possible to tune strength and sign of interaction over a wide range of values. Image taken from [38]

The resulting dependence of scattering length from external field can be modeled phenomenologically as:

$$a(B) = a_{bg}\left(1 - \frac{\Delta B}{B - B_0}\right) \tag{A.1}$$

where $\Delta B$ is the resonance width and $B_0$ its center, while $a_{bg}$ is the off-resonance background scattering length. At the resonance, i.e. when $B = B_{=}0$, the scattering length diverges; instead, all the observable remain finite. One of the most astonishing properties of Feshbach resonances, is the possibility to tune not only the interaction strength but also its sign;. It give rise to the possibility of exploring different regime of fermionic systems.

In figure A.2 it is represented the dependence of the scattering length from the external applied magnetic field for the lowest hyperfine levels of $^6$Li. Referring to the states labeled as in figure, both resonances $|1\rangle$-$|2\rangle$ and $|1\rangle$-$|3\rangle$ are about 250 G broad; in particular the most exploited resonance in this work is the $|1\rangle$-$|2\rangle$: it is centered at about 832 G, and it is used to explore the different regimes in the BEC-BCS crossover.

# Appendix B

# Density depletion caused by phase imprinting

When employing the phase imprinting technique to produce circulations in the ring, there is a characteristic sign that it is always present right after the phase gradient pulse. If an image is taken just a few microseconds after the imprinting, this sign is well visible also by eye. An example is given in fig. B.1: the image is taken 21 $\mu$s after the light pulse. In correspondence to the phase jump of the gradient imprinted, both a depletion in the density and an accumulation of atoms appear close to each other.

This fact is due, we strongly suspect - to the anti-gradient imprinted together with the phase gradient: as a matter of fact, when a linear phase profile is generated, a slope in the opposite direction has to take place because a vertical line is not possible in any experimental system. Previous attempts involving phase imprinting technique on an atomic ring, suggested to place a barrier over the phase jump to avoid counter propagation of atoms [77]. Actually, due to the high resolution of our system, we managed to employ the technique with good results without the usage of a barrier.

The only issue we have to take into account is indeed this kind of short term solitonic excitation. The kind of density depletion or bump depends strongly on the employed imprinting time. In figure B.1 we report an exampled of a 70 $\mu$s imprinting time in the unitary regime. This procedure would not end up creating a circulating state, just winding number zero. Still, the excitation is present. The more imprinting time we apply, the deeper is the depletion (and more pronounced instead the accumulation).

In order to study the behavior of the excitation, a more quantitative analysis is performed: first, as usual, the ring is unwrapped; then the density distribution is fitted with two Gaussian functions, one with a positive amplitude for the accumulation of density and one with negative value for the depletion. As a result, the amplitude, standard deviation, center and offset of the function are saved. To obtain an evolution of these quantities over time, we take multiple images with a variable timestep. For each time, 5 images are taken and averaged. We repeated the analysis with different timescales in order to access to phenomena both quickly vanishing or lasting for milliseconds.

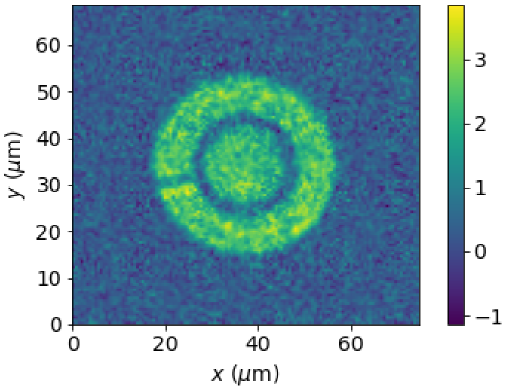


(a) Image taken 21 $\mu$s after imprinting.

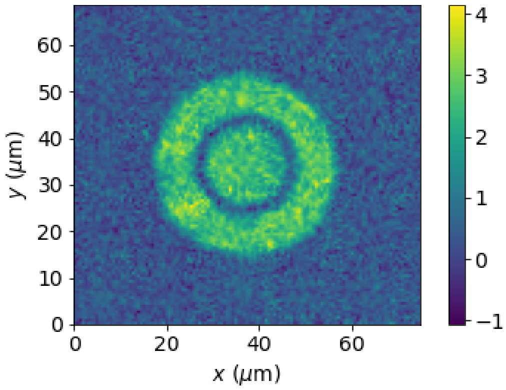


(b) Image taken 270 $\mu$s after imprinting.

Figure B.1: In situ image of the gas at different time after the phase imprinting: in correspondence with the phase jump of the imprinted gradient, a depletion and an accumulation in density profile of the ring are visible and quickly decays in time.

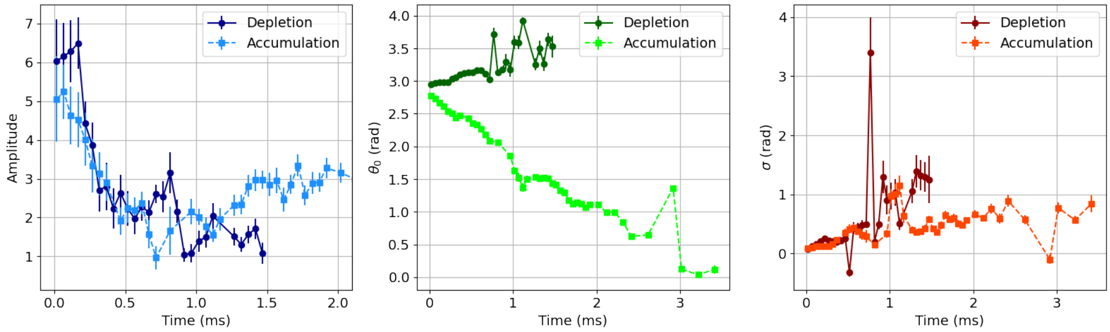


Figure B.2: Example of the results obtained from the analysis of the short-term excitation caused by phase imprinting. The density profile of an average image is fitted varying the acquisition time to monitor the evolution. On the left panel it is plotted the evolution in time of the amplitude from the fitted Gaussian of both depletion and accumulation. In center, the evolution of the position is shown: the accumulation moves faster and clockwise, instead the depletion moves slower in the anticlockwise direction. Finally, the broadening of the two excitation can be observed by looking at the standard deviation of the Gaussian fit, plotted in the right panel.

An example of the results obtained with the described analysis is reported in fig. B.2: from the result of the Gaussian amplitude it is possible to extract the decay rate of the excitation. Moreover, by looking at the center of the fitted function we can reconstruct the trajectory of the depletion and accumulation: after the imprinting the are propagating in opposite directions. Since the profile is linear in good approximation, it is straightforward to derive the propagation speed. Finally from the standard deviation it is possible to see that both the excitations broaden in time.

In the following we report some numeric results obtained. As said, values strongly depend on the regime of superfluidity explored. An interesting feature regards the propagation speed of the accumulation of density. Indeed, as expected, for all the regimes we found a very good agreement with the speed of sound. For UFG we obtained that the maximum decay rate observed is around 0.4 ms, while the speed of the density bump is 11.2±0.5 mm/s (compared to sound speed of $v_s = 11$ mm/s). An interesting feature observed only in unitary regime is a radial oscillation decaying in at most 1 ms, with a frequency that is around 30 times the first box energy level. In the BEC regime instead we find that the decay rate is at most 3 ms while the bump speed is 6.02±0.2 mm/s (where sound speed is $v_s = 5.8$ mm/s). Finally, in the BCS regime the maximum decay rate is 0.3 ms and the accumulation in the density propagates with a speed of 12.58±0.27 mm/s in excellent agreement with $v_s = 12.53$ mm/s.

As a conclusion, by phase imprinting technique we cause also a short-term excitation in the density. Anyway it decays very fast and most of all it does not interfere (as seen in the text) with the presence of currents in the ring.

# Bibliography


[1] M. W. Zwierlein, "Superfluidity in ultracold atomic Fermi gases," *Novel Superfluids*, pp. 269–422, 2015.

[2] R. P. Feynman, "Simulating physics with computers," *International Journal of Theoretical Physics*, vol. 21, no. 6-7, pp. 467–488, 1982.

[3] B. S. Deaver and W. M. Fairbank, "Experimental evidence for quantized flux in superconducting cyclinders," *Physical Review Letters*, vol. 7, no. 2, pp. 43–46, 1961.

[4] J. File and R. G. Mills, "Observation of Persistent Current in a Superconducting Solenoid," *Physical Review Letters*, vol. 10, no. 3, pp. 93–97, 1963.

[5] Y. Aharonov and D. Bohm, "Significance of electromagnetic potentials in the quantum theory," *Physical Review*, vol. 115, no. 3, p. 485, 1959.

[6] D. Loss and P. M. Goldbartt, "Persistent currents from Berry's phase in mesoscopic systems," *Physical Review B*, vol. 45, no. 23, pp. 15–1992, 1992.

[7] W. L. Goodman, W. D. Willis, D. A. Vincent, and B. S. Deaver, "Quantized Flux States of Superconducting Cylinders," *Physical Review B*, vol. 4, no. 5, pp. 1530–1538, 1971.

[8] M. Büttiker, Y. Imry, and R. Landauer, "Josephson behavior in small normal one-dimensional rings," *Physics letters a*, vol. 96, no. 7, pp. 365–367, 1983.

[9] R. Landauer and M. Büttiker, "Resistance of small metallic loops," *Physical review letters*, vol. 54, no. 18, p. 2049, 1985.

[10] J. Clarke and A. I. Braginski, *The SQUID handbook: Applications of SQUIDs and SQUID systems*. John Wiley & Sons, 2006.

[11] T. Fukuhara, A. Kantian, M. Endres, M. Cheneau, P. Schauß, S. Hild, D. Bellem, U. Schollwöck, T. Giamarchi, C. Gross, I. Bloch, and S. Kuhr, "Quantum dynamics of a mobile spin impurity," *Nature Physics*, vol. 9, no. 4, pp. 235–241, 2013.

[12] D. Bellem, *Generation of Spatially and Temporally Varying Light Potentials in Optical Lattices*. PhD thesis, München, 2011.

[13] A. Kumar, N. Anderson, W. D. Phillips, S. Eckel, G. K. Campbell, and S. Stringari, "Minimally destructive, Doppler measurement of a quantized flow in a ring-shaped Bose-Einstein condensate," *New Journal of Physics*, vol. 18, no. 2, pp. 0–7, 2016.

[14] S. Moulder, S. Beattie, R. P. Smith, N. Tammuz, and Z. Hadzibabic, "Quantized supercurrent decay in an annular Bose-Einstein condensate," *Physical Review A - Atomic, Molecular, and Optical Physics*, vol. 86, no. 1, pp. 1–7, 2012.

[15] B. I. Halperin, G. Refael, and E. Demler, "Resistance in superconductors," *Bcs: 50 Years*, pp. 185–226, 2011.

[16] A. Ramanathan, K. C. Wright, S. R. Muniz, M. Zelan, W. T. Hill, C. J. Lobb, K. Helmerson, W. D. Phillips, and G. K. Campbell, "Superflow in a toroidal bose-einstein condensate: An atom circuit with a tunable weak link," *Physical Review Letters*, vol. 106, no. 13, pp. 1–4, 2011.

[17] C. Ryu, M. F. Andersen, P. Cladé, V. Natarajan, K. Helmerson, and W. D. Phillips, "Observation of persistent flow of a Bose-Einstein condensate in a toroidal trap," *Physical Review Letters*, vol. 99, no. 26, pp. 10–13, 2007.

[18] S. Beattie, S. Moulder, R. J. Fletcher, and Z. Hadzibabic, "Persistent currents in spinor condensates," *Physical Review Letters*, vol. 110, no. 2, pp. 1–5, 2013.

[19] M. F. Andersen, C. Ryu, P. Cladé, V. Natarajan, A. Vaziri, K. Helmerson, and W. D. Phillips, "Quantized rotation of atoms from photons with orbital angular momentum," *Physical Review Letters*, vol. 97, no. 17, pp. 1–4, 2006.

[20] K. C. Wright, R. B. Blakestad, C. J. Lobb, W. D. Phillips, and G. K. Campbell, "Driving phase slips in a superfluid atom circuit with a rotating weak link," *Physical Review Letters*, vol. 110, no. 2, pp. 1–5, 2013.

[21] A. Kumar, S. Eckel, F. Jendrzejewski, and G. K. Campbell, "Temperature-induced decay of persistent currents in a superfluid ultracold gas," *Physical Review A*, vol. 95, no. 2, pp. 1–5, 2017.

[22] C. Ryu, E. C. Samson, and M. G. Boshier, "Quantum interference of currents in an atomtronic SQUID," *Nature Communications*, vol. 11, no. 1, pp. 2–7, 2020.

[23] R. Mathew, A. Kumar, S. Eckel, F. Jendrzejewski, G. K. Campbell, M. Edwards, and E. Tiesinga, "Self-heterodyne detection of the in situ phase of an atomic superconducting quantum interference device," *Physical Review A - Atomic, Molecular, and Optical Physics*, vol. 92, no. 3, 2015.

[24] Y. Cai, D. G. Allman, P. Sabharwal, and K. C. Wright, "Persistent currents in rings of ultracold fermionic atoms," *ArXiv ID 2104.02218*, vol. 1, no. 2, pp. 1–5, 2021.

[25] P. W. Anderson and N. Itoh, "Pulsar glitches and restlessness as a hard superfluidity phenomenon," *Nature*, vol. 256, no. 5512, pp. 25–27, 1975.

[26] G. Pecci, P. Naldesi, L. Amico, and A. Minguzzi, "Probing the BCS-BEC crossover with persistent currents," *ArXiv ID: 2010.03552*, pp. 1–7, 2020.

[27] Bardeen, John and Cooper, , L. N. Schrieffer, and J. Robert, "Theory of super conductivity," *Physical Review*, vol. 108, no. 5, p. 1175, 1957.

[28] T. Tsuneto, *Superconductivity and superfluidity*.

[29] M. Inguscio and L. Fallani, *Atomic physics: precise measurements and ultracold matter*. 2013.

[30] L. V. Keldysh and A. N. Kozlov, "Collective properties of excitons in semiconductors," *Sov. Phys. JETP*, vol. 27, no. 3, p. 521, 1968.

[31] D. M. Eagles, "Possible pairing without superconductivity at low carrier concentrations in bulk and thin-film superconducting semiconductors," *Physical Review*, vol. 186, no. 2, p. 456, 1969.

[32] V. N. Popov, "Theory of a Bose gas produced by bound states of Fermi particles," *Soviet Physics JETP*, vol. 50, p. 1034, 1966.

[33] W. Ketterle and M. W. Zwierlein, "Making, probing and understanding ultracold Fermi gases," *Rivista del Nuovo Cimento*, vol. 31, no. 5-6, pp. 247–422, 2008.

[34] A. Leggett, *Diatomic molecules and cooper pairs*, vol. 115, p. 13. 1980.

[35] M. Randeria and E. Taylor, "BCS-BEC Crossover and the Unitary Fermi Gas," pp. 1–33, 2013.

[36] P. Nozieres and S. Schmitt-Rink, "Bose condensation in an attractive fermion gas: From weak to strong coupling superconductivity," *J. Low Temp. Phys.; (United States)*.

[37] M. J. Ku, A. T. Sommer, L. W. Cheuk, and M. W. Zwierlein, "Revealing the superfluid lambda transition in the universal thermodynamics of a unitary fermi gas," *Science*, vol. 335, no. 6068, pp. 563–567, 2012.

[38] G. Del Pace, *Tunneling transport in strongly-interacting atomic Fermi gases*. PhD thesis, 2020.

[39] J. M. Kosterlitz and D. J. Thouless, "Ordering, metastability and phase transitions in two-dimensional systems," vol. 6, pp. 1181–1203, apr 1973.

[40] Z. Hadzibabic, P. Krüger, M. Cheneau, B. Battelier, and J. Dalibard, "Berezinskii-Kosterlitz-Thouless Crossover in a Trapped Atomic Gas," *Nature*, vol. 441, pp. 1118–1121, 2006.

[41] M. W. Zwierlein, A. Schirotzek, C. H. Schunck, and W. Ketterle, “Vortices and superfluidity in a strongly interacting Fermi gas,” *Nature*, vol. 435, no. June, pp. 1047–1051, 2005.

[42] L. A. Sidorenkov, M. K. Tey, R. Grimm, Y. H. Hou, L. Pitaevskii, and S. Stringari, “Second sound and the superfluid fraction in a Fermi gas with resonant interactions,” *Nature*, vol. 498, no. 7452, pp. 78–81, 2013.

[43] W. J. Kwon, G. D. Pace, R. Panza, M. Inguscio, W. Zwerger, M. Zaccanti, F. Scazza, and G. Roati, “Strongly correlated superfluid order parameters from dc Josephson supercurrents,” *Science*, vol. 369, no. 6499, pp. 84–88, 2020.

[44] L. Landau, “Theory of the superfluidity of helium II,” *Physical Review*, vol. 60, no. 4, pp. 356–358, 1941.

[45] P. J. Bendt, “Superfluid helium critical velocities in a rotating annulus,” *Physical Review*, vol. 127, no. 5, pp. 1441–1445, 1962.

[46] I. Rudnick, H. Kojima, W. Veith, and R. S. Kagiwada, “Observation of Superfluid-Helium Persistent Current by Doppler-Shifted Splitting of Fourth-Sound Resonance,” *Physical review letters*, vol. 23, no. 21, pp. 1220–1223, 1969.

[47] J. B. Mehl and W. Zimmermann, “Flow of superfluid helium in a porous medium,” *Physical Review*, vol. 167, no. 1, pp. 214–229, 1968.

[48] D. Loss and P. Goldbart, “Period and amplitude halving in mesoscopic rings with spin,” *Physical Review B*, vol. 43, no. 16, p. 13762, 1991.

[49] F. London, “Superfluids,” *(Willey, New York, 1950)*, vol. 8, 1950.

[50] R. Doll and M. Näbauer, “Experimental proof of magnetic flux quantization in a superconducting ring,” *Physical Review Letters*, vol. 7, no. 2, pp. 51–52, 1961.

[51] J. Puig, N. R. C. Bolecek, J. A. Sánchez, M. I. Dolz, M. Konczykowski, and Y. Fasano, “Bridge in micron-sized Bi2Sr2CaCu2O8+y sample act as converging lens for vortices,” pp. 1–7, 2021.

[52] L. Amico, A. Osterloh, and F. Cataliotti, “Quantum many particle systems in ring-shaped optical lattices,” *Physical Review Letters*, vol. 95, no. 6, pp. 1–4, 2005.

[53] F. Piazza, L. A. Collins, and A. Smerzi, “Vortex-induced phase-slip dissipation in a toroidal Bose-Einstein condensate flowing through a barrier,” *Physical Review A - Atomic, Molecular, and Optical Physics*, vol. 80, no. 2, pp. 1–4, 2009.

[54] L. Onsager, “Statistical hydrodynamics,” *Il Nuovo Cimento (1943-1954)*, vol. 6, no. 2, pp. 279–287, 1949.

[55] R. P. Feynman, “Atomic theory of liquid helium near absolute zero,” *Physical Review*, vol. 91, no. 6, p. 1301, 1953.

[56] R. P. Feynman, "Atomic theory of the two-fluid model of liquid helium," *Physical Review*, vol. 94, no. 2, p. 262, 1954.

[57] G. Valtolina, *Superfluid and spin dynamics of strongly interacting atomic Fermi gases*. PhD thesis, 2016.

[58] A. Burchianti, J. A. Seman, G. Valtolina, A. Morales, M. Inguscio, M. Zaccanti, and G. Roati, "All-optical production of 6Li quantum gases," *Journal of Physics: Conference Series*, vol. 594, no. 1, 2015.

[59] A. Burchianti, G. Valtolina, J. A. Seman, E. Pace, M. De Pas, M. Inguscio, M. Zaccanti, and G. Roati, "Efficient all-optical production of large Li 6 quantum gases using D1 gray-molasses cooling," *Physical Review A - Atomic, Molecular, and Optical Physics*, vol. 90, no. 4, pp. 1–5, 2014.

[60] C. J. Foot and Others, *Atomic physics*, vol. 7. Oxford University Press, 2005.

[61] H. J. Metcalf and P. van der Straten, "Laser cooling and trapping of atoms," *JOSA B*, vol. 20, no. 5, pp. 887–908, 2003.

[62] E. L. Raab, M. Prentiss, A. Cable, S. Chu, and D. E. Pritchard, "Trapping of Neutral Sodium Atoms with Radiation Pressure," *Physical Review Letters*, vol. 59, no. 23, pp. 2631–2634, 1987.

[63] A. L. Gaunt, T. F. Schmidutz, I. Gotlibovych, R. P. Smith, and Z. Hadzibabic, "Bose-einstein condensation of atoms in a uniform potential," *Physical Review Letters*, vol. 110, no. 20, pp. 1–5, 2013.

[64] N. Navon, A. L. Gaun, R. P. Smith, and Z. Hadzibabic, "Critical dynamics of spontaneous symmetry breaking in a homogeneous Bose gas," *Science*, vol. 347, no. 6218, pp. 167–170, 2015.

[65] L. Chomaz, L. Corman, T. Bienaimé, R. Desbuquois, C. Weitenberg, S. Nascimbène, J. Beugnon, and J. Dalibard, "Emergence of coherence via transverse condensation in a uniform quasi-two-dimensional Bose gas," *Nature Communications*, vol. 6, 2015.

[66] B. Mukherjee, Z. Yan, P. B. Patel, Z. Hadzibabic, T. Yefsah, J. Struck, and M. W. Zwierlein, "Homogeneous Atomic Fermi Gases," *Physical Review Letters*, vol. 118, no. 12, 2017.

[67] E. Nugent, D. McPeake, and J. F. McCann, "Superfluid toroidal currents in atomic condensates," *Physical Review A - Atomic, Molecular, and Optical Physics*, vol. 68, no. 6, p. 8, 2003.

[68] A. Das, J. Sabbatini, and W. H. Zurek, "Winding up superfluid in a torus via Bose Einstein condensation," *Scientific Reports*, vol. 2, no. 1, pp. 17–19, 2012.

[69] P. D. Drummond, A. Eleftheriou, K. Huang, and K. V. Kheruntsyan, "Theory of a mode-locked atom laser with toroidal geometry," *Phys. Rev. A*, vol. 63, p. 53602, apr 2001.

[70] L. J. Garay, J. R. Anglin, J. I. Cirac, and P. Zoller, "Sonic black holes in dilute Bose-Einstein condensates," *Phys. Rev. A*, vol. 63, no. 2, p. 23611, 2001.

[71] A. Görlitz, J. M. Vogels, A. E. Leanhardt, C. Raman, T. L. Gustavson, J. R. Abo-Shaeer, A. P. Chikkatur, S. Gupta, S. Inouye, T. Rosenband, and W. Ketterle, "Realization of Bose-Einstein Condensates in Lower Dimensions," *Phys. Rev. Lett.*, vol. 87, no. 13, p. 130402, 2001.

[72] L. Salasnich, A. Parola, and L. Reatto, "Bosons in a toroidal trap: Ground state and vortices," *Phys. Rev. A*, vol. 59, pp. 2990–2995, apr 1999.

[73] S. Gupta, K. W. Murch, K. L. Moore, T. P. Purdy, and D. M. Stamper-Kurn, "Bose-Einstein Condensation in a Circular Waveguide," *Phys. Rev. Lett.*, vol. 95, no. 14, p. 143201, 2005.

[74] Dobrek, M. Gajda, M. Lewenstein, K. Sengstock, G. Birkl, and W. Ertmer, "Optical generation of vortices in trapped Bose-Einstein condensates," *Physical Review A - Atomic, Molecular, and Optical Physics*, vol. 64, no. 5, p. 10, 1999.

[75] S. Burger, K. Bongs, S. Dettmer, W. Ertmer, K. Sengstock, A. Sanpera, G. V. Shlyapnikov, and M. Lewenstein, "Dark solitons in bose-einstein condensates," *Physical Review Letters*, vol. 83, no. 25, pp. 5198–5201, 1999.

[76] J. Denschlag, "Generating solitons by phase engineering of a Bose-Einstein condensate," *Science*, vol. 287, no. 5450, pp. 97–101, 2000.

[77] A. Kumar, R. Dubessy, T. Badr, C. De Rossi, M. De Goër De Herve, L. Longchambon, and H. Perrin, "Producing superfluid circulation states using phase imprinting," *Physical Review A*, vol. 97, no. 4, pp. 1–7, 2018.

[78] M. R. Andrews, C. G. Townsend, H. J. Miesner, D. S. Durfee, D. M. Kurn, and W. Ketterle, "Observation of interference between two bose condensates," *Science*, vol. 275, no. 5300, pp. 637–641, 1997.

[79] L. Pitaevskii and S. Stringari, "Interference of bose-einstein condensates in momentum space," *Physical Review Letters*, vol. 83, no. 21, pp. 4237–4240, 1999.

[80] W. Hoston and L. You, "Interference of two condensates," *Phys. Rev. A*, vol. 53, no. 6, pp. 4254–4256, 1996.

[81] M. Naraschewski, H. Wallis, A. Schenzle, J. I. Cirac, and P. Zoller, "Interference of Bose condensates," *Phys. Rev. A*, vol. 54, no. 3, pp. 2185–2196, 1996.

[82] H. Wallis, A. Röhrl, M. Naraschewski, and A. Schenzle, "Phase-space dynamics of Bose condensates: Interference versus interaction," *Phys. Rev. A*, vol. 55, pp. 2109–2119, mar 1997.

[83] M. E. Zawadzki, P. F. Griffin, E. Riis, and A. S. Arnold, "Spatial interference from well-separated split condensates," *Phys. Rev. A*, vol. 81, p. 43608, apr 2010.

[84] A. Röhrl, M. Naraschewski, A. Schenzle, and H. Wallis, "Transition from Phase Locking to the Interference of Independent Bose Condensates: Theory versus Experiment," *Phys. Rev. Lett.*, vol. 78, no. 22, pp. 4143–4146, 1997.

[85] W.-M. Liu, B. Wu, and Q. Niu, "Nonlinear Effects in Interference of Bose-Einstein Condensates," *Phys. Rev. Lett.*, vol. 84, pp. 2294–2297, mar 2000.

[86] L. S. Cederbaum, A. I. Streltsov, Y. B. Band, and O. E. Alon, "Interferences in the Density of Two Bose-Einstein Condensates Consisting of Identical or Different Atoms," *Phys. Rev. Lett.*, vol. 98, p. 110405, mar 2007.

[87] D. Sanvitto, F. M. Marchetti, M. H. Szymańska, G. Tosi, M. Baudisch, F. P. Laussy, D. N. Krizhanovskii, M. S. Skolnick, L. Marrucci, A. Lemaître, J. Bloch, C. Tejedor, and L. Vĩa, "Persistent currents and quantized vortices in a polariton superfluid," *Nature Physics*, vol. 6, no. 7, pp. 527–533, 2010.

[88] W. Wen and H. J. Li, "Interference between two superfluid Fermi gases," *Journal of Physics B: Atomic, Molecular and Optical Physics*, vol. 46, no. 3, 2013.

[89] C. Kohstall, S. Riedl, E. R. Sánchez Guajardo, L. A. Sidorenkov, J. Hecker Denschlag, and R. Grimm, "Observation of interference between two molecular Bose–Einstein condensates," *New Journal of Physics*, vol. 13, no. 6, p. 065027, 2011.

[90] W. Zhang and C. A. Sá De Melo, "Matter-wave interference in s -wave and p -wave Fermi condensates," *Physical Review A - Atomic, Molecular, and Optical Physics*, vol. 76, no. 1, pp. 1–8, 2007.

[91] M. Greiner, C. A. Regal, and D. S. Jin, "Emergence of a molecular Bose-Einstein condensate from a Fermi gas," *Nature*, vol. 426, no. 6966, pp. 537–540, 2003.

[92] R. P. Feynman, "Chapter II Application of quantum mechanics to liquid helium," in *Progress in low temperature physics*, vol. 1, pp. 17–53, Elsevier, 1955.

[93] J. S. Stießberger and W. Zwerger, "Critical velocity of superfluid flow past large obstacles in Bose-Einstein condensates," *Physical Review A - Atomic, Molecular, and Optical Physics*, vol. 62, no. 6, pp. 61601–61601, 2000.

[94] C. Raman, M. Köhl, R. Onofrio, D. S. Durfee, C. E. Kuklewicz, Z. Hadzibabic, and W. Ketterle, "Evidence for a critical velocity in a bose-einstein condensed gas," *Physical Review Letters*, vol. 83, no. 13, pp. 2502–2505, 1999.

[95] R. Onofrio, C. Raman, J. M. Vogels, J. R. Abo-Shaeer, A. P. Chikkatur, and W. Ketterle, "Observation of superfluid flow in a Bose-Einstein condensed gas," *Physical Review Letters*, vol. 85, no. 11, pp. 2228–2231, 2000.

[96] R. Desbuquois, L. Chomaz, T. Yefsah, J. Léonard, J. Beugnon, C. Weitenberg, and J. Dalibard, "Superfluid behaviour of a two-dimensional Bose gas," *Nature Physics*, vol. 8, no. 9, pp. 645–648, 2012.

[97] W. Weimer, K. Morgener, V. P. Singh, J. Siegl, K. Hueck, N. Luick, L. Mathey, and H. Moritz, "Critical velocity in the BEC-BCS crossover," *Physical Review Letters*, vol. 114, no. 9, pp. 1–5, 2015.

[98] L. Sanchez-Palencia, D. Clément, P. Lugan, P. Bouyer, and A. Aspect, "Disorder-induced trapping versus Anderson localization in Bose-Einstein condensates expanding in disordered potentials," *New Journal of Physics*, vol. 10, 2008.

[99] P. W. Anderson, "Absence of Diffusion in Certain Random Lattices," *Phys. Rev.*, vol. 109, pp. 1492–1505, mar 1958.

[100] M. Ögren and G. M. Kavoulakis, "Persistent currents in a Bose-Einstein condensate in the presence of disorder," *Journal of Low Temperature Physics*, vol. 149, no. 3-4, pp. 176–184, 2007.

[101] L. Kelvin, "On the motion of free solids through a liquid," *Phil. Mag*, vol. 42, no. 281, pp. 362–377, 1871.

[102] H. von Helmholtz, *über discontinuirliche Flüssigkeits-Bewegungen*. Akademie der Wissenschaften zu Berlin, 1868.

[103] R. Blaauwgeers, V. B. Eltsov, G. Eska, A. P. Finne, R. P. Haley, M. Krusius, J. J. Ruohio, L. Skrbek, and G. E. Volovik, "Shear Flow and Kelvin-Helmholtz Instability in Superfluids," *Physical Review Letters*, vol. 89, no. 15, pp. 2–5, 2002.

[104] S. N. Burmistrov, L. B. Dubovskii, and T. Satoh, "Kelvin-Helmholtz instability and dissipation in a phase-separated 3He-4He liquid mixture," *Journal of Low Temperature Physics*, vol. 138, no. 3-4, pp. 513–518, 2005.

[105] S. E. Korshunov, "Analog of Kelvin-Helmholtz instability on a free surface of a superfluid liquid," *JETP Letters*, vol. 75, no. 8, pp. 423–425, 2002.

[106] E. A. Henn, J. A. Seman, E. R. Ramos, M. Caracanhas, P. Castilho, E. P. Olímpio, G. Roati, D. V. Magalhães, K. M. Magalhães, and V. S. Bagnato, "Observation of vortex formation in an oscillating trapped Bose-Einstein condensate," *Physical Review A - Atomic, Molecular, and Optical Physics*, vol. 79, no. 4, pp. 1–5, 2009.

[107] N. Suzuki, H. Takeuchi, K. Kasamatsu, M. Tsubota, and H. Saito, "Crossover between Kelvin-Helmholtz and counter-superflow instabilities in two-component Bose-Einstein condensates," *Physical Review A - Atomic, Molecular, and Optical Physics*, vol. 82, no. 6, pp. 1–9, 2010.

[108] H. Takeuchi, N. Suzuki, K. Kasamatsu, H. Saito, and M. Tsubota, "Quantum Kelvin-Helmholtz instability in phase-separated two-component Bose-Einstein condensates," *Physical Review B - Condensed Matter and Materials Physics*, vol. 81, no. 9, pp. 1–5, 2010.

[109] D. Kobyakov, A. Bezett, E. Lundh, M. Marklund, and V. Bychkov, "Turbulence in binary Bose-Einstein condensates generated by highly nonlinear Rayleigh-Taylor and Kelvin-Helmholtz instabilities," *Physical Review A - Atomic, Molecular, and Optical Physics*, vol. 89, no. 1, pp. 1–7, 2014.

[110] A. W. Baggaley and N. G. Parker, "Kelvin-Helmholtz instability in a single-component atomic superfluid," *Physical Review A*, vol. 97, no. 5, pp. 1–7, 2018.

[111] W. J. Kwon, G. D. Pace, K. Xhani, L. Galantucci, A. M. Falconi, M. Inguscio, F. Scazza, and G. Roati, "Sound emission and annihilations in a programmable quantum vortex collider," 2021.

[112] J. P. Martikainen, K. A. Suominen, L. Santos, T. Schulte, and A. Sanpera, "Generation and evolution of vortex-antivortex pairs in Bose-Einstein condensates," *Physical Review A. Atomic, Molecular, and Optical Physics*, vol. 64, no. 6, pp. 1–5, 2001.

[113] A. C. White, C. F. Barenghi, and N. P. Proukakis, "Creation and characterization of vortex clusters in atomic Bose-Einstein condensates," *Physical Review A - Atomic, Molecular, and Optical Physics*, vol. 86, no. 1, pp. 1–8, 2012.

[114] M. Gehm, "Preparation of an optically-trapped degenerate Fermi gas of 6Li: Finding the route to degeneracy," 2003.

[115] C. Chin, R. Grimm, P. Julienne, and E. Tiesinga, "Feshbach resonances in ultracold gases," *Reviews of Modern Physics*, vol. 82, no. 2, pp. 1225–1286, 2010.

# Ringraziamenti

Insomma siamo arrivati alla fine. E la bellezza del percorso fatto non può portare malinconia ma solo gratitudine ed entusiasmo per ciò che verrà. Gratitudine che voglio esprimere in primis a coloro che mi hanno accompagnato quotidianamente in questo percorso di tesi: grazie Giacomo, perché sei stato una guida e un amico, hai sempre avuto a cuore il mio bene e non hai mai smesso di consigliarmi e suggerirmi. Mi hai fatto sentire accolto e stimato, e mi hai supportato e guidato in qualunque problema. Grazie Giulia. Hai avuto la pazienza e la gentilezza di insegnarmi tutto, dalle cose più pratiche in laboratorio a come stare davanti agli errori e agli sbagli. Thank you Woojin for the usefull discussions during these months: I will always remember the first questions you asked me in the lab and our conversations on ours plans and projects. Grazie ad Ale, fedele compagno di tesi, che mi hai subito accolto e insegnato quello che sapevi, mettendomi sempre al primo posto anche quando magari dovevi scrivere o fare altro. Grazie anche a Francesco: ci siamo visti poco in questi mesi ma ogni volta mi ha stupito il tuo entusiasmo nel salutarmi e nel raccontarmi. Grazie anche a Nicola, perché mi hai accompagnato in questi ultimo periodo, le domande che mi hai fatto e la tua curiosità mi hanno spinto a capire di più anche io quello che facciamo. Infine un grande grazie a Davide: in questi anni sei stato sempre presente, da una chiacchiera in corridoio al molto tempo e pazienza dedicati in confronti sulla scelta della tesi. La passione e la dedizione che metti nel tuo lavoro sono fonte di ispirazione, e i tuoi corsi che ho seguito mi hanno appassionato e segnato, tanto che hanno determinato le mie scelte per la tesi e per approcciarmi al mondo del lavoro.

Un inevitabile ringraziamento va alla mia famiglia, innanzitutto a mamma e papà: evidentemente dire che senza di voi tutto questo non sarebbe stato possibile è riduttivo. Mi sembrano troppi i motivi per cui vorrei ringraziarvi, ma in questa tesi di laurea forse non ci stanno. Mi avete sempre accompagnato, anche se io - testardo - spesso ho deciso di testa mia; ma voi avete continuato a supportarmi e stimarmi, volermi bene, essere disponibili, e spendervi in tutto per me. Grazie Luca, perché anche se non lo sai ho sempre tenuto gli occhi puntati in alto verso di te guardandoti con stima, per come sai stare con i nostri genitori, con i tuoi amici, con i miei amici, e come affronti le circostanze di tutti i giorni. Grazie anche a Maria, perché insieme in questi anni siete stati un bellissimo esempio da guardare e imitare, e perché in questa decisione di formare una nuova famiglia avete dato prova di un coraggio e di una certezza che mi infondono forza. Un grazie va anche a tutto il resto della famiglia, unici che mi avete accompagnato fin da bambino. Grazie nonna Mia, perché vedo il tuo affetto crescere sempre di più in questi anni: sei stata una grande compagnia e mi hai ispirato ad essere sempre migliore in questi anni. Un ringraziamento anche agli zii Emi e Anna, e a Ceci e Paolo, per tutti i momenti che abbiamo condiviso e vissuto insieme. Grazie a nonna Gigia, per la tua accoglienza sempre calorosa, e un grazie anche a tutto il resto della famiglia che è sempre stato negli anni un punto di riferimento e unità: zia Rosi, Dalila e Riccardo, Alice e Flavio, così come Leo, Cory, Niki e Ale, Babi, Marco, Giack, Albi e Michi. Una menzione speciale al mio mitico padrino zio Francesco per la tua presenza costante in questi anni.

Sono poi tanti gli amici che mi hanno accompagnato negli anni e a cui devo un ringraziamento, sicuramente ne dimenticherò tanti e per questo chiedo scusa in anticipo. Parto da quelli che ho più recentemente conosciuto qui a Firenze: i compagni di pranzi Michele, Nicoletta, Alessia, Tusi e di aperitivi Frengo e Livi. Un grazie enorme anche agli amici che ho incontrato fuori dall'università e che in questi mesi mi hanno accolto nella loro città. Per cui un ringraziamento speciale va a tutti gli amici della scuola di comunità, in questi mesi luogo di crescita, confronto, e di nascita di nuove amicizie. In particolare grazie a Pietro e Lucia, vi auguro una bellissima vita insieme, a don Giordano, Alice, Civa, Franci, Tambu, Lore, Stade, Edo, Elda, Totò, Ester Volpetti, per le birre, le cene, le giornate insieme, e la compagnia che mi avete fatto in questi mesi, rendendo Firenze un po' più casa. Rimane una menzione speciale per Ricca, grande compagno d'appartamento: abbiamo condiviso insieme moltissime cene e mi hai fatto conoscere ed incontrare i tuoi amici, ti ringrazio molto. E poi un grazie ad Ester Pevere, una grande amicizia nata inaspettatamente, e a Marina, fin da subito mio angelo custode, vi ringrazio per il bene immeritato e gratuito che mi avete voluto fin da subito.

Pensando a questi anni di università non posso che ringraziare tutti gli amici più grandi, che mi hanno insegnato con il loro stare insieme un modo bello e desiderabile di vivere, tra cui Simo, Richi, Eddi, Sabba, Samu, Scotti, Peter, Ila, Gëck, Gio, Rache, Ciondi, Bubba, Bianca, Bella, Cicca. Ringrazio poi gli amici con cui più ho passato questi anni, perché grazie a voi vivere l'università è stato bello ed entusiasmante: Ste Marni, Cheva e Ali, Nico, Giorgio, Chiara, Scan, Simo Riva, Ermo, Sara, Cate Mina, Gloria, Frenk, Silvia, Franci, Teo, Gege, Jack Bolchi, Zu, Elia, Pingu, Duce, Becca, Benni, le due Cate, Marti, Guggo, Simo de Rueco, Harem, Gigi, Trava, Raul, Tdl, ognuno di voi ha contribuito con un sorriso, una battuta, un caffè, un pranzo o molto altro a rendere speciale per me Fisica. Ringrazio in particolare tutte le "matroccole", che rimarranno tali anche se ormai giunte al terzo anno, soprattutto Tommi Colo, Giuli, Nene, Ema, Gala, Sky, Paola, Michi, Martolina, Pelle, Sid, Franci Curto, Tommi Rove, Bonni e Cate Maino, perché stare con voi mi ha responsabilizzato ed educato a stare seriamente nella realtà. Un grazie poi va a Clara, fedele amica, Maddi, per i bei viaggi in metro con cui spesso iniziavano le giornate, Bailey, per l' attenzione che mi hai sempre rivolto, Pivets, perché in questi anni hai imparato a sopportare le mie freddure e volermi bene lo stesso, Leo, perché mi hai sempre richiamato all'essenziale pur nello sparare cazzate, Tia e Tine, perché abbiamo condiviso insieme una marea di cose e vi ho proprio riscoperto in università, Gio, perché sei stato per me una vera sorpresa in questi anni, Miri, perché sei stata un grande esempio e una grande amica e mi hai fatto crescere tanto, Jane, per volermi così bene e per tutte le bellissime vacanze a cui mi hai invitato (e spero continuerai a fare ahahah). Un ringraziamento ad hoc lo devo anche a Carlo, primo amico di università, compagno di mille avventure, con la speranza che un giorno le nostre strade si possano incontrare di nuovo. Grazie Abbo, perché se sono qui a scrivere queste righe sicuramente buona parte del merito la devo a te, che a partire dalla quarantena mi sei stato compagno in tanti esami, e mi hai fatto riscoprire la bellezza di studiare; meriteresti una statua! Grazie Michi, perché sei stata proprio un bellissimo dono in questi anni: sia nello studio che nella compagnia di tutti i giorni, mi hai sempre preferito con semplicità e fedeltà. Grazie Mavi: innanzitutto mi hai fatto studiare quando ci hanno rinchiuso in casa, e già questo è un mezzo miracolo, ma soprattutto sei stata in tutti questi anni una amica sincera con cui ho potuto condividere tutto. Grazie Blanco, perché da Arenzano è sbocciata una amicizia vera che mi sta aiutando a vivere meglio le giornate.

Voglio poi ringraziare tutti gli amici del coro alpino e in particolare i tenori II, tra cui un immenso grazie va a Matt, e anche ai suoi ”successori” Gabri e Luca Pozzi, affezionatissimi al coro e sempre disponibili per me. Grazie anche al coro di scienze a partire dai direttori Edo, a cui va un ringraziamento speciale, e Cami, con cui è stato bello condividere gli ultimi anni, fino a tutti i coristi, in particolare Meri, Mango, Piva, Ema, Merlo, Meggy, Fede, Luci, Pis, Soldato, Genna, Cate Pini, Cate Ferrari, Nico. Un grazie agli altri amici delle colazioni dopo messa Sandro, Franci, Ezio, a donCe che in questi anni è stato punto di riferimento costante, e agli altri amici del gruppo di Portofranco Maddi, Ester e Anna, con cui è nato un bellissimo rapporto. Ringrazio poi tutti gli altri amici di ”Porcatroia” Jack, Busca e Liga per le serate e i giripizza fatti insieme. Ringrazio poi tutti gli adulti e le famiglie incontrate in questi anni e che mi hanno accompagnato a fare un pezzo più o meno lungo di strada, tra cui Malini, Bianchi, Colombini, famiglia Mauro, famiglia Martinelli, famiglia Pantiri, famiglia Giannattasio, famiglia Bollea, Cristina, Lollo, Nella, Ernesto, Chicco, Franci, Andre e Giudi. Un grazie davvero speciale a Sara e Ele, grandi amiche da anni, perché le cene che periodicamente facciamo sono un punto fisso durante l’anno, e grazie agli altri amici del liceo in particolare Chiara, Anna, ed Enri. Grazie anche a Olga e Leti, perché anche se ormai ci vediamo raramente non sbiadisce mai la freschezza della nostra amicizia. Ci tengo poi a ringraziare Ire, per l’amicizia di questi anni, che non è stata mai banale ma sempre interessata al destino. Sì lo so Samu, tu sei rimasto fuori da tutti i gruppi, ma solo perché meriti un ringraziamento speciale a parte. Ti ringrazio perché in questi anni, pur a distanza o venendo meno la frequentazione quotidiana, il confronto e il racconto con te è stato sempre presente. E grazie anche alla Betta: non vedo l’ora di poter vivere con voi la gioia del passo che avete deciso di intraprendere!

Alla fine un ringraziamento va a te, Agne, che - pur ignara - sei qui davanti a me a tenermi compagnia collegata a 300 km di distanza, lamentandoti che lo sciroppo non è più buono come quando eri bambina... Non so da dove iniziare, e tante cose non si possono scrivere in una tesi di laurea. Ma sicuramente un posto nei ringraziamenti

te lo eri meritata anni fa, quando con la tua dolcezza e gentilezza avevi raddrizzato qualche giornata ”no”. Poi che dire, in questo ultimo anno ti sei guadagnata la piazza d’onore qui in fondo, perché come dice la canzone *hai preso la mia vita e ne hai fatto molto di più*, aiutandomi a camminare sempre di più verso la verità di me. Ma qui inizia tutta un’altra storia, che spero potrà trovare posto in un altro capitolo del libro della vita che si apre ora.